Using Droplet Induced Deformations in Polymeric Functional Materials for Heat and Mass Transport Modulation

by

Akshay Phadnis

A Dissertation Presented in Partial Fulfillment
of the Requirements for the Degree
Doctor of Philosophy

Approved May 2019 by the
Graduate Supervisory Committee:

Konrad Rykaczewski, Chair
Timothy Burgin
Robert Wang
Liping Wang
Jay Oswald

ARIZONA STATE UNIVERSITY

August 2019

ABSTRACT

Droplet-structure interactions play a pivotal role in many engineering applications as droplet-based solutions are evolving. This work explores the physical understanding of these interactions through systematic research leading to improvements in thermal management via dropwise condensation (DWC), and breathable protective wearables against chemical aerosols for better thermoregulation.

In DWC, the heat transfer rate can be further increased by increasing the nucleation and by optimally 'refreshing' the surface via droplet shedding. Softening of surfaces favor the former while having an adverse effect on the latter. This optimization problem is addressed by investigating how mechanical properties of a substrate impact relevant droplet-surface interactions and DWC heat transfer rate. The results obtained by combining droplet induced surface deformation with finite element model show that softening of the substrates below a shear modulus of 500 kPa results in a significant reduction in the condensation heat transfer rate.

On the other hand, interactions between droplet and polymer leading to polymer swelling can be used to develop breathable wearables for use in chemically harsh environments. Chemical aerosols are hazardous and conventional protective measures include impermeable barriers which limit the thermoregulation. To solve this, a solution is proposed consisting of a superabsorbent polymer developed to selectively absorb these chemicals and closing the pores in the fabric. Starting from understanding and modeling the droplet induced swelling in elastomers, the extent and topological characteristic of swelling is shown to depend on the relative comparison of the polymer and aerosol geometries. Then, this modeling is extended to a customized polymer, through a simplified characterization paradigm. In that, a new method is proposed to measure the swelling parameters of the polymer-solvent pair and develop a validated model for swelling. Through this study, it is shown that for this polymer, the concentration-dependent diffusion coefficient can be measured through gravimetry and Poroelastic Relaxation Indentation, simplifying the characterization effort. Finally, this model is used to design composite fabric. Specifically, using model results, the SAP geometry, base fabric design, method of composition is optimized, and the effectiveness of the composite fabric highlighted in moderate-to-high concentrations over short durations.

Dedicated to…

Aai, Baba & Namrata

ACKNOWLEDGMENTS

I would like to sincerely thank my advisor Dr. Konrad Rykaczewski for providing the best mentorship and guidance a PhD student can experience. His teachings of creative thinking and problem-solving have prepared me for the journey ahead.

My journey before starting the PhD prepared me for the path that laid ahead. I want to sincerely thank my parents for that journey, their faith in me, and for preparing me to take risks. I cannot mention the incredible support provided by my lovely wife Namrata during PhD and otherwise. Without my parents and Namrata, this would not have been possible. I would also like to thank my brother Ashish, bhabhi Namrata and my nephew Darshan for being the source of my rejoice and an indirect motivation for my achievements.

I have been lucky to have garnered incredible friends in my life who have helped me become a better person at every step in my life. I would like to thank Dr. Viraj Damle for his constant support and unhindered friendship. I thank all my friends from GE and PVG for everything and all the incredible moments. I would also like to thank my collaborators and lab-mates Kenneth Manning and Praveen Kotagama for many fruitful discussions, insights in experiment design and uncountable debates. And last but not least, I would like to thank all my mentors, teachers and relatives for their support and direct and indirect impact on my life.

TABLE OF CONTENTS

Page

CHAPTER Page

LIST OF FIGURES

Figure Page

Figure Page

1 INTRODUCTION

Thermal management imposes a severe challenge in designing systems ranging from power plants, processor industries, climate control and even immunotherapy and thermoregulation. These challenges can be ‘direct’ as in case of thermal power plants, cooking appliances and engines, and ‘indirect’ as in case of microelectronics packaging, HVAC and thermoregulation of the human body, where thermal effects are mostly a bi-product and often undesirable. All the solutions to these challenges fall under either of the following two categories *viz.* efficient transport of thermal energy from the source or reduction in generation of thermal energy at the source. Over the years, a significant improvement has been observed in thermal management solutions owing to the evolution in the complementary fields like manufacturing technology, material science, modeling and simulation techniques and at the same time, academic research evolving understanding of the underlying complex phenomenon. The parallel developments in the field of material science and the fundamental academic research especially, have had a considerable impact. Development in the wide range of novel materials has changed several design aspects.

Of all the materials, polymers, both natural and synthetic, have provided a solution in a range of engineering applications, almost ubiquitously. In thermal management, they have been widely used as insulators, structural materials, sensors, controls, etc. However, since recently, polymers and polymer composites are finding applications in solutions where they are used for promoting thermal energy transport such as personalized cooling suits for space and outdoor applications (thermoregulation),[1,2] thermal interface materials in electronics and wearables,[3–6] and promoting dropwise condensation[7–9] to name a few. Many of these applications involve functional polymeric materials interfacing with the working fluid either in the form of droplets or in bulk. Given this premise, it is worthwhile to look at thermal, mechanical and even chemical interactions between polymers and fluids and especially droplets. Conducting fundamental research on droplet-polymer interactions would be of great interest especially when these interactions can be exploited to design novel thermal management solutions.

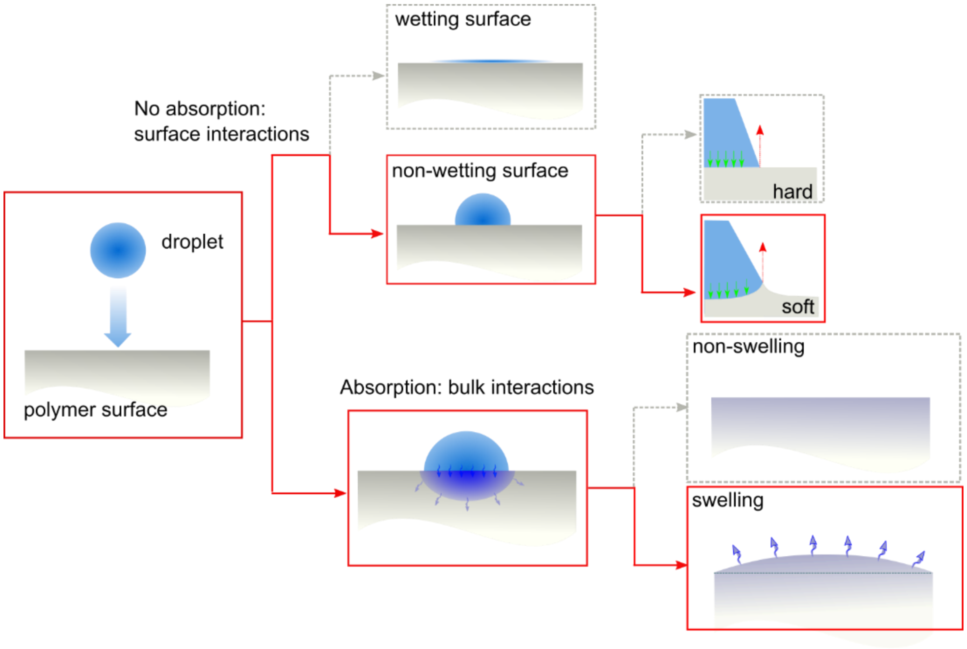

Figure 1.1 Regime map of different droplet-polymer interactions, the focus areas of this work are highlighted in red.

In view of the droplet-surface interactions, we need to consider the following phenomenon- spreading, evaporation and absorption, which governs these interactions. Depending upon how the timescales associated with these processes compare, *i.e.* t_s, t_e and t_a, we can see completely different behaviors. When a droplet of a given fluid comes in contact with a polymer surface, the droplet gets absorbed in the polymer matrix if the absorption time scale t_a is short or stays on the surface if it is too large as compared to the other two time scales. This broadly classifies the droplet-polymer interactions into two categories *viz.* bulk interactions and surface interactions between droplet and the polymer.

First let us consider the case of droplet staying on the polymeric surface. When the droplet hits such surface, it can either spread if the spreading time scale is short or “bead-up” depending upon the wettability of the surface (spreading time scale is irrelevant here and we assume t_a to be significantly high). Significant amount of work has been done on the former case and underlying mechanism have been explored for a range of engineering surfaces.[10–12] Beading of the droplet on the other hand is favored in dropwise condensation and has been a prime focus of the research only in recent years to develop specialized surfaces that achieve this. A sessile droplet shares two interactive forces with the surface- Laplace pressure in the droplet and surface tension force along the triple phase contact line (TPCL). With the ‘soft enough’ surface, these forces can cause comparable deformations that in turn affects the condensation heat transfer. If on the other hand, the polymer absorbs the droplet in case where $t_a \gg t_s \: and \: t_e$, depending upon the polymer-fluid pair, certain interesting bulk interactions are observed. Some crosslinked polymers, absorb the favorable fluid while dilating volumetrically, a phenomenon known as ‘swelling’. Through carefully tuned chemistry, specialized polymers can be developed that swells by absorbing target chemicals.

The objective of my thesis will be to explore the two specific interactions pertaining to the two cases discussed above. Thus, the thesis is broadly classified into two sections- I. Surface interactions between droplets and functional polymeric surfaces and II. Bulk interactions between droplets and superabsorbent/swellable polymers. I recognize that studying these two cases can be of interest in two thermal management applications *viz.* dropwise condensation (DWC) and thermoregulation. In DWC, I explore thermo-mechanical interactions between condensate droplet and soft, conductive polymeric surfaces which I discuss in chapter 2 of this thesis. Whereas, in thermoregulation, I explore chemo-mechanical swelling interactions between polymers and chemical droplets to design and develop breathable, adaptive wearable which is compiled in chapters 3, 4 and 5.

SECTION I. DROPLET INDUCED SURFACE DEFORMATIONS

Dropwise condensation (DWC) has been in focus for over a decade as it promises significant improvements over conventional filmwise mode. In DWC, water vapor condenses on the surface kept below its dew point temperature in the form of droplets which grow and coalesces to grow as more vapor condenses. As the droplets grow, the conduction resistance increases reducing the heat transfer rate, thus it is beneficial to remove the droplets beyond a critical size and “refresh” the surface for ‘new’ droplets to nucleate which offer high heat transfer rate. To achieve this, non-wetting surfaces are required which promote droplet formation followed by their easy removal. Typically, these surfaces are obtained by changing the surface chemistry to achieve low interface energy or through surface texture or sometimes, both. Ideal non-wetting surfaces not only provide means for drops to form but also reduce the contact angle hysteresis (CAH) which promotes the easy removal of bigger droplets.

Recent developments in achieving such surfaces include chemical modifications via low energy coatings, microstructures and application of polymer coatings, to name a few. Furthermore, it was recently shown recently that soft surfaces increase the nucleation rate. This increase is attributed to the mechanical interactions between condensate droplets and surfaces. Let’s assume a sessile droplet on the surface as shown in Figure I-1. At macroscopic scale, it interacts with the surface via two mechanisms. The droplet surface tension at the triple phase contact line (TPCL) pulling the surface upward and the Laplace pressure inside the droplet presses against the surface. For a given liquid (water in this case) the vertical component of surface tension force at TPCL is high for high apparent contact angles (e.g. $\theta \rightarrow 90°$, $sin\theta \rightarrow 1$). As for the Laplace pressure, since it increases with decrease in radius ($P_l = 2\sigma/r$), smaller droplets exert higher pressure.

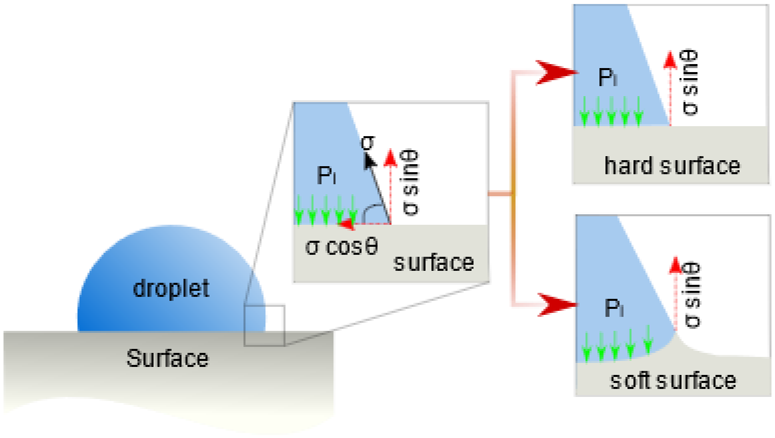

Figure I-1. Schematic showing mechanical interactions between droplet and surface during dropwise condensation.

Thus, the initial period of DWC where droplets with high contact angle are sufficiently small the surface experiences the maximum forces. Although these forces are small for hard materials like metals, they can result into considerable deformations in softer materials such as silicones. Thus, these interactions become important in the DWC regime targeted to maximize the heat transfer *i.e.* high contact angle small droplets achieved using low energy soft silicone-based surfaces. In the following text, we explore these interactions and their effect on the overall heat transfer during DWC. In chapter 2, using a combined numerical-experimental approach, I quantify the effect of deformations in soft surfaces on DWC heat transfer. To estimate the heat transfer, I developed a numerical model based on finite element approach in COMSOL. This model assumes the heat removal from a surface maintained at constant temperature via conduction across water inside the droplet.

Although we consider only conduction heat transfer through a sessile droplet, another mechanism persists that affects the thermal transport. When a sessile droplet is placed on the colder surface, the droplet bulk in the immediate vicinity of the surface achieves its temperature while the top region of the droplet has the saturation temperature with a temperature gradient existing along the height of the droplet as shown in Figure I-2 resulting in surface tension gradient. This non-equilibrium state gives rise to a flow-field in the opposite direction to balance the shear forces and is known as Marangoni flow. Since this flow ‘convects’ the cold fluid to the hot regions, it is sometimes referred to as Marangoni convection.

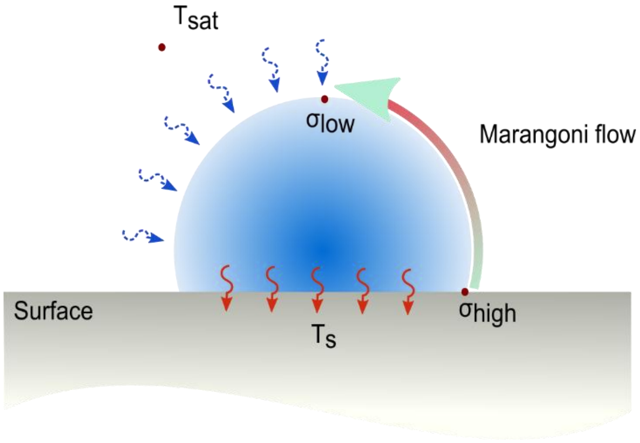

Figure I-2. Schematic of surface tension induced Marangoni flow in a sessile condensate droplet on a hydrophobic surface.

The presence of this flow is long known but its effect on heat transfer has not been quantified yet. Conventional analytical models and numerical models neglect any contribution of this flow to the DWC heat transfer. Although, this is true for small droplets, due to small surface tension gradients, the effect could be significant in larger droplets. Thus, while estimating the heat transfer during DWC on soft, hydrophobic surfaces, I investigated the effect of Marangoni flows on numerical predictions. In chapter 2, I discuss the details of this study. First, I present the theoretical foundation for Marangoni flows and its significance in different geometrical regimes of droplet using non-dimensional scaling laws. Then, I present a finite element model that incorporates the Marangoni flow physics with the heat transfer in a sessile droplet. Using this model, I quantify the effect of modeling Marangoni flows in heat transfer predictions across droplets of different size, contact angle and fluids. The primary target of this part is to address any gaps in capturing the physical phenomenon during DWC heat transfer to design better systems.

2 DROPWISE CONDENSATION ON SOFT, HYDROPHOBIC SURFACES

2.1 Introduction

Promoting dropwise condensation (DWC) could improve the efficiency of many industrial systems[13–17] because it is associated with a 5 to 10-fold heat transfer rate increase in heat transfer as compared to the currently predominant film-wise mode.[18]Because of the search for a durable material that could sustainably promote DWC,[7,9,15,19–25] a lot of attention has been recently dedicated to finding routes to even further enhance the heat transfer rate during this phase change process. A moderate level of enhancement has been demonstrated with use of chemically heterogeneous,[26–34] textured,[35–40] and lubricant-impregnated substrates.[9,22,23,41] In contrast, DWC heat transfer enhancement using soft substrates that have mechanical properties in-between the extensively studied "hard solid" and liquid substrates has received limited attention.

Encouragingly, Sokuler *et al.*[8] demonstrated that softening of a hydrophobic elastomer surface enhances the initial condensation rate by increasing droplet nucleation density. Such materials can also alter dynamics of droplet impact onto[42–49] and movement across surfaces.[50–61] Furthermore, Jeong *et al.*[6] and Barlett *et al.*[3] recently demonstrated that inclusion of room temperature liquid metal nano/microdroplets (e.g. EGaIn or EGaInSn) in silicone matrix significantly increases thermal conductivity of the resulting composite (k~1 to 10 $\mathrm{Wm^{-1}K^{-1}}$) without considerably altering its mechanical properties. Since silicones are hydrophobic, reasonable thickness coatings (~5 to 10 µm) made out of such soft composites could be used to promote DWC without introducing a significant parasitic thermal resistance. Motivated by these results, here I investigate how mechanical properties of a substrate impact relevant droplet-surface interactions and the overall DWC heat transfer rate.

The overall DWC heat transfer rate is dictated by heat transfer through individual drops ($q_d(r,\theta)$), critical embryo radius (r_{min}), nucleation density (N_s), and droplet shedding radius (r_{max}).[18,62,63] The nucleation density determines the threshold radius (r_e) that segregates nanoscale (($n(r)$) and micro-to-macroscale ($N(r)$) droplet populations, while the droplet shedding radius determines how often the surface is refreshed for subsequent droplet growth cycle. In more quantitative terms, the total heat transfer per unit area of a condenser surface is given by:

$$q" = \int_{r_{min}}^{r_e} q_d(r,\theta)\, n(r)\, dr + \int_{r_e}^{r_{max}/1.3} q_d(r,\theta)\, N(r)\, dr \qquad (2.1)$$

In this model formulation the value of the critical radius does not depend on surface properties ($r_{min} = 2T_{sat}\gamma/H_{fg}\rho\Delta T$ where T_{sat} is the saturation temperature, ΔT is subcooling of the substrate, γ is liquid-vapor surface tension, H_{fg} is the latent heat, and ρ is the condensate liquid density). Similarly, softening of the substrate is not likely to affect the functional form of the droplet size distribution. Specifically, $n(r)$ and $N(r)$ should be well-represented through classical models,[18,62] which reasonably describe droplet populations on both solid and liquid surfaces.[41] However, change in mechanical properties of the substrate will affect two of the three boundary values of these size distributions, namely r_e and r_{max}. The value of r_e will be altered because it is defined by the droplet nucleation density ($r_e = 1/\sqrt{4N_s}$). The value of r_{max}, in turn, will be altered because of the formation of a solid wetting ridge around the droplet perimeter. The schematic in Figure 2.1 shows that this deformation occurs because of the combined effect of the condensate liquid's surface tension and Laplace pressure inside the drop.[60,64–67] The depression of the substrate under the drop will also increase the thermal resistance posed by the liquid as well as the liquid-solid interfacial area, thus altering $q_d(r,\theta)$.

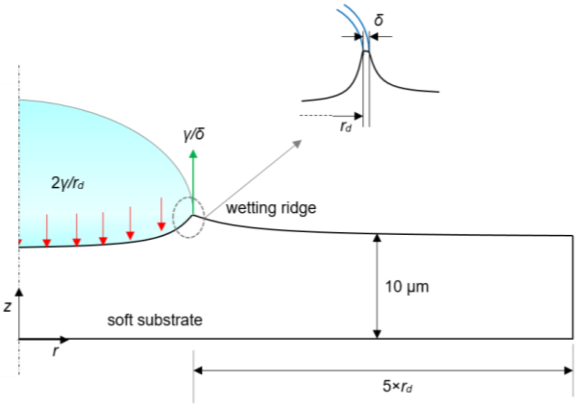

Figure 2.1 Axisymmetric schematic illustrating forces imposed by a droplet on a soft substrate and its resulting deformation.

Here, the focus is on quantifying how mechanical properties of the substrate change the values of r_e, r_{max}, and $q_d(r,\theta)$. Specifically, I measured r_e and r_{max} of condensate on silicone substrates with elastic modulus altered through varied cross-linking density. To quantify the impact of mechanical properties on $q_d(r,\theta)$, the analytical solution of elastomer deformation induced by droplets with finite element-based heat transfer model is combined. By substituting these experimentally and theoretically derived values into the DWC model (equation 2.1), I quantify the effect of the substrate's elastic modulus on the overall heat transfer rate.

2.2 Methods

2.2.1 Materials

To quantify the effect of the shear modulus of the substrate, *G*, on droplet nucleation density and departure size, I fabricated 350 µm thick PDMS (Sylgard® 184, Dow Corning) slabs with varied base to cross-linker ratios. Specifically, use of base to cross-linker ratios of 10:1, 20:1 and 33:1 by weight which correspond to *G*=75 kPa, 220 kPa, and 500 kPa, respectively.[59] We note that for a moving liquid front such as perimeter of a condensing droplet, the height of the substrate deformation is determined using the shear modulus, rather than Young's modulus, E, of the substrate (for isotropic and incompressible material like PDMS with Poisson's ratio $v = 0.5$, $G \approx E/(2(v+1) \approx E/3)$.[57] The samples were poured into a mold made out of 350 µm thick silicon wafers and cured at 60 °C for 1 hour. All of the resulting silicone substrates were highly hydrophobic with contact angles above 105° and contact angle hysteresis below ~15° (see Appendix A for more information). For a "hard" reference substrate with comparable wetting properties, I used a silicon wafer (*G*=50 GPa) coated with fluorosilane ((Tridecafluoro-1,1,2,2-Tetrahydrooctyl)Trichlorosilane, Gelest Inc.)

2.2.2 Condensation experiments

In order to measure r_e and r_{max}, I conducted condensation experiments with horizontal and vertical sample orientation. The experiments were conducted in a modified environmental chamber (Electro-tech Systems 5518) with air temperature of 22±0.2 °C and 99±1% relative humidity. The condensation process was initiated by decreasing the sample temperature by 5 °C below dew point using a water-cooled Peltier cooler connected to a programmable temperature controller (PTC10 Stanford Research System). The controller receives temperature feedback from the copper-constantan thermocouple (0.003” dia, Omega) attached to the PDMS surface. I imaged condensation on the horizontally oriented samples every 5 seconds using a high magnification optical microscope (Axio Zoom.V16) with an objective lens of 2.3x/0.57 FWD and 10.6 mm focal length (Zeiss PlanNeoFluar Z) that is integrated with the chamber using a custom extension.[68] Additionally, I imaged the condensation process on vertically oriented samples with a digital camera (DFK23UP031, ImagingSource) at 15 fps. All the resulting images were analyzed in ImageJ. Specifically, I measured the projected base contact area of droplets and, if the droplets were not circular, calculated the radius of the equivalent circle, r_b. We then calculated the equivalent radius r_d of the droplet using corresponding static contact angle, θ using $r_d = r_b/sin\theta$. I analyzed at least 15 droplets per sample to calculate the average radius. These values are reported with uncertainty determined using student’s t-test with 99.7% confidence interval. Four different measurements were done on each sample. These values are reported with uncertainty corresponding to 95%

confidence interval. More details on the experimental setup are available in the Appendix A.

2.2.3 Modeling of heat transfer across individual droplets on soft substrates

In order to simulate how the deformation of the substrate geometry impacts heat transfer, I combined Yu *et al.*'s[65] analytical substrate deformation model with finite element model of heat conduction. As explained earlier, the combined action of Laplace pressure and surface tension deforms the substrate. A two-dimensional quasi-steady model of substrate deformation has been developed using linear momentum balance:

$$\nabla\sigma = 0 \tag{2.2}$$

with the following boundary conditions:

$$\sigma_{zz} = \left\{ \begin{matrix} P = \frac{2\gamma}{r}, r \leq r_d \\ \tau = \frac{\gamma}{\delta},\ \ R \leq r \leq r_1 = r_d + \delta \\ 0, \qquad r > r_1 \end{matrix} \right\}$$

Where, σ is the stress, P is the Laplace pressure, γ is the liquid-vapor interface tension, δ is the molecular level liquid-vapor interface thickness and r_d is the drop radius (also referred to as *r* elsewhere in the article). Yu *et al.* used a linear elastic material model to calculate the strains. After implementing the boundary conditions, the following analytical solution are obtained in terms of the hypergeometric function, ${}_2F_1$, for the vertical displacement:

$$u_z(r,0) = \left\{ \begin{array}{c} \frac{2(1-v^2)}{E}\left[r_1\tau \cdot {}_2F_1\left(\frac{1}{2},-\frac{1}{2};1;\frac{r^2}{r_d^2}\right) - r_d(P+\tau) \cdot {}_2F_1\left(\frac{1}{2},-\frac{1}{2};1;\frac{r^2}{r_d^2}\right)\right],\ r \le r_d \\ \frac{2(1-v^2)}{E}\left[r_1\tau \cdot {}_2F_1\left(\frac{1}{2},-\frac{1}{2};1;\frac{r^2}{r_d^2}\right) - \frac{r_d^2}{2r}(P+\tau) \cdot {}_2F_1\left(\frac{1}{2},-\frac{1}{2};2;\frac{r_d^2}{r}\right)\right],\ r_d \le r \le r_1 \\ \frac{2(1-v^2)}{E}\left[\frac{r_1^2}{2r}\tau \cdot {}_2F_1\left(\frac{1}{2},-\frac{1}{2};2;\frac{r_1^2}{r^2}\right) - \frac{r_d^2}{2r}(P+\tau) \cdot {}_2F_1\left(\frac{1}{2},-\frac{1}{2};2;\frac{r^2}{r_d^2}\right)\right],\ r \ge r_1 \end{array} \right\} \quad (2.3)$$

Using Wolfram Mathematica v.11 I plot the deformed substrate profiles predicted by equation 2.3 for various droplet sizes and substrate moduli. Specifically, in each case I plotted the droplet sitting on a 10 µm thick substrate with width five times the droplet radius, r_d, as shown in Figure 2.1. As in the case of an indentation,[69,70] if a depth of the deformation is less than 10% of the substrate thickness, the effect of underlying hard surface on deformation can be neglected. I calculated maximum vertical deformation of 1.4 µm, 0.5 µm, and 0.2 µm for G= 75 kPa, 220 kPa, and 500 kPa, respectively. Consequently, the 10 µm thick substrate can be assumed to be unimpacted by the underlying hard surface and use a deformation model for infinitely thick substrate. Also note that the PDMS sample thickness used for the condensation experiments is 350 µm for which, the deformation criterion is satisfied for all the cases. For simplicity, I simulated droplets with a 90° contact angle. Based on previous work,[66,67] this contact angle was assumed to occur at the tip of the deformed ridge (i.e. droplet shape consists of hemisphere imposed over the deformed substrate, see example in Figure 2.3b).

For droplets with radius smaller than the elastocapillary length, $r_{el} = \gamma/G$,[51,61] Yu *et al.*[65] analytical model predicts unrealistically deep substrate deformation (i.e. near column like droplet shapes with highly pulled up substrate around them). In contrast, Style *et al.* recently demonstrated that for droplets with $r < r_{el}$ the substrate deformation resembles that induced by a droplet condensed on a denser liquid surface.[23,61] In fact, this transition is not only limited to a liquid-solid interaction but is also true in case of hard solid-elastic substrate combination.[71] For the surfaces with G=75 kPa, 220 kPa, 500 kPa and 50 GPa the corresponding values of r_{el} are 960 nm, 330 nm, 140 nm, and 1.44 Å, respectively. For droplets below this scale, I derived the droplet geometry by assuming that the droplet three phase contact line obeys Neumann's triangle law of wetting.[72] Further details of the derivation of the droplet and substrate geometry used below r_{el} and above r_{min} are provided in Appendix A.

The combined droplet-substrate geometry was imported into COMSOL Multiphysics v5.2a. Following Chavan *et al.*,[63] I simulated a convective boundary condition at the liquid-vapor interface with constant interfacial heat transfer coefficient value of 0.8 MWm^{-2}K^{-1} (corresponding to the accommodation coefficient, δ, of 0.1 and saturation temperature of 373 K) and defined a constant temperature boundary condition at the bottom of the coating. Thermal conductivity of the substrate is 2 Wm^{-1}K^{-1}, which corresponds to an unstrained composite of PDMS with 50% liquid metal droplets by volume.[3,6] As in our previous work,[73] I calculated the heat fluxes for the simulated subcooling values through a numerical integration of equation 2.1 using Riemann summation.

2.3 Results and Discussion

2.3.1 Droplet nucleation density and departure radius

In agreement with Sokuler *el al.*[8] results, experiments here demonstrate that softening of the substrates with shear modulus below 500 kPa increases droplet nucleation density. This trend is evident in images of the samples taken 45 s after cooling was initiated shown in Figure 2.2a and the corresponding plot shown in Figure 2.2b. In particular, reduction in *G* from 50 GPa to 500 kPa has only negligible impact on nucleation density, which remains around 2.5x10^9 drops per m^2. In contrast, decrease in *G* from 500 kPa to 75 kPa increases the nucleation density more than four times from about 2.5x10^9 to about 10^8 drops per m^2. Sokuler *el al.*[8] argued that the increase in nucleation density occurs because decrease in the modulus reduces the liquid-vapor interfacial area and thus the free energy barrier for nucleation. From DWC heat transfer perspective, this mechanism is beneficial as it reduces the threshold radius between the two droplet populations. In quantitative terms, the values of r_e are 5.1 µm, 5.7 µm, 9.5 µm, and 10.2 µm for *G*=75 kPa, 220 kPa, 500 kPa, and 50 GPa, respectively. Thus, softening of the substrate by about half or more from the lower bound of the "hard limit" (i.e. 500 kPa) halves the threshold radius.

Next, I analyzed the effect of the substrate modulus on the droplet departure radius. The example images of droplets during or right prior to shedding from the vertically oriented substrate are shown in Figure 2.2c. As also indicated in the plot of the average departure radii against substrate modulus shown in Figure 2.2d, decrease of the modulus below 500 kPa increases the departure radius (from 1.8 mm at 500 kPa to 3.1 mm at 75 kPa). This effect stems from formation of highly irregularly shaped drops during coalescence on the softer substrates.[8] In particular, droplets become non-circular after coalescence because of the presence, and slow decay, of the wetting ridge deformation at the meeting point of the two constituent drops and around their receding contact lines.

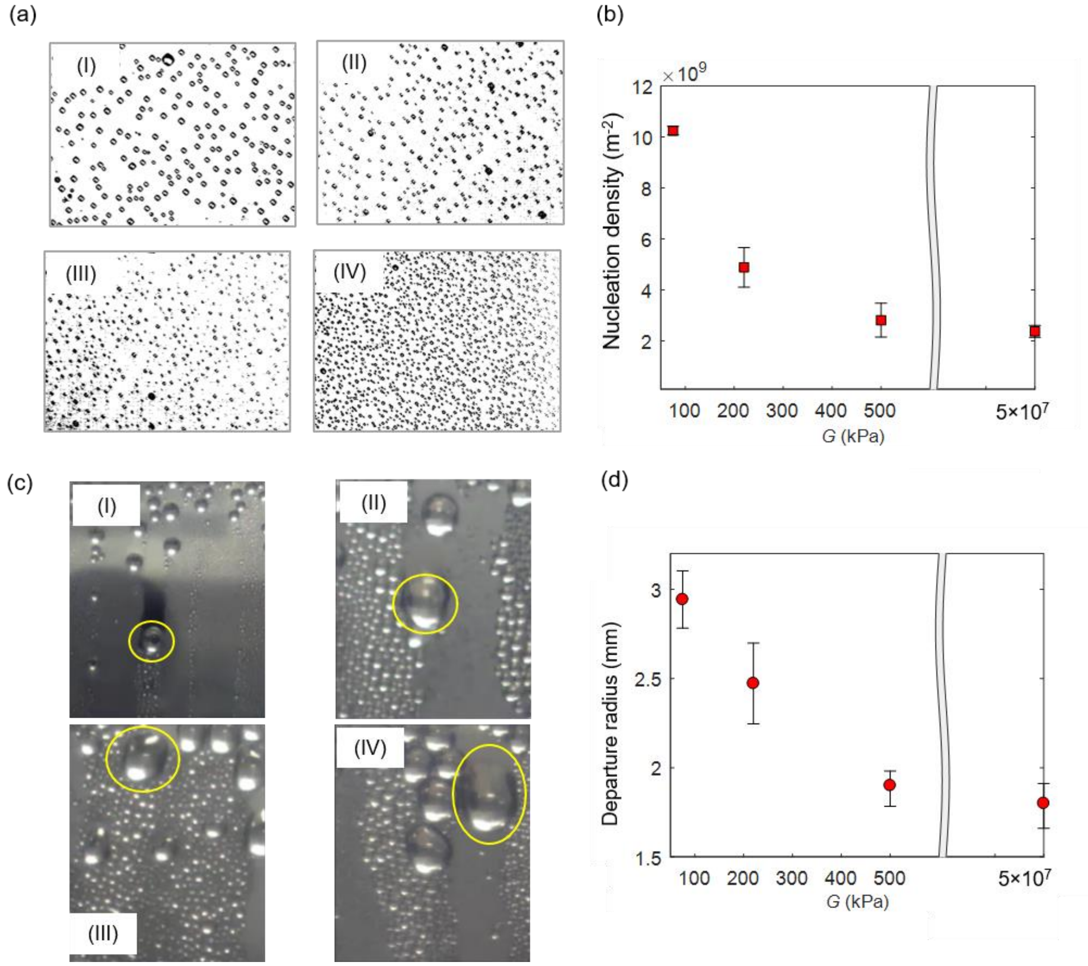

Figure 2.2 (a) Nucleation density at 45 s after initiation of cooling of horizontally oriented samples with shear modulus *G* equal to (I) 75 kPa, (II) 220 kPa, (III) 500 kPa, and (IV) 50 GPa, (b) plot of nucleation density as a function of the shear modulus, (c) example images of condensation on vertically oriented samples with departing droplets indicating with are

circles, and (d) plot of departure diameter as a function of shear modulus. In all cases, error bars correspond to 95% confidence interval.

Formation of the wetting ridge can even impede coalescence[74,75] and slows droplet movement through viscoelastic energy dissipation.[54,55] Both the highly irregular nature of droplets and their slower shedding velocity on the softer substrates are also evident in Movie 1 (Supplementary information of Phadnis and Rykaczewski[76]). In fact, both these behaviors result in the condensation mode on the sample with G=75 kPa beginning to exhibit some characteristics of the filmwise mode. Consequently, the sample with G=75 kPa (33:1 PDMS) are treated as the lower bound on which dropwise condensation can be sustainably achieved. Accordingly, our subsequent analysis is restricted to samples with G of 75 kPa or higher. In summary, the results in this section indicate high increase in the droplet nucleation density and departure size as the surface becomes softer than G of 500 kPa. However, these two results have impacts on heat transfer which are opposing in nature, thus the overall effect on DWC cannot be inferred without simulation of heat transfer through a single droplet and substitution of all values into equation 2.1.

2.3.1.1 Simulation of heat transfer through individual drops

The deformation of the substrate by the capillary forces imposed by a droplet (surface tension and Laplace pressure) cause two geometrical changes which have opposing effect on heat transfer. Specifically, the increase of liquid-solid interfacial area could increase conduction across the drop, while the additional thermal resistance posed by the liquid caused by the substrate depression could decrease it. The plot of the heat transfer rate across the droplets on substrates with varied modulus, q, normalized to that across droplets on silicone substrate, $q_{silicon}$, shown in Figure 2.3a indicates that the latter effect dominates the heat transfer process. Specifically, softening of the substrate decreases the value of $q/q_{silicon}$ ratio in all cases. However, the degree to which this ratio is decreased strongly depends on the droplet size. Larger droplets with radii of 100 µm and 1 mm are unaffected by decrease of the modulus from 50 GPa to 500 kPa and experience only a mild 20 to 25% reduction in the heat transfer rate with decrease of the modulus from 500 kPa to 75 kPa. In contrast, heat transfer rate through a 10 µm droplet is reduced by 25% and by 70% as the modulus of the substrate is reduced from 50 GPa to 500 kPa and 50 GPa to 75 kPa, respectively. Even more dramatically, same modulus reductions cause decrease of heat transfer rate through a 1 µm droplet of approximately 60% and 90%.

The significant reduction in heat transfer rate across smaller droplets can be explained through the role of the Laplace pressure ($2\gamma/r$) on the substrate deformation. The substrate depression below the coating-vapor interface is negligible for large droplets with radii of 100 µm and 1 mm because their Laplace pressure is low (about 1.5 kPa and 150 Pa for 100 µm and 1 mm respectively). This low level of pressure induces only a minor depression in even the softest tested coating (see Figure 2.3b), resulting in only the 20 to 25% heat transfer rate reduction in this case. In contrast, the Laplace pressure for droplets with radii of 1 µm and 10 µm is about 150 kPa and 15 kPa, respectively. This high pressure induces large depression even in the stiffer substrate with G of 500 kPa (see Figure 2.3b), leading to sizable increase in the liquid's thermal resistance (thus significantly reduced heat transfer rate). Note that the large deformation of the droplet with radius of 1 µm on substrate with modulus of 75 kPa shown in Figure 2.3b corresponds to the limit of applicability of equation 2.3 (i.e. droplet radius approaches the elastocapillary length). As explained in Section 2.3.1, in order to avoid unrealistic droplet shapes and substrate deformations, for droplets with radius below the elastocapillary length we simulated droplets with liquid-on-liquid geometry. In the next section, I evaluate how the decrease in heat transfer across droplets along with the increased nucleation density and the departure radii translate into impact of substrate softening on overall DWC heat transfer rate.

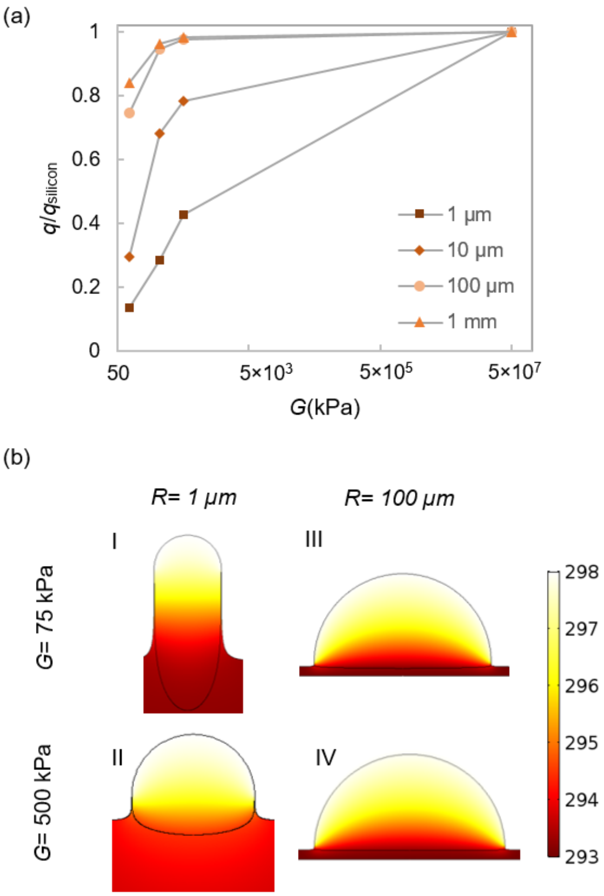

Figure 2.3 (a) Heat transfer rate across single droplets of different radii on substrates with increasing shear modulus and (b) the steady-state temperature profiles at the droplet-deformed substrate cross-section with subcooling of 5 K, interfacial heat transfer coefficient of 0.8 MW $m^{-2}K^{-1}$, and substrate conductivity of 2 W $m^{-1}K^{-1}$.

2.3.1.2 The effect of substrate softening on overall heat transfer

In order to estimate the effect of substrate modulus on the overall DWC heat transfer rate, I substituted the single droplet heat transfer rates obtained from simulations and the experimentally determined values of r_e and r_{max} into equation 2.1. More specifically, this procedure calculates how the heat flux per unit area of the condenser, q'' (Wm^{-2}), changes with subcooling for different values of the substrate's modulus. The plot in Figure 2.4a shows that the heat flux increases linearly with the subcooling and also increases with increase in the material's modulus. To elucidate the latter trend further, the variation of q'' with substrate modulus for a fixed subcooling of 5 K is shown in the inset of Figure 2.4a; a trend similar to that in Figure 2.3a can be seen here. Alternatively, the linear relationship between the simulated q'' and subcooling allows to calculate the DWC heat transfer coefficient from the slope of these lines. The plot in Figure 2.4b shows that the effective heat transfer coefficient increases with use of stiffer substrates. Specifically, the heat transfer coefficient for the softest substrate (G=75 kPa) is about 40% lower than that for silicon (G=50 GPa) as well as the stiffest silicone (G=500 kPa).

In order to separate the effect of droplet departure radius from nucleation density and heat transfer through individual droplets, I also calculated heat transfer coefficients for hypothetical silicone substrate set with departure radius independent of the shear modulus and equal to that observed on the hydrophobic silicon (i.e. 1.8 mm). Such substrates could likely be achieved in practice through swelling of the polymer with a lubricant. The plot in Figure 2.4a still shows a decrease of the heat transfer coefficient with substrate softening, implying that additional resistance posed by the substrate depression below microscopic droplets dominates the heat transfer process. Lastly, it was also observed the same trend when I altered the cutoff size between the droplets defined by Yu *et al.*[65] model and the liquid-on-liquid shape from $r < r_{el}$ to $r < 2\, r_{el}$ (see Appendix A for further details). This ensured that our results were not significantly impacted by applicability limits of the substrate deformation model we used.

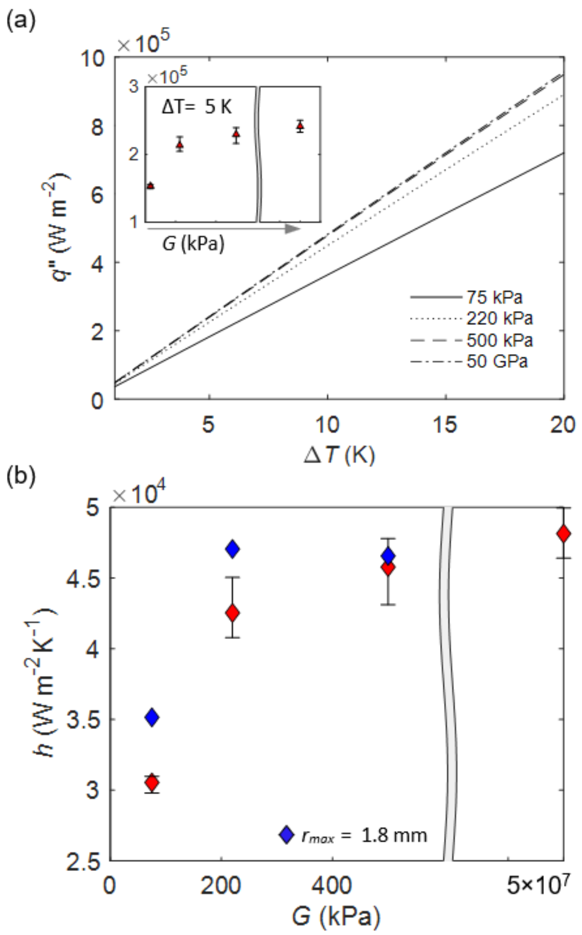

Figure 2.4 (a) Comparison of heat transfer rate per unit condenser area for different substrates and subcooling levels; the inset shows heat transfer rate per unit condenser area at subcooling of 5 K plotted against increasing substrate moduli from 75 kPa to 50 GPa, and (b) comparison of DWC condensation heat transfer coefficient, *h*, plotted against the substrate elastic modulus, *G*. Also plotted is the heat transfer coefficient (blue markers) for the condensation for hypothetical surfaces with departure diameter independent of the shear modulus and equal to that observed on the silicon surface.

2.4 The effect of Marangoni flows on dropwise condensation heat transfer

In the previous section we saw the effect of substrate modulus on dropwise condensation (DWC) heat transfer. While quantifying this effect, I inherently assumed conduction through condensate droplet to estimate $q_d(r,\theta)$ in equation 2.1. However, in this section we explore the effect of surface tension induced convection currents on DWC heat transfer.

2.4.1 Background

All current DWC models treat the droplets as a stagnant medium while neglecting any convective contributions. This assumption can be supported with simple scaling arguments. Specifically, one can determine whether or not buoyancy driven flow is occurring within an enclosure (here the droplet resting on a vertical wall) by calculating the Raleigh number [77]:

$$Ra = \frac{g\beta\Delta T L^3}{\alpha v} \tag{2.4}$$

Where, g is the earth acceleration constant, β is the thermal expansion coefficient, v is the kinematic viscosity, and α is the thermal diffusivity of the liquid. The plot in Figure 2.5a shows that even for subcooling, ΔT, of 50 K and a large drop radius of 1 mm, the Raleigh number is far below the critical threshold of ~1700 required for onset of buoyancy driven convection. Since this level of subcooling is extreme (i.e. not achievable in practice), buoyancy driven convection will not occur during DWC. In contrast to the absence of buoyancy driven convection, Beysens and co-workers recently pointed out that Marangoni flow could occur within condensing water drops under a wide range of conditions [78]. This thermocapillary phenomenon is caused by the temperature gradient along vapor-liquid interface of a drop that results into a surface tension gradient. The resulting spatial change in the surface tension causes unbalanced shear forces that drive a flow. The magnitude of this thermocapillary flow depends upon relative magnitude of surface tension and viscous forces and can be qualitatively estimated from the non-dimensional Marangoni number [78]:

$$Ma = \frac{\left|\frac{d\sigma}{dT}\right|\Delta T L}{\mu\alpha} \tag{2.5}$$

Where, $\left|\frac{d\sigma}{dT}\right|$ is the surface tension change with temperature, $L\ (\sim r)$ is the characteristic length, and μ is the dynamic viscosity. The plot in Figure 2.5b confirms Beysens and co-workers calculations [78], showing that the Ma can be greater than the critical value of 60 even for water droplets with small radii of 10 μm and 1 μm with respective small and moderate temperature differences of 1 K and 10 K. Consequently, Marangoni convection is likely to occur in majority of industrially relevant DWC processes. Note that it is important to distinguish the focus of current work, Marangoni convection during DWC of pure liquids on hydrophobic and omniphobic surfaces, from process sometimes referred to as Marangoni (or pseudo-) dropwise condensation that occurs during condensation of steam mixed with small addition of other vapors such as ethanol [79–82]. The presence of the secondary fluid in the latter process destabilizes a condensed film and causes it to break up into droplets.

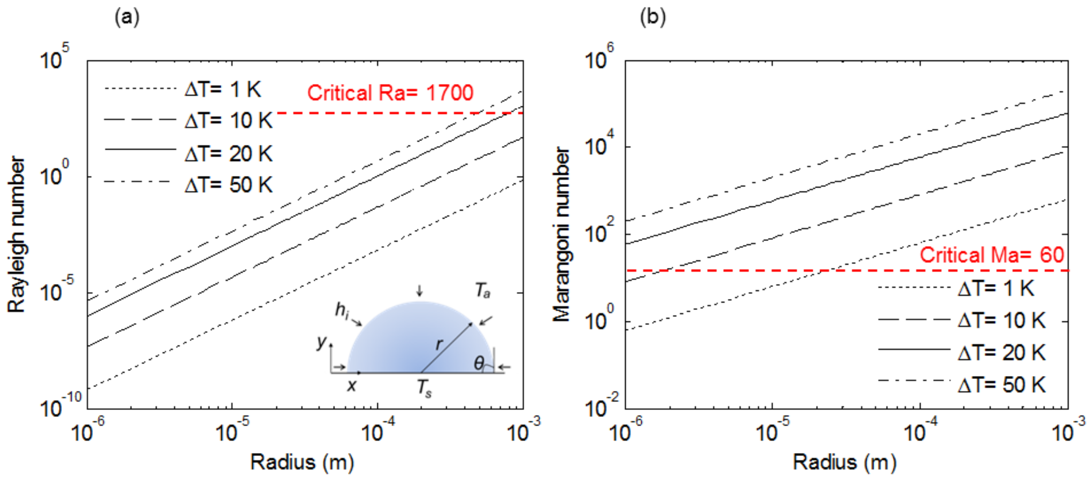

Figure 2.5 A comparison of non-dimensional numbers governing the flow-field inside condensing droplet on a vertical surface: (a) Rayleigh number and (b) Marangoni number. The schematic in the inset shows the droplet condensation problem formulation.

2.4.2 Hypothesis

In the present work, I theoretically quantify the effect of Marangoni convection on heat transfer across individual condensing droplets as well as its impact on the overall DWC heat transfer. Specifically, I use finite element model simulations to estimate the change in heat transfer that thermocapillary flow induces in condensing sessile drops with spherical cap geometry. Besides water, I also study heat transfer across drops of organic liquids whose DWC was recently demonstrated including toluene, ethanol, and pentane. Using a comprehensive set of FEM simulations in conjunction with previously described drop size distribution and steady-state model, I quantify the effect of thermocapillary flow on the overall DWC heat transfer.

2.4.3 Results and Conclusion

The details of the finite element model and assumptions therein, are provided in Appendix A (alternatively, in Phadnis and Rykaczewski[83]). Here I summarize the key takeaways from the work. To quantify the effect of Marangoni flows on dropwise heat transfer I first present the effect on heat transfer through a single droplet. This effect is presented in terms of the ratio of heat transfer predicted by the model when Marangoni convection is modeled along with conduction to that when only conduction is modeled.

Figure 2.6 summarizes simulated heat transfer ratio ($Q_{total}/Q_{conduction}$) as a function of subcooling for five drop radii spanning the 100 nm to 1 mm range. The rows of Figure 2.6 correspond to contact angles of 90º, 120º, and 150º; while the two columns correspond to saturation temperatures of 297 K and 373 K (results for 313 K are shown in Appendix A). As expected from the Marangoni number, the heat transfer ratio increases with the temperature difference and radius of the drops. We can also observe the heat transfer ratio increasing with the contact angle and saturation temperature, leading to a maximum 6-fold heat transfer enhancement for drop with 150º contact angle and radius of 1 mm subjected to 50 K subcooling at saturation temperature of 373 K. At these conditions, the maximum heat transfer ratio for drops with contact angle to 120º and 90º is reduced to 5.5 and 3, respectively. Lowering the saturation temperature for the same drop geometries reduces the maximum heat transfer ratio by about half (i.e. 1.5 at 90˚, 2 at 120˚ and 3 at 150˚). The reduction in the heat transfer ratio is attributed to the surface tension decreasing from 0.2 mN m^{-1} K^{-1} at 373 K to 0.15 mN m^{-1} K^{-1} at 297 K.

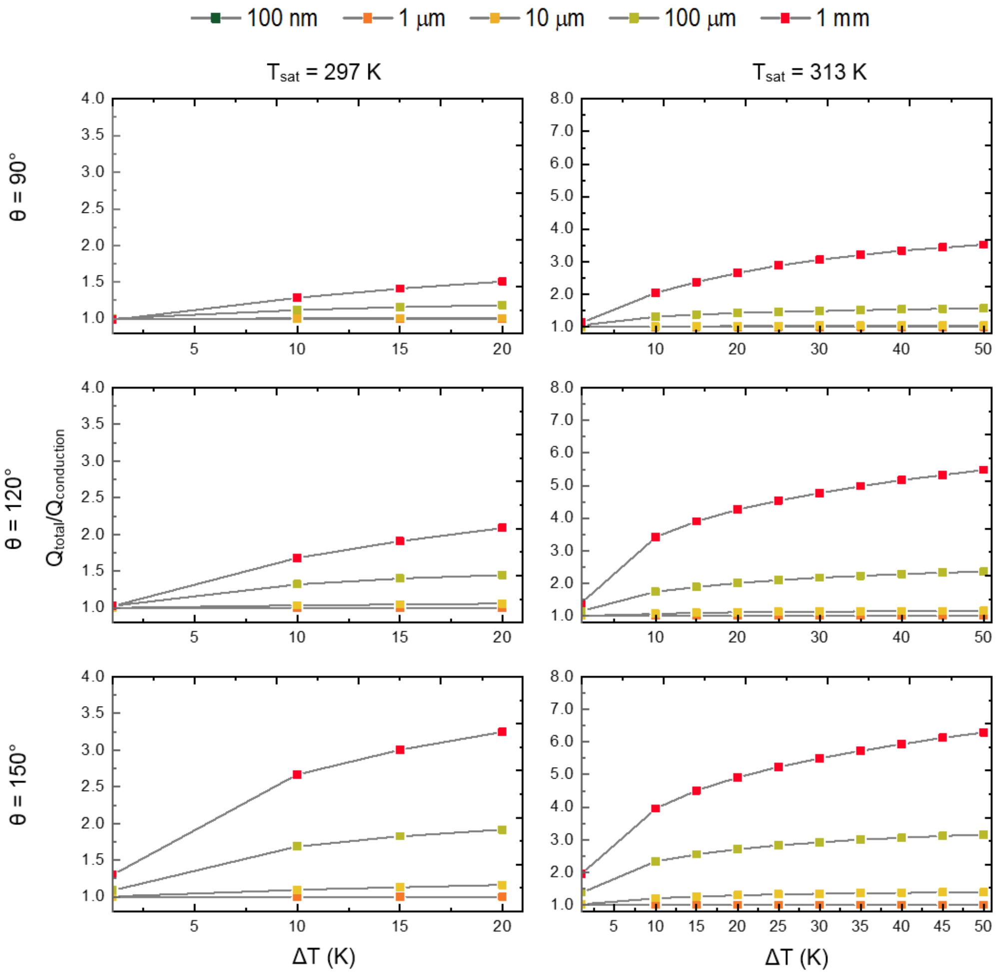

Figure 2.6 Heat transfer ratio, $Q_{total}/Q_{conduction}$, across water droplet for two saturation temperatures- 297 K (left column) and 373 K (right column) with contact angles- 90º, 120º and 150º.

Reduction of the drop radius from 1 mm to 100 µm similarly reduces the heat transfer ratio by half or more. Importantly, any droplet with radius 10 µm or smaller have, at most, a heat transfer ratio of 1.5. Note that, in some cases the presence of flow can decrease the heat transfer ratio below 1. For example, this occurs with 1 mm droplets having 90º contact angle at low subcooling (1 K).

Having established the impact of Marangoni flow on individual droplet heat transfer for various operating conditions, droplet sizes, contact angles etc., in this section, I use this information to estimate the total impact of thermocapillary flow on heat transfer during dropwise condensation. As described previously, the overall heat transfer rate per unit area (equation 2.1) is estimated through integration of single droplet heat transfer with the droplet size distribution. Instead of finding piecewise empirical fits to the FEM simulation data as Chavan *et al.*[63] (whose product with droplet size distribution equations needs to be numerically integrated), I computed the heat fluxes for the simulated subcooling values through a Riemann summation of the product of the FEM results and the droplet size distribution for given radius over the entire drop size range. The plots in Figure 2.7a and b show that for both the conduction only and the conjugate heat transfer simulations the heat flux increases linearly with the substrate subcooling, which allows for computation of the overall heat transfer coefficients from the slopes of these curves. These computed values shown in plot in Figure 2.7c are in reasonable agreement with previous experimental results [84]. Note that in order to isolate the effect of the Marangoni flow, a departure radius of 1 mm was used for all water droplet heat transfer calculations. Consequently, the heat transfer coefficient for the stagnant water droplet simulation decreases with increasing contact angle (and with that higher individual droplet resistance). If the departure radius is decreased for the 150° contact angle geometry to 100 µm and 7 µm, the conduction only heat transfer coefficient increases to 35.2 W m^{-2} K^{-1} and 64.3 W m^{-2} K^{-1}, respectively. The latter heat transfer coefficient for the superhydrophobic surface as well as its enhancement over the hydrophobic surface (~25%) is in the range of experimental values reported for jumping condensation [39].

Irrelevant of the liquid, the presence of the Marangoni flow enhances the overall heat transfer coefficient, albeit to varying extents. Figure 2.7d shows that for the organic liquids the thermocapillary flow enhances the overall heat transfer coefficient by a minor 2% to 12%. In the case of water with a fixed departure radius of 1 mm, the enhancement varies significantly from 2% for contact angle of 50º to 25 % and 29% for contact angles of 120º and 150º, respectively. Consequently, as clearly evident from Figure 2.7e, the surface tension rate of change with temperature is not the major factor determining the degree of thermocapillary enhancement of the heat transfer coefficient. Instead, Figure 2.7f shows that the contact angle of the droplets plays a dominant role. In particular, if the departure radius is similar, the percentage increase in the heat transfer coefficient for all the simulate fluids increases with droplet contact angle. It becomes significant (>10%) when the contact angle increases above 75º to 80º. This effect can be explained through insight from orevious results that show that the thermocapillary flow significantly enhances the heat transfer when the conductive resistance posed by the droplets is high (i.e. higher contact angle). Note, however, that the increase in droplet contact angle is typically characterized by decrease in the departure radius. Because the thermocapillary flow enhances the heat

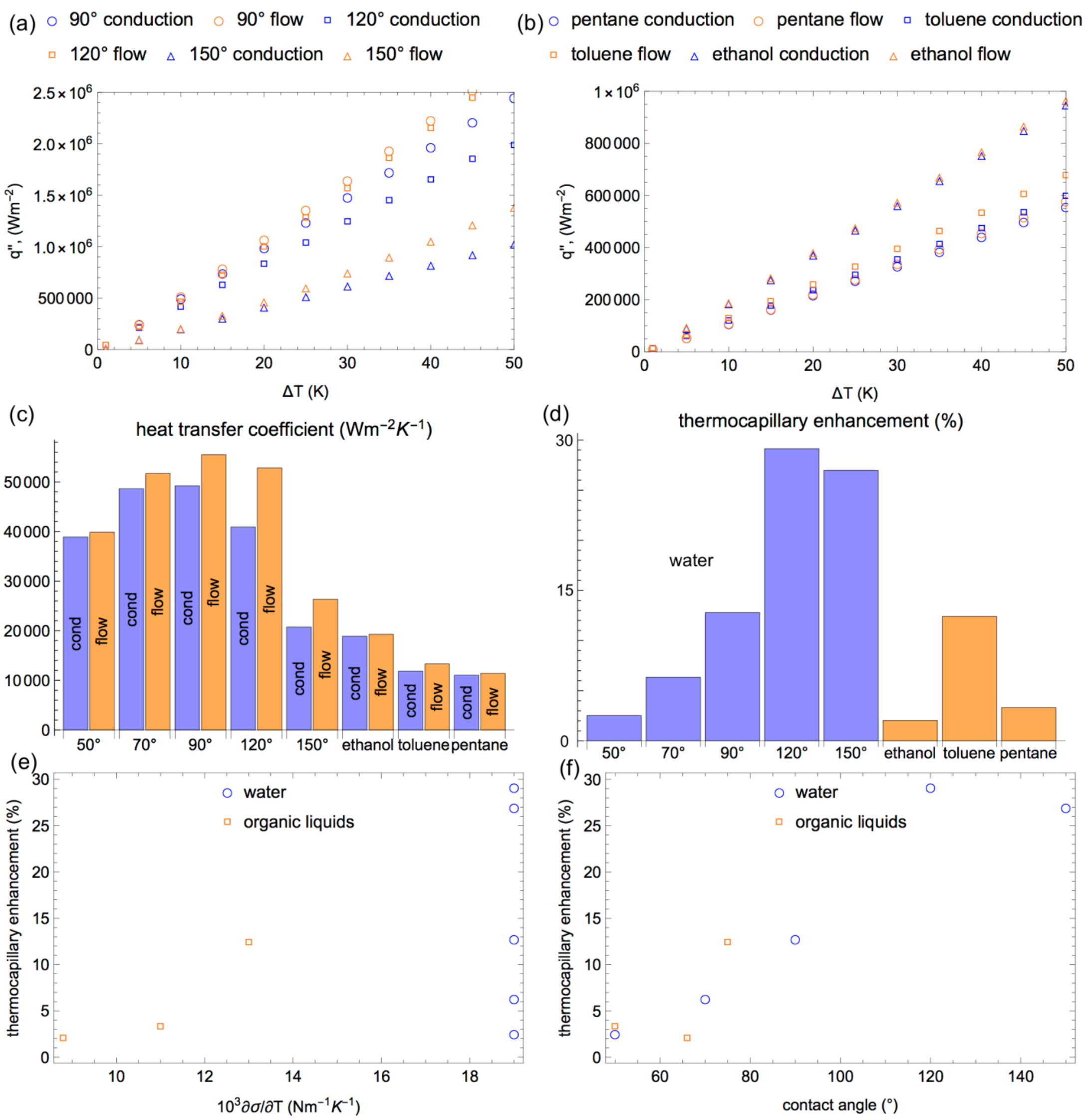

Figure 2.7 Thermocapillary enhancement of dropwise condensation heat transfer: (a)-(b) plots of simulated heat flux (q”) vs. subcooling (ΔT) with and without Marangoni flow for dropwise condensation of (a) water onto surfaces with various wetting properties and (b) of organic liquids onto fluorinated silicon wafer, and (c) heat transfer coefficients calculated from linear fits to data in (a) and (b); (d) to (f) percentage enhancement in the heat transfer coefficient due to thermocapillary flow as a function (d) liquid, (e) surface tension rate of change with temperature of the liquid, and (f) droplet contact angle. All liquid properties we calculated at atmospheric pressure with corresponding saturation temperature.

transfer across droplets with larger sizes, decrease in the departure radius will decrease the Marangoni flow heat transfer enhancement. For example, the thermocapillary heat transfer enhancement of a superhydrophobic surface with a contact angle greater than 150º, that promotes jumping condensation with a departure radius of 7 µm [39] is a negligible 4%.

2.5 Conclusions

In summary, the impact of substrate's mechanical properties on condensation heat transfer in the dropwise mode is investigated here. The overall DWC heat transfer coefficients are estimated by using the values of simulated heat transfer through single droplets and experimentally determined droplet nucleation density and departure size. These results show that softening of the substrates below a shear modulus of 500 kPa results in an overall reduction in the condensation heat transfer. This trend occurs despite a significant experimentally observed increase in the nucleation density on softer substrates and is primarily driven by additional thermal resistance of the liquid posed by depression of the soft substrate. In particular, I demonstrated that degradation of heat transfer persists even if the droplet departure radius is artificially decreased. Consequently, the experimentally observed increase of the departure radius caused by substrate softening contributes to heat transfer coefficient decrease but is not its primary cause. Thus, contrary to prior suggestions that softer surfaces can be better for condensation, these results show that it is not the case from droplet life cycle perspective.

In addition, I also explore the modeling of heat transfer in a sessile condensate droplet. I used FEM simulations of individual droplets in conjunction with classical steady-state dropwise condensation models to quantify the effects of modeling Marangoni convection on the overall heat transfer during this phase change process. The FEM simulations revealed that the thermocapillary flow can indeed provide a multi-fold enhancement in predicting the heat transfer across individual droplets. When integrated with the drop size distribution, the multi-fold increases in heat transfer across individual drops translate to a maximum ~30% increase in the overall dropwise condensation heat transfer coefficient. Thus, from a practical perspective, it is important to point out that the uncertainty in experimentally measured dropwise condensation heat transfer coefficients can be in similar range (e.g. 20%).[39] Thus, for practical heat exchanger design, the recommendation is to use the classical dropwise condensation models with droplets treated as stagnant medium with correlations that do account for the convective boundary condition at the liquid-vapor interface.[63]

SECTION II: DROPLET INDUCED BULK DEFORMATIONS

The recent Sarin gas attacks in Syria in 2015 and 2017 demonstrate that chemical weapon agents (CWA) are still a modern threat that requires protective materials. A vast majority of these chemical weapon agents (CWA) have very low vapor pressure and exist in the micro-droplet form rather than in the gas phase. The current protective measures act as an overclothing to be worn over the standard military uniform. These non-permeable measures provide protection against CWAs but at the same time, restrict the passage of perspiration vapor through them. The body temperature of the wearer rises beyond permissible limits within an hour of activity if the perspiration cooling is restricted.[85] Most current MOPP ("Mission Oriented Protective Posture") gear design prevents the evaporative cooling of the wearer and thus cannot be used for more than an hour without using auxiliary cooling equipment. Thus, thermoregulation poses a poignant challenge in designing these protective wearables. This issue can be addressed by a breathable, self-sealing fabric utilizing novel super absorbing polymers (SAPs) that can rapidly swell by absorbing the CWA and seal the fabric.

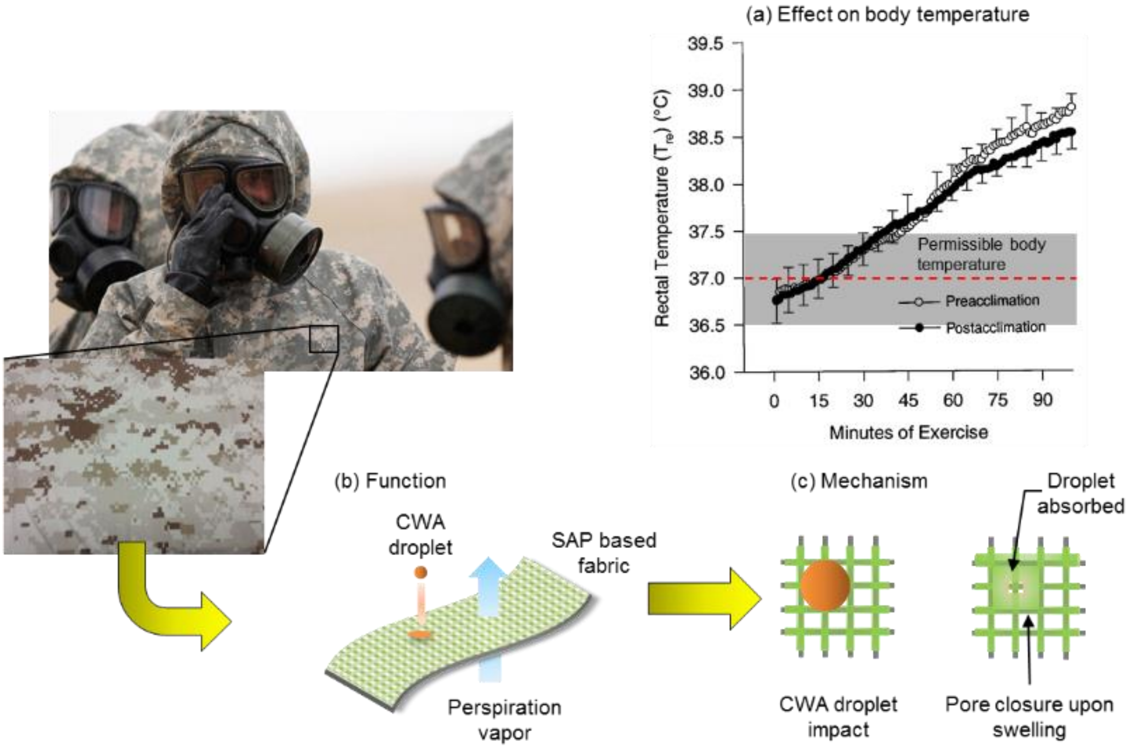

Figure II-1. Schematic illustration of the SAP-based breathable fabric: (a) body temperature rise due to lack of perspiration cooling,[85] (b) function of the breathable fabric and (c) Closing mechanism of the fabric based on SAP swelling. (Picture courtesy: www.fastcodesign.com).

The proposed working mechanism of this design in described Figure II-1. The SAPs after coming in contact with the CWA droplet absorb them to swell in large proportions. When embedded within the cloth (as shown in Figure II.1c) and with appropriate geometries, this swelling of SAPs can rapidly close the pores effectively blocking the passage of droplets. Since this mechanism is localized to the area of CWA contamination, it keeps unaffected areas of the clothing breathable for effective thermoregulation. Two design factors play key role in this process, *i.e.* swelling extent and swelling dynamics. The prior dictates the size of pore relative to the SAP that can be closed upon swelling and can be deduced based on the swelling ratio of the polymer, while the later indicates the time scales associated with this swelling and is governed by the diffusion of the penetrant (CWA in this case) in the SAP network. When the penetrant diffuses, the polymer chains expand elastically to accommodate the pressure exerted by the fluid. Thus, the whole mechanism can be considered to be a sequence of subprocesses in the following order- absorption of CWA droplet(s) by SAP, diffusion of CWA in SAP matrix followed by the deformation of SAP due to swelling.

Due to recent advancement in applications involving SAPs, a lot of effort has been dedicated in explaining the processes involved in swelling. Out of numerous different approaches, theory of poroelasticity is used most widely.[86] This theory treats the polymer and solvent mixture to be monophasic (termed as ‘gel’ throughout the text) and solves for concurrent fluid permeation and large deformation of the polymer matrix. The penetrant, after coming in contact with the polymer, diffuses in the matrix due to chemical potential gradient. The osmotic pressure increases as the fluid permeates in the polymer network voids and causes it to expand elastically. This process continues till the osmotic pressure is balanced by elastic forces and the gel is said to be in an equilibrium with the penetrant. Thermodynamically, the chemical potential of the penetrant inside the polymer is in equilibrium with the penetrant surrounding the polymer as shown in Figure II-2.

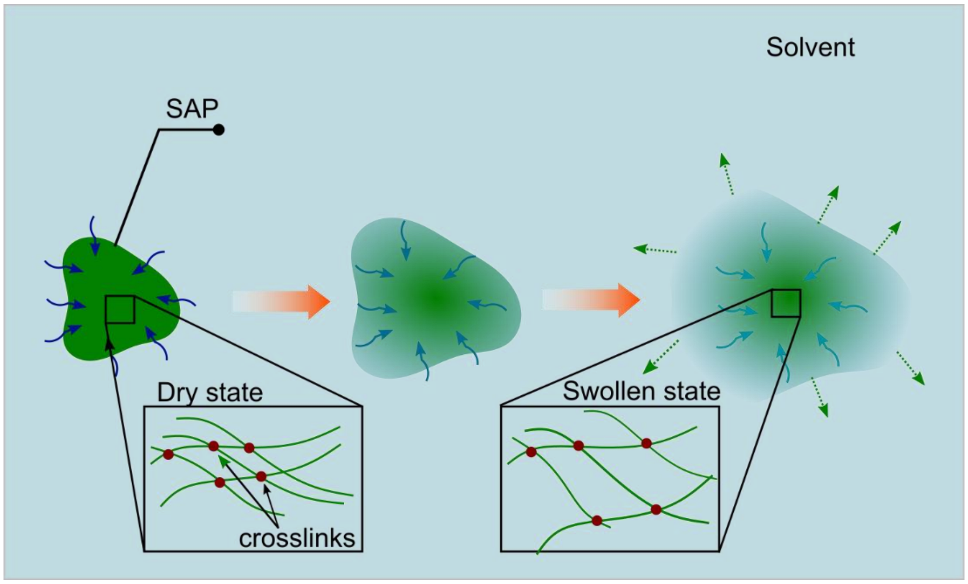

Figure II-2. A schematic showing the mechanism behind swelling of SAPs by absorbing the solvent (penetrant) which is being used to develop selectively permeable protective membranes in hazardous environments.

The mass balance describing the fluid permeation and force balance describing the deformation together forms a coupled partial differential equation (PDE) system. This system is further accompanied by minimization of thermodynamic free energy function and the physical constraints as a part of theory of poroelasticity. Solving such complex, multiphysics problem is a non-trivial task and requires dedicated mathematical and numerical treatments. Fortunately, in the recent past, a finite element (FE) based unified approach has been developed and advanced by several investigators to model the swelling behavior in polymers and hydrogels. We adapt this approach to our work for developing a predictive numerical model of SAP swelling by absorbing droplet(s) of CWAs. Thus, given a high-fidelity numerical model, they provide an important tool in studying the interactions of SAPs and penetrant (droplets). Not only it saves the time and cost of the experimental work, but it also provides important insights in the swelling behavior of SAPs that can be exploited for designing the composite fabric.

I developed this numerical model, validated it for different scenarios and used it to design the composite fabric and to predict its performance. The development of a preliminary model for swelling and its implementation in COMSOL Multiphysics is described in chapter 3 where I discuss swelling deformation in PDMS upon contact with n-hexane droplets. Using customized tests, I validate this model and predict the characteristic swelling of different geometries of PDMS under the impact of hexane droplet train. Additionally, I use time scale analysis to identify spatiotemporal regimes resulting in distinct boundary conditions that occur based on relative values of the absorption timescale and the droplet train period. I show that, when the two timescales are comparable, a variety of temporary geometrical features due to localized swelling are observed. I show that the swelling feature and its temporal evolution depends upon geometric scaling of polymer thickness and width relative to the droplet size. Based on this scaling, I showcase six cases of localized swelling and experimentally demonstrate the swelling features for two cases representing limits of thickness and width.

In the chapter 4, I extend the modeling methodology demonstrated on PDMS to poly(N-butyl-N-phenylacrylamide) (NBPA-33), a custom polymer developed to swell in target chemicals. Unlike PDMS or any elastomer, this polymer exhibits different characteristics which needs to be accounted for in the model. So, I describe how the material change is incorporated in the model. Specifically, I introduce a simple methodology to characterize solvent diffusion in the polymer based on an approximate model of the concentration dependent diffusion coefficient. This approach relies on a combination of gravimetry and poroelastic relaxation indentation (PRI) tests to measure the concentration-dependent diffusion coefficient, shear modulus, and Flory's interaction parameter, which are required to implement the predictive swelling model. My results show a close match between the model-predicted and measured swelling of NBPA-33 in *o*-xylene in terms of mechanical deformation, solvent front movement and solvent uptake with time. Based on these results, I also develop an analytical expression that predicts the polymer swelling based on gravimetry measurements alone.

In the final chapter, I use this validated model for NBPA-33 to explore the design space of the composite fabric. From my conclusions in chapter 3, I recommend a spherical shape of the polymer as an optimum geometry for the composite fabric while also suggesting the dimensional scale for the same. Next, I convert the axisymmetric model discussed in chapter 4 and to a 2-D model that simulates the composite fabric made up of NBPA beads attached to highly organized array of pores. Using this model, I establish a correlation between SAP bead size and the pore size that it can close. Using swelling dynamics results, I investigate lower and upper bound for the droplet 'encounter rate' that the composite fabric can withstand while remaining protective.

3 DROPLET TRAIN INDUCED SPATIO-TEMPORAL SWELLING REGIMES IN ELASTOMERS

3.1 Introduction

A crosslinked network of a polymer can absorb large amounts of suitable solvent and undergo elastic deformation, a phenomenon known as swelling.[87–90] Wherein, small molecules of the solvent migrate into the cross-linked network due to a difference in the chemical potential, to form a gel. Many natural materials including lentils, grains, fibers, and seeds exhibit this behavior in response to water present in their environment.[91–94] In industrial applications, solvent induced swelling of manmade polymers is used in numerous technical applications including drug delivery,[95] flow control,[96] actuation,[94,97,98] rapid containment of organic liquid spills,[99,100] and selective membrane filtration.[101,102]

Depending upon the extent of contact with the solvent, the polymer can undergo bulk swelling, where the polymer matrix is in contact with the solvent at all of its surfaces. In contrast, if only a part of the surface is in contact with the solvent, localized swelling is observed. Bulk swelling behavior in polymers has been extensively studied both experimentally[103–105] and numerically.[88,106–110] Droplet induced localized swelling has received a lot of attention recently. Recent experimental and numerical studies of droplet induced localized shape modulations and surface deformations have focused on bending and twisting of soft polymer structures,[111–115] formation of surface patterns and instabilities,[116–121] development of rapid responsive surfaces[122,123] etc. We note that due to negligible contact angle between swelling liquid and polymer, such shape modulation is distinct from elastocapillary deformations.[60,124–126] In addition, localized swelling of polymer structures upon impact of multiple sequential droplets (i.e. droplet train) has not yet been explored.

Repeated contact with the solvent at the same location induces swelling, deforming the polymer in an incremental fashion. The dynamics of this local swelling deformation can be compared to the formation of stalagmites due salt deposition. However, unlike stalagmites, the material expansion is restricted by the saturation of the polymer at the equilibrium. The droplet induced swelling of this kind is temporal in nature and, dependent on problem parameters, could either be highly localized or nearly uniform across the sample. Studying these swelling interactions can play an important role in designing materials for rapid and selective absorption of organic chemicals or oils droplets[100] and for designing protective gear that self-seals when exposed to droplets of harmful chemical weapon agents.[127]

In this work, I conducted a theoretical and experimental study of localized swelling behavior of polymer samples with axisymmetric geometries upon central impact of a train of solvent droplets. Based on timescale and geometric scaling analysis, different spatiotemporal swelling regimes are reported with distinct, temporary geometrical deformations. I experimentally reveal a subset of these temporary deformations and use this data to validate a high-fidelity numerical model that captures solvent spreading, absorption, and diffusion as well as polymer swelling. Owing to its robustness, I implemented coupled fluid permeation and large deformation theory in a finite element

(FE) analysis framework to describe the swelling behavior.[86,106,128–131] The FE framework captures the transient and nonlinear aspects of swelling and has been previously proven to be a highly efficient numerical technique.[108,110,132–134] The validated multiphysics model is implemented to reveal characteristic deformations within the entire swelling regime map.

3.2 Swelling regimes

When a single droplet of solvent comes in contact with a polymer, droplet spreading and absorption into the bulk polymer occur and induce swelling at and below the contact interface. In this event, the two relevant time scales are the liquid spreading time, t_s, and the time required for absorption of the droplet into bulk of the polymer, t_a. For surfaces that are wetted by the impacting droplet, t_s scales with R_d and is in most cases much shorter than $t_a \sim R_d^2/D$ (where R_d is droplet radius and D is the solvent diffusion coefficient in the polymer).[12] For example, for hexane droplet with $R_d =$ 1.3 mm impacting on a Polydimethylsiloxane (PDMS) surface, $t_s =$ 18-20 ms while $t_a =$ 12-15 s. When a train of droplets impinges on the polymer surface (see Figure 3.1a), another time scale set by the time-period between two droplets, t_{dt} (referred from now on as droplet train period), emerges. In case t_s is comparable to t_a (e.g. for impact of extremely viscous liquids), the summation of these parameters is the appropriate droplet train impact time scale. However, since in most cases absorption, not spreading, is the rate limiting process, I utilize t_a and t_{dt} as the two relevant time scales for analysis of the droplet-train and polymer sample dynamics. Depending upon the relative magnitudes of these times scales, three different regimes illustrated in Figure 3.1a arise:

- $t_a \gg t_{dt}$: In this case the droplet impacts the surface before the preceding droplet is completely absorbed. The progression of impacting droplets leads to flooding of the contact surface and eventually of the rest of polymer sample. While during the sample flooding time some deformation of the polymer occurs, this case can be approximated by a scenario where a sample is submerged in the solvent bath and allowed to swell freely. This case has been studied in detail and is described in the literature.[86,107,110,132]
- $t_a \ll t_{dt}$: In this case each droplet is completely absorbed, and the polymer may reach an equilibrium swelling condition before the next droplet hits. Thus, a train of droplets in this case leads to a quantized growth mode, with final state of each step corresponding to temporary equilibrium (i.e. uniform polymer stretching in all the unconstrained directions). Volumetric constraint is used to estimate the swelling ratio of the polymer, given the concentration of the solvent.[86] The incremental swelling ratio defined as the ratio of final to initial (dry) volume of the polymer due to absorption of n droplets in time nt_{dt} can be obtained by rewriting the volumetric constraint as

$$J_n = 1 + \Omega n c_d \tag{3.1}$$

  Where, c_d is the molar concentration when a single droplet is absorbed, n is the number of droplets. This swelling ratio can be further expressed in terms of the droplet parameters by rewriting the concentration c_d as

$$J_n = 1 + \frac{\Omega n V_d \rho}{M_w V_P} = 1 + \frac{n V_d}{V_p} \tag{3.2}$$

where, V_d is the volume of the droplet, V_p is the initial volume of the polymer, M_w, ρ, and Ω is the molecular weight, density, and molar volume of the solvent, respectively.

- $t_a \sim t_{dt}$: In this case, the time in-between droplet impact is comparable to liquid absorption time into the bulk polymer and it is difficult to predict polymer swelling dynamics based on timescale analysis alone. Consequently, focus of the attention is studying the localized swelling behaviors possible in this regime.

Pertaining to the third regime, let us now consider effects of the possible variations of the polymer sample width and thickness relative to the droplet radius. We can focus on a situation where the successive droplets impact the surface as soon as the previous one is absorbed into the bulk polymer. Consider an axisymmetric problem formulation, where a sessile droplet of radius R_d, is deposited on the center of upper planar surface of a cylinder with thickness δ and lateral dimension, L. Based on these three dimensions, the following six scenarios illustrated in Figure 3.1b are possible: (i) $R_d \gg \delta$ and $R_d \sim L$, (ii) $R_d \sim \delta$ and $R_d \sim L$, (iii) $R_d \ll \delta$ and $R_d \sim L$, (iv) $R_d \gg \delta$ and $R_d \ll L$, (v) $R_d \sim \delta$ and $R_d \ll L$, and (vi) $R_d \ll \delta$ and $R_d \ll L$. We note that all cases in which $R_d \gg L$ are trivial as the solvent will flood the entire polymer and are analogous to the $t_a \gg t_{dt}$ regime. Similarly, in cases (i) and (ii) volume of the polymer sample and the droplet are comparable, consequently impact of droplet train will result in sample flooding and bath-like swelling behavior, ending in polymer saturation after impact of a few droplets (depending on swelling capability of the solid). In the remainder of the cases (iii-vi), however, localized swelling with distinct geometrical deformations can occur.

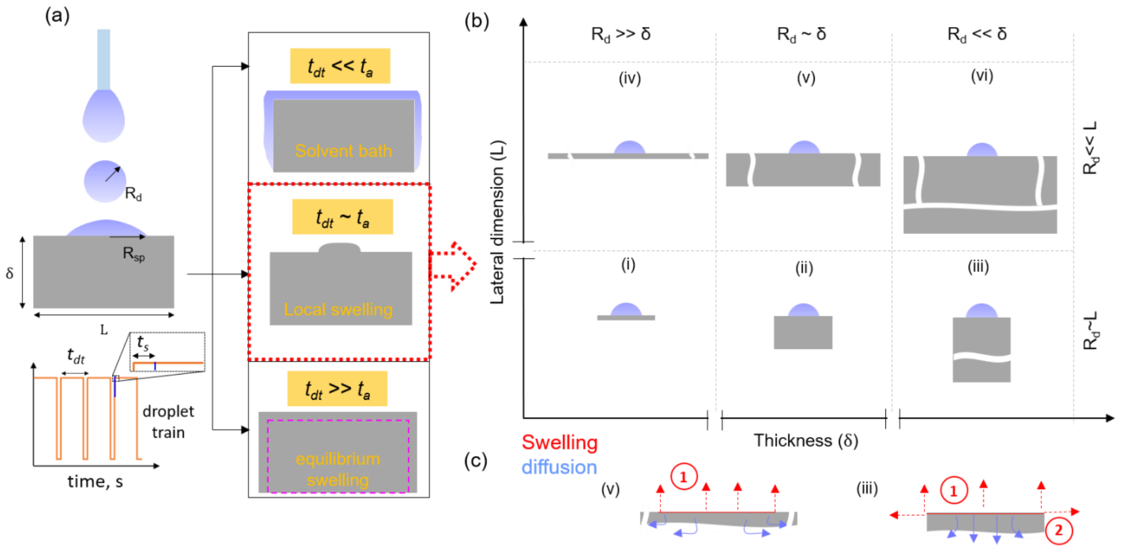

Figure 3.1 Regime map based on interactions between droplet and polymer surface: (a) regimes due to relation between the time scales associated with diffusion and train of droplets, (b) regime map based on geometric possibilities of the droplet and polymer surface for the case where the two time scales are comparable, and (c) close-up view of the expected near surface swelling and diffusion mechanisms in cases (iii) and (v).

In case (iii), diffusion of the solvent will occur predominantly along the thickness of the sample (i.e. negligible in-plane concentration gradients) and the swelling is expected to occur in both transverse and lateral directions (see Figure 3.1c-iii). In cases (iv) and (v), solvent will rapidly saturate volume below the droplet and its diffusion will gradually occur along the lateral dimension of the sample (see Figure 3.1c-v). Consequently, swelling will occur predominantly in the transverse direction below the liquid-surface contact region. In turn, case (vi) corresponds to a semi-infinite sample with isotropic solvent fluxes. The swelling in this case is expected to be qualitatively similar to case (v), but with significant decrease in the extend of the local sample deformation. In case (iv) microscopic crumpling and buckling of the thin polymer film ($\delta <$100 μm) occurs, irrelevant of the swelling induced by exposure to solvent drops or bath (see representative experiments in Appendix C). Thin film buckling has been studied extensively in literature,[116–118] and will not be elaborated on, further.

Based on the above qualitative arguments, we can expect the most distinct and substantial local deformations to occur in cases (iii) and (v). Consequently, these two scenarios provide the best study cases for high temporal and spatial resolution experimental characterization of the droplet-train induced polymer swelling dynamics. In the following sections, results of these experimental efforts and their use to validate the multiphysics FE model developed to simulate the swelling dynamics is described. The numerical model validated against experimental results from cases (iii) and (v) is subsequently used to study swelling characteristics in rest of the cases that were identified using scaling analysis.

3.3 Results and discussion

In this section, I describe the experimental and numerical studies of localized swelling dynamics in cases (iii) and (v) represented by central impact of n-hexane droplet-train on PDMS cylinder and disc, respectively. I selected this representative polymer-solvent pair because of the reasonably high degree of swelling[135] and availability of parameter required for modeling. The sample swelling dynamics was imaged using a custom-built droplet dispenser setup with a backlight and camera schematically illustrated in Figure 3.2a. I also developed an axisymmetric FE model of the process (see schematic formulation in Figure 3.2b) and compared it against the experimental data. Further experimental and numerical details are described in the Methods Section.

A key link between the experimental and numerical efforts, is the determination of the value of the diffusion coefficient of the solvent within the polymer. In particular, an accurate value of this parameter is needed in order to simulate correctly the temporal polymer shape evolutions due to droplet train swelling. Since very limited data was available in literature, I conducted two sets of experiments to measure the diffusion coefficient of n-hexane in PDMS cured with 1:33 cross-linker to base ratio. The results of these experiments are described first, followed by discussion of the cylinder and disc swelling studies, and numerical exploration of swelling dynamics in the remaining cases.

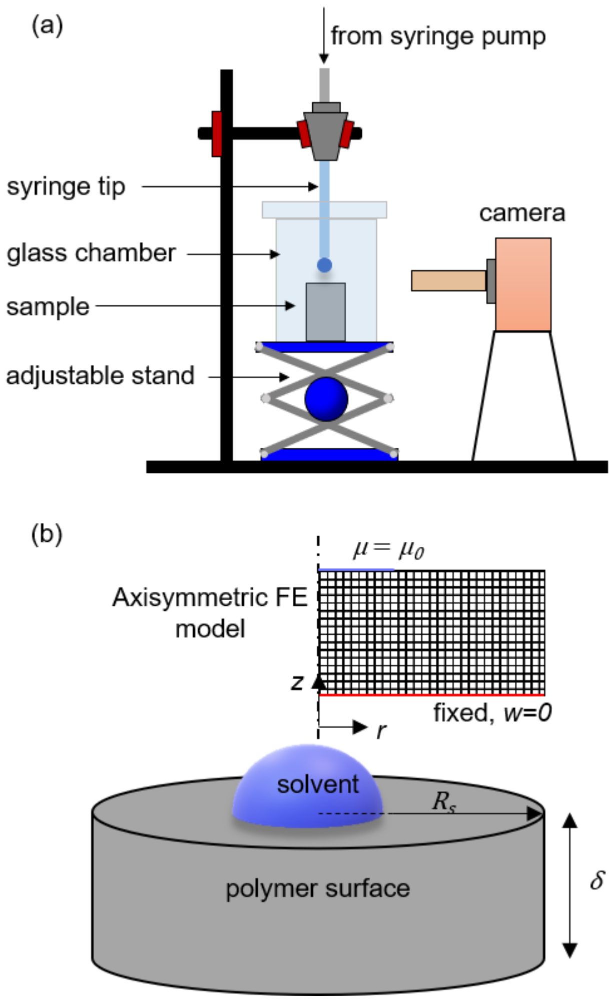

Figure 3.2 (a) Schematic of the experimental setup used to observe PDMS cylinder and disc swelling dynamics upon the impact of n-hexane droplet train and (b) schematic formulation of the corresponding two dimensional axisymmetric FE model domain and boundary conditions.

3.3.1 Measurement of diffusion coefficient of hexane in PDMS

To determine the diffusion coefficient of n-hexane in PDMS cured with 1:33 cross-linker to base ratio, I conducted polymer free swelling experiments in solvent bath and Attenuated Total Reflectance Fourier Transform Infrared Spectroscopy (ATR-FTIR).

In the free swelling experiments, I measured the mass of n-hexane absorbed by the PDMS sample with time (see Appendix C for further details). In the ATR-FTIR experiments, I measured the temporal change in spectral reflectance at the ATR crystal-polymer interface after top of the sample was exposed to the solvent. The diffusion coefficient can be determined from the onset time for reflectance change and the subsequent spectral dip evolution.[136–138] Since in these experiments swelling of the polymer film changed its thickness during the experiments, I could not apply the traditional closed-form formulas to determine the diffusion coefficient. Instead, D was estimated through iteratively adjusting its value in the FE simulations (adopted for geometries in these experiments) and comparing against experimental values. Using this approach, I estimated that $D = 6.1\times10^{-9}$ m^{2}s^{-1} provided best match of the simulated shape with free swelling data. This value is within the 2.6×10^{-9} to 7.0×10^{-9} m^{2}s^{-1} (95% confidence interval) range obtain from the ATR-FTIR experiments and is also in decent agreement with 4.0×10^{-9} m^{2}s^{-1} value previously reported in the literature (albeit for PDMS cured with 1:10 cross-linker to base ratio).[139] Consequently, in the subsequent studies we used $D = 6.1\times10^{-9}$ m^{2}s^{-1} as well as the lower and upper bounds of the 95% confidence interval from ATR-FTIR experiments.

3.3.2 Localized swelling of cylindrical sample (case iii)

As a representative scenario for case (iii), I studied central impact of 34 n-hexane droplets within a 10-minute period on a cylindrical sample of PDMS with radius $R_s = 5$ mm and thickness $\delta = 12.5$ mm. After contact, each droplet with volume of around 10 μL (pre-impact radius of around 1.3 mm) spreads within 18 to 20 ms and forms a puddle with radius of about 5 mm. Thus, the geometrical conditions for case (iii) of $R_d \ll \delta$ and $R_d \sim L = 2R_s$ are satisfied. In order to satisfy the temporal regime requirement of matching t_a and t_{dt}, I adjusted solvent flow rate so that droplets impinged on the surfaces every 12 to 15 s. This period corresponds to the experimentally measured time taken by the sample to completely absorb the sessile liquid puddle from each of the first few individual droplets (see Appendix C).

Representative sequential profile images of the cylinder swelling dynamics are shown in Figure 3.3a and Movie 1 (Refer to ESI of Phadnis *et al.*[140]). In agreement with the previous reasoning, the comparable size of the cylinder and the droplet puddle results in substantial swelling in both radial and axial directions. This process creates a spherical cap in the center of the sample, while the sides of the cylinder swell outwards radially, creating a profile resembling a "mushroom". During impact of the first few droplets the deformation of the top surface is slightly asymmetrical. This behavior eventually disappears as subsequent droplets spread out more evenly, resulting in symmetrical deformation after 10 minutes of the experiment.

The upper possible bound of the local deformation in the axial direction is defined by the equilibrium stretching ratio, λ_{eq}, which can be expressed in terms of the swelling ratio and is defined as $\lambda_{eq} = \sqrt[3]{J_{eq}} = \sqrt[3]{V_{swollen}/V_{dry}}$. From our free swelling experiments, I obtained $J_{eq} = 2.71$ and $\lambda_{eq} = 1.39$. Since we used PDMS base to cross-linker to ratio of 33:1, this value of $J_{eq} = 2.71$ is higher than previously reported value of

1.35 that were measured for base to cross-linker ratio of 10:1.[135] For the center of the cylinder, we observed the maximum equilibrium stretching ratio of 1.1. This value is although smaller than λ_{eq} but is close enough to give a good approximation.

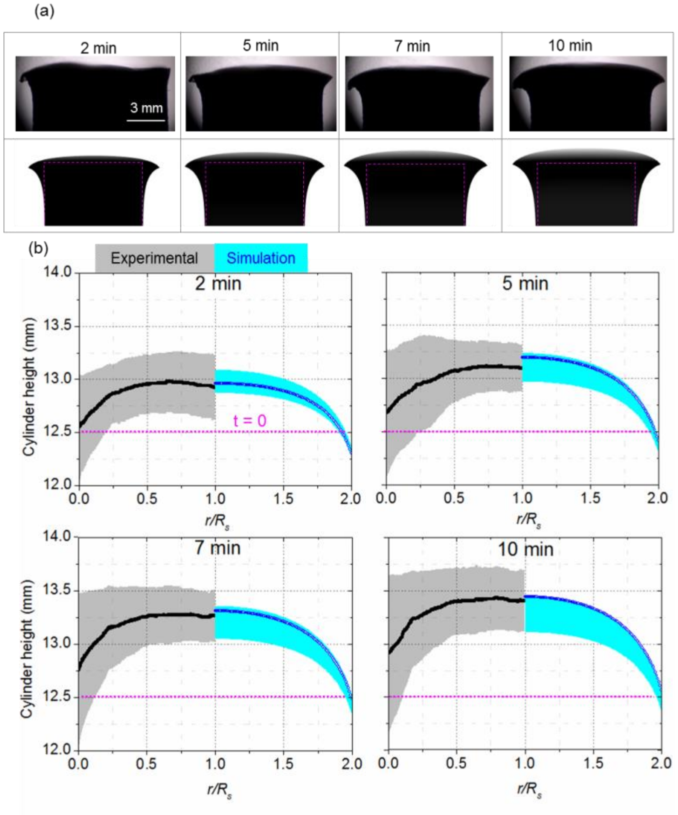

Figure 3.3 Characteristic swelling of cylindrical samples: (a) sequence of experimental (top row) and simulated (bottom row) cylinder deformation profiles at corresponding time points, and (b) comparison between experimental (left) and numerical results (right) showing temporal evolution of the top surface after 2, 5, 7, and 10 minutes. Error band for experimental results corresponds to 68% confidence interval of the experimental measurements, while the error band for numerical results stems from the variation in the measured diffusion coefficient implemented in the numerical simulations.

The bottom sequence of profile images of the simulated cylinder swelling dynamics shown in Figure 3.3a illustrate good agreement with experimental results. In more quantitative terms, the plots in Figure 3.3b show a close match between extracted profile of the cylinder obtained from experiments and simulations after 2, 5, 7, and 10 minutes of the experiment. The FE model was setup to simulate the test conditions by defining droplet contact boundary on the entire top surface of the cylinder as shown in Figure 3.2b. The pulsating nature of droplet contact on the top boundary was simplified by assuming constant contact with the solvent. This simplification matches with the studied scenario since every droplet meets the surface as soon as the previous one is absorbed. The only inputs into the model are the shear modulus (75 kPa for a PDMS mixed in 33:1 ratio),[59] Flory's interaction parameter ($\chi = 0.4$),[141] and experimentally measured diffusion coefficient of n-hexane in the polymer. The range of the presented simulation results corresponds to the diffusion coefficient range that we measured. The dark line in plots in Figure 3.3b corresponds to $D = 6.1\times10^{-9}$ m^2s^{-1} obtained in the free swelling experiments, while the cyan band corresponds to the 2.6×10^{-9} to 7.0×10^{-9} m^2s^{-1} result range (95% confidence interval) obtained from the ATR-FTIR experiments. As more droplets hit the substrate and swelling proceeds, the deformation profiles simulated with $D = 6.1\times10^{-9}$ and $D = 7.0\times10^{-9}$ m^2s^{-1} come closer and begin to overlap. After 10 minutes, surface of the cylinder gets saturated and reaches and equilibrium state, locally. Similar phenomenon is also observed for the swelling of thin film which is discussed next.

3.3.3 Localized swelling of the disc sample (case v)

As a representative geometry for case (v), I studied central impact of 28 n-hexane droplets within a 7-minute period onto a disc of PDMS with radius R_s =12.5 mm and thickness $\delta =$ 1 mm. In order to satisfy the geometric and temporal regime requirements, droplet size and solvent flow rate were maintained the same as in case (iii) experiments. These parameters allowed for satisfaction of the geometrical conditions of $R_d \sim \delta$ and $R_d \ll L = 2R_s$ as well as the temporal regime condition of matching t_a and t_{dt}.

Representative sequential profile images of dynamic swelling of the disc is shown in Figure 3.4a and Movie 2 (Refer to ESI of Phadnis *et al.*[140]). In agreement with the previous reasoning, the deformation has a "mesa" like shape that is highly localized to the region below droplet-surface contact and rapidly decays away from the edge of this area. The "mesa" height increases with time until polymer saturation is achieved after about 7 minutes of the experiment start. As shown by the bottom sequence of profile images of the simulated disc swelling dynamics in Figure 3.4a, the numerical results match well with experimental observations. The maximum λ_{eq} is 1.5 ± 0.1 which is close to the equilibrium stretching ratio of 1.4 obtained from free swelling test. This agreement stems from saturation of the sample throughout its thickness, which did not occur in case (iii). Note that the absorption of initial few droplets leads to temporary mechanical instabilities of the surface and its crumpling. This, in turn, results in shedding of a few droplets. Since these effects were not captured in the model formulation, I used a time averaged area to define the solvent contact with the polymer surface in order to accommodate the droplet shedding process. Using this area, the sample within the model imbibed nearly all of the experimentally dispensed solvent volume (97%) in 7 minutes. This minor alteration of the numerical boundary conditions results in small overestimation of the deformation in the early swelling stage (see frame of Figure 3.4b corresponding to results at 1 minute). Besides this minor disagreement, our simulations provide a good prediction of the swelling dynamics of cylindrical and disc polymer samples subjected to impact of a solvent droplet train.

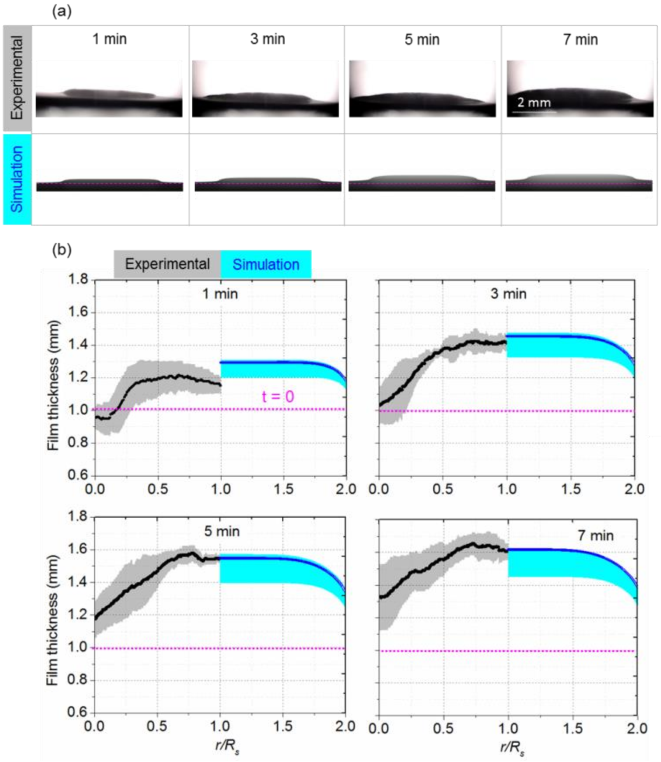

Figure 3.4 Characteristic swelling of film samples: (a) sequence of experimental (top row) and simulated (bottom row) disc deformation profiles at corresponding time points and (b) comparison between experimental (left) and numerical results (right) showing temporal evolution of the surface at 1, 3, 5, and 7 minutes of the experiment. Error band for experimental results corresponds to 68% confidence interval of the experimental

measurements, while the error band for numerical results stems from the variation in the measured diffusion coefficient implemented in the numerical simulations.

3.3.4 Localized swelling deformations in the matched timescale regime

Using the validated numerical model, I simulated n-hexane droplet-train induced swelling of the PDMS with geometries corresponding to the cases (ii) to (vi) discussed in the swelling regime section 3.2 (see Figure 3.1c). The simulated swelling deformations resulting from impact of 30 droplets are summarized in Figure 3.5a. Note that in simulating case (ii), the sample thickness was set to 4 mm instead of 1 mm as in case (v) in order to allow for the absorption of all of the 30 droplets (geometrical regime requirements are still satisfied since $\delta/R_d \approx 4 < 10$). Overall, I categorize the geometric form of the deformation into three characteristic shapes *viz.*, the “mushroom” for case (ii) and (iii), the “mesa” for cases (iv) and (v), and finally the “cap” for case (vi). The subtle difference between the “cap” and the “mesa” geometries can be realized by the curvature of the swollen front at the axis of symmetry. In case (iv), the deformation is flat for most part of the swollen region whereas in case (vi), the swollen region is curvilinear. Rapid local saturation of thin film results into deformation approaching uniform local swelling, while thick sample does not saturate and has strong concentration gradients in the sample. Similar behavior is observed with case (ii) to some extent where swollen region near the center is flat as opposed to case (vi). In all, the lateral extent of the sample relative to the droplet diameter plays the dominant role in determining the localized swelling geometry (“mushroom” vs. “mesa” and “cap”) and thickness dominates the further distinction between formation of “mesa” vs. “cap” shapes.

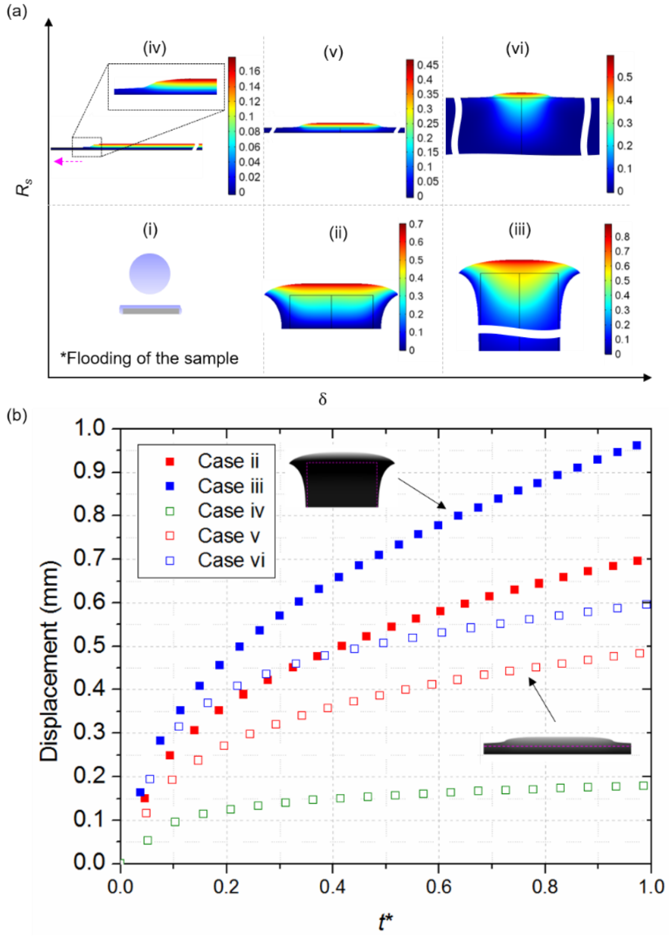

Figure 3.5 (a) Characteristic swelling deformations simulated using the FEA model for the identified geometric regimes and (b) plot of maximum surface swelling displacement in the axial direction against non-dimensional time for all the simulated geometries.

It was found that localized swelling deformations can also be distinguished based on the temporal evolution of the maximum displacement that occurs at the center of the droplet-surface contact region. The data in the plot in Figure 3.5b is presented in terms of non-dimensional time t^* that is obtained by scaling the time with the total absorption time for each case. Case (iii) shows maximum displacement of about 1 mm while case

(iv) shows the lowest swelling displacement of 0.18 mm. The latter case results in the lowest swelling because the sample is very thin compared to the droplet and saturates throughout its thickness rapidly. While being significantly higher than in case (iv), the maximum displacement in cases (v) and (vi) follow a similar saturation trend as case (iv). In contrast, the maximum displacement in cases (ii) and (iii) does not saturate. Consequently, the "mushroom" (cases (ii) and (iii)) shapes can also be distinguished from the "cap" and "mesa" geometries based on the temporal evolution of their maximum displacement.

3.4 Conclusions

A combined experimental and theoretical study of localized polymer swelling dynamics was performed under impingement of a solvent droplet train. Three swelling regimes were identified based on relative comparison of the droplet train period and absorption time. When these two time-scales are significantly different, swelling resembles either free swelling in a bath of solvent ($t_a \gg t_{dt}$) or quantized uniform growth with each step corresponding to a temporary equilibrium ($t_a \ll t_{dt}$). When these two time scales are comparable, appreciable localized deformation can occur near the impact of the droplets. In this regime, I identified six deformation scenarios that can occur based on the relative comparison between the droplet size and sample dimensions. Experimentally and numerically studies were performed on two of these cases in depth. Specifically, I studied localized swelling induced by central impact of about 30 droplets of n-hexane onto PDMS cylinder and disc (cases (iii) and (v)). I also developed a complementary finite element model of the process and validated it against the experimental results in terms of transient swelling deformation. Using only the diffusion coefficient as the fitted parameter, I obtained good agreement between numerical and experimental results. Using the validated model, I simulated the localized swelling behavior for all the geometrical cases identified in the match absorption time and droplet impact period regime. The results show that when the droplet size is comparable to the lateral size of the polymer sample, droplet train induced swelling results in formation of a temporary "mushroom" shape. In turn, when sample is much wider than the droplet size, droplet train induced swelling results in formation of temporary "mesa" and "cap" shapes. These results provide a starting point for analysis of droplet train swelling induced of more complex samples and development of functional devices based on such materials.

3.5 Materials and Methods

3.5.1 Numerical modeling

A custom finite element swelling model is developed in COMSOL Multiphysics v5.3. A concurrent fluid permeation and large deformation theory[86] combined with constitutive relation based on Flory-Rehner theory is considered here. Following Lucantonio *et al.*[110] and Caccavo and Lamberti,[133] we cast the following governing equations in the weak form using the weak form PDE module in COMSOL. For computational simplicity, we considered a 2D axisymmetric domain. It should be noted that the lateral dimension L of polymer will henceforth be expressed as R_s, the radius of the polymer sample in a 2D axisymmetric domain. A coupled system of equations governing diffusion, mechanical deformation, and volumetric constraint are solved simultaneously to obtain solution for displacement field $u(X,t)$, concentration field $c(X,t)$ and pressure field $p(X,t)$. A volumetric constraint is imposed to account for the fact that the total volume of the swollen matrix is the sum of dry polymer volume and the volume of solvent absorbed. Finally, a finite element problem can be formulated as follows: find u, p, c and boundary concentration c_b such that for any $\hat{u}$, $\hat{c}$, $\hat{p}$ and $\widehat{c_b}$ with $\hat{u}$ compatible with the boundary condition on bottom surface where $w = 0$, and $c = c_b$ on droplet contact area, it holds:

$$-2\pi \int (\boldsymbol{S}:\nabla\hat{u}) R\, dA = 0 \tag{3.3}$$

$$-2\pi \int \frac{\partial c}{\partial t}\, \hat{c}\, R\, dA + 2\pi \int \boldsymbol{h}\, \hat{c}\, R\, dA = 0 \tag{3.4}$$

$$-2\pi \int [J - (1 + \Omega\, c)] \hat{p}\, R\, dA = 0 \tag{3.5}$$

with a modified Dirichlet boundary condition defined in terms of boundary concentration c_b such that the chemical potential balance is satisfied on the boundary. Please note that the terms in bold are rank-2 tensors.

$$-2\pi \int (\mu_0 - \mu) \widehat{c_b} R\, dL = 0 \tag{3.6}$$

where, 1st Piola-Kirchhoff stress $\boldsymbol{S}$, chemical potential μ and solvent flux $\boldsymbol{h}$ is defined as-

$$\boldsymbol{S} = \frac{G}{\lambda_0} \boldsymbol{F_0} \boldsymbol{F_0^T} \boldsymbol{F} - p\ J\ \boldsymbol{F^{-T}} \tag{3.7}$$

$$\mu = RT\left(\log\left(\frac{\Omega J_0 c}{1+\Omega J_0 c}\right) + \frac{1}{1+\Omega J_0 c} + \frac{\chi}{(1+\Omega J_0 c)^2}\right) + \Omega p \tag{3.8}$$

$$\boldsymbol{h} = -\frac{c(X,t) D}{RT}\ \boldsymbol{F}^{-T} \boldsymbol{F}^{-1} \nabla\mu \tag{3.9}$$

where, $\boldsymbol{F}$ is the deformation gradient, G is shear modulus of the dry polymer (kPa), p is Lagrange multiplier and is equivalent to an osmotic pressure (Pa), Ω is molar volume (m^3 mol^{-1}), χ is the interaction parameter, $J = \det \boldsymbol{F}$ is the volumetric swelling ratio and D is the diffusion coefficient of the solvent in the dry polymer (m^{2}s^{-1}). Since the chemical potential reaches singularity at $c = 0$, a reference state is assumed where infinitesimal swelling ratio $J_0 = 1.003$ and concentration $c_0 = 23\ mol/m^3$ is defined in the numerical model. Naturally, all the calculations that follow, use this reference state as the initial condition instead of a dry state.[110]

A schematic of polymer droplet interaction and corresponding 2D axisymmetric FE model domain is shown in Figure 3.2. The droplet-surface contact area after the droplet has completely spread, is defined with the modified Dirichlet condition as explained earlier, while the rest of the boundary is defined with zero solvent flux, i.e., insulated. The bottom surface is constrained for any motion in axial direction ($w = 0$).

3.5.2 Polymer sample preparation

PDMS was prepared by mixing Sylgard 184 (Dow Corning) base with cross-linker in 33:1 ratio by mass. Red dye was added (KEDA dye) to facilitate visual distinction of the sample from the impacting solvent. The mixture was cast into cylindrical Aluminum molds and cured at 60 ˚C for 1 hour. Using same mixing procedure, uncured PDMS was coated on the glass slides of size 25 × 25 mm. As a result, uniform films of PDMS having thickness 0.9±0.1 mm were obtained.

3.5.3 Experimental Setup

Solvent droplets were produced using a stainless steel dispenser tip with internal diameter of 0.5 mm. In order to facilitate dispensing of smaller drops, the tip surface was made hydrophobic with a treatment of a mixture of Nitic acid (Sigma-Aldrich), water and ethanol (200 proof, Sigma Aldrich), and 1H,1H,2H,2H-Perfluorodecyl-triethoxysilane (Gelest). The steel dispenser tips were dipped in the solution for 1 hour and dried using a heat gun. This treatment reduced the extent to which hexane wetted the tip and made production of consistent sized droplets easier. The dispenser tip was connected to a 3 mL-syringe fitted onto a syringe pump (NE-300, New Era Pump Systems, Inc.) using a PTFE chemical resistant tubing and Luerlok connectors. To isolate the droplets from the effect of air movement inside the fume hood, the sample and the tip were situated inside a square glass container closed with a lid. This arrangement reduced the drift coming into the fume hood and ensured constant droplet frequency. To reduce the droplet evaporation, the sample was placed over a pool of hexane to create saturated vapor space. The evaporation time in this situation for a 10 µL droplet was measured to be > 2 min which is significantly higher than the absorption time (~ 12−15 sec) and hence the droplet evaporation was neglected. In order to prevent complex spreading dynamics, droplets were released from height of 5 mm above the sample, which resulted in small Weber number of 4 to 10 and negligibly small inertia effects.

3.5.4 Imaging

Nikon D5200 DSLR camera attached with an optical lens (489052, Navitar) was used for imaging the droplet impact. A monochromatic light source (Sola Eng, Litepanels) was used to backlight the setup. The images were post processed using MATLAB code based on Otsu's algorithm.[142] Please refer to Figure C3 in Appendix C for further details of the experimental setup.

4 PREDICTIVE MODELING AND CHARACTERIZATION OF SUPERABSORBENT POLYMER

4.1 Introduction

Superabsorbent polymers (SAPs) are a class of materials that swell in large proportions by absorbing penetrants upon contact. This property makes them attractive for a variety of applications including drug delivery,[95,143] filtration,[101,102] chemically responsive and biomimetic actuation,[114,122,144–146] and flow control.[96] These SAPs can also be functionally tuned to selectively absorb certain target materials in large quantities while rejecting others. We recently developed such functionalized SAP- low molecular weight poly(N-butyl-N-phenylacrylamide) (referred to as NBPA-33) that swells by absorbing targeted organic solvents while rejecting the water.[147] This selectivity of NBPA-33 can be exploited to develop specialized membranes and fabrics for protective clothing, chemical containment as well as thermoregulation applications. For developing these applications, quantitative prediction of NBPA-33 swelling dynamics is critical and could be achieved using a robust predictive numerical model. However, to develop such model, clear understanding and mathematical representation of underlying solvent diffusion and mechanical deformation processes is required.

As a first step towards developing a model to predict the swelling of NBPA-33, the transport of target organic solvent in the polymer needs to be characterized. The predominant difficulty in modeling the solvent diffusion in NBPA-33 is that since this polymer is having recently developed in the lab, any quantitative information on the solvent transport is unknown. Our initial experiments on the diffusion of *o*-xylene in dry

NBPA-33 shows a solvent front propagating with time. However, the analysis shows Fickian dominated diffusion with absence of any relaxation limiting process and, thus making the modeling such process unique to this solvent-polymer pair. To address this, I propose modeling a variable macroscopic diffusion coefficient, $D(c)$ as a function of solvent concentration, c.[148,149] This variable is typically modeled by integrating via appropriate functional form the mutual diffusion coefficient (D_0) that represents solvent mobility in the solid matrix and self-diffusion coefficient (D_s) which represents the solvent mobility in itself. While D_s is commonly available in the literature for most solvents, D_0 typically has to be measured for the specific SAP-liquid pair.

D_0 can be measured using Nuclear Magnetic Resonance (NMR) spectroscopy,[150–152] Fourier-Transform Infrared-Attenuated Total Reflectance (FTIR-ATR) among others,[153] and Raman spectroscopy.[154] Besides using of the latter method, I also develop an alternative approach for obtaining D_0 that has much simpler sample geometry requirements than the other techniques. Specifically, I implement a functional form for $D(c)$ that is based on D_s and the diffusion coefficient at equilibrium swelling state, D_{eq}. Physically, this value represents the mobility of the solvent in the polymer with an equilibrium solvent concentration. D_{eq}, along with mechanical and thermodynamic properties required for modelling of the swelling process, can be simultaneously measured through Poroelastic Relaxation Indentation (PRI)[155] of the swollen polymer gel. The D_0 obtained through Raman spectroscopy imaging as well as through our D_s and D_{eq} approach match closely. Using the data obtained from PRI tests, I also estimate the shear modulus of the dry NBPA-33 and use it to estimate the Flory's interaction parameter required by the constitutive model. Lastly, I show that substituting these values into the numerical model enables quantitative prediction of the experimental results of the transient solvent uptake, change in cylinder outer diameter due to swelling, and the solvent front propagation.

4.2 Characterization of swelling of NBPA-33

4.2.1 Gravimetry

The nature of temporal uptake of a solvent by a polymer is the simplest indicator to characterize the diffusion mode of solvent.[154,156,157] It has been established that the qualitative nature of the correlation between solvent uptake and time can be utilized to get a reasonable insight into the diffusion mode. A generalized equation is given by a power law as follows:[156,158]

$$\frac{M}{M_\infty} = kt^n \tag{4.1}$$

Where, M is mass of absorbed solvent at given time t, M_∞ is the mass of absorbed solvent at equilibrium (assumed to take place when $t \to \infty$), k is a proportionality constant and n is the time exponent. It should be noted that this equation only gives a rudimentary information about the diffusion process and appropriate care should be taken in drawing conclusion from its results.[158,159]

For these experiments, I prepared three cylindrical samples 3.8±0.1 mm in diameter and 27±1 mm in length. The aspect ratio of the cylinders was chosen so that diffusion can be approximated to be 1-D along the radial direction (see Appendix D). I prepared six such samples, three used for gravimetry and rest three for optical imaging explained in the next section. Placing the samples in an o-xylene bath, I measured the mass of absorbed solvent at different times using an analytical balance (Mettler-Toledo, ±0.1 mg). The transient increase in the imbibed solvent eventually stops when the system reaches an equilibrium. The equilibrium volumetric swelling ratio J_{eq} is calculated based on the ratio of dry and swollen sample weights as:

$$J_{eq} = 1 + \frac{\rho_p}{\rho_s}\frac{\bar{M}_\infty}{M_0} \tag{4.2}$$

Where, ρ_p and ρ_s are densities of polymer and solvent, respectively and M_0 is the mass of dry polymer sample. Note that $\overline{M_\infty}$ is used to indicate the total mass of the swollen polymer. Using equation 4.2, I calculate $J_{eq} = 5.4 \pm 1.5$. Note that the variation in J_{eq} is much smaller compared to that in the diffusion coefficient (in section 4.4) rendering no effect on modeling results and therefore, is not considered and we use the nominal value for the analysis.

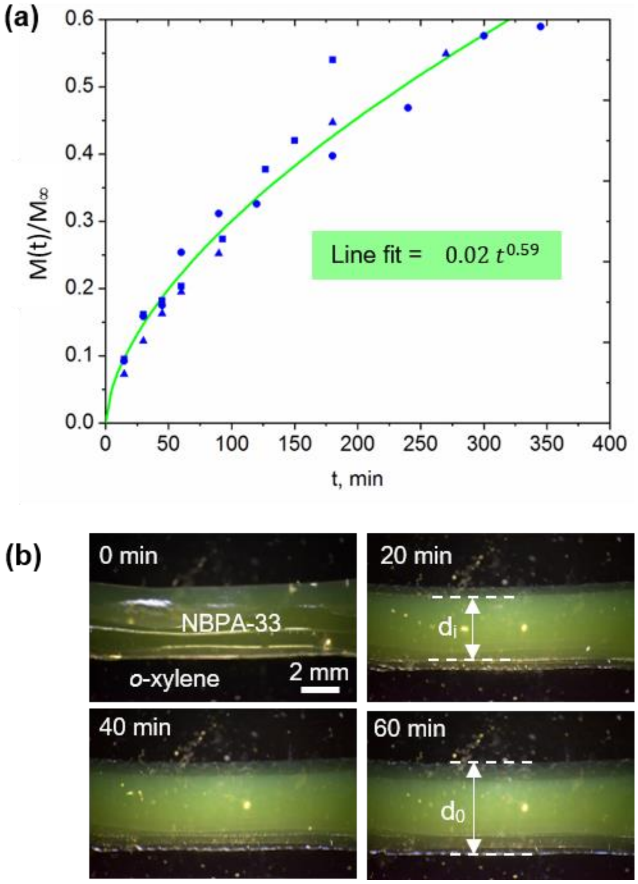

Figure 4.1 (a) A Plot of solvent mass uptake with time from three experiments (blue markers). The green line shows a power law fit of the data based on equation 4.1, (b) Optical images of NBPA-33 cylinder swelling in *o*-xylene. Propagation of the solvent front is shown at different times.

Figure 4.1a shows the temporal mass uptake by samples and normalized by the solvent absorbed at the equilibrium state, M_∞, during first 6 hours of the experiments. This has been done to satisfy the assumptions made in deriving equation 4.1, and restrict the data where $\frac{M}{M_\infty} < 0.6$ as recommended in several reports.[148,158,160] Using statistical analysis tool JMP, I fit the reduced experimental data of solvent uptake (till 0.6) in equation 4.1 and obtain the parameter value, $n = 0.59 \pm 0.06$. The error corresponds to the 95% confidence interval limit. It has been earlier reported that for the cylindrical samples, $n = 0.45$ indicates the ideal Fickian diffusion while $n = 0.9$ indicates the case II behavior.[159] In this case, $n = 0.59$ indicates some deviation from ideal Fickian diffusion but is still dominated by the Fickian transport. I confirm this by applying a method suggested by Peppas and Sahlin (see Appendix D) and show that the contribution of relaxation induced diffusion is less than 5% and thus can be neglected.[161] However, as mentioned earlier, due to assumptions in this analysis, I further verify our conclusions by observing the motion of the solvent front in the polymer samples.

4.2.2 Optical Imaging of solvent front motion

To verify the solvent behavior observed from the gravimetry results, I performed optical imaging of the swelling process by imaging the three cylindrical samples of NBPA-33 (approximately identical to those used for gravimetry) placed in a bath of *o*-xylene. As can be seen from Figure 4.1b, a solvent front separating dry polymer and swollen polymer gel can be clearly observed. Using ImageJ, I post-processed the images and measured the outer diameter (d_0) and inner diameter (d_i), which can be alternatively interpreted as the swelling deformation and location of the solvent front, respectively. The variation of d_0, d_i with time is plotted in Figure 4.4b where the decaying rate of solvent propagation can be clearly seen as opposed to constant rate in case II diffusion.[162,163] This observation also supports the argument about Fickian dominated diffusion of *o*-xylene in NBPA-33 observed from gravimetry. This conclusion plays a crucial role in numerically modeling the diffusion which is discussed next.

The case II behavior is explained by the rate limiting viscoelastic relaxation (VER) of polymer chains which takes significantly more time than diffusion. Whereas in this case, we expect the viscoelastic relaxation time of NBPA-33 to be smaller than the diffusion time scale. Thus, I treat this problem as a pseudo-Fickian diffusion with a sharp solvent front. Consequently, modeling of the transport and swelling processes requires a variable diffusion coefficient that is dependent on the amount of solvent.[164] Similar treatment was also suggested in the past by Crank to represent the Fickian diffusion with sharp solvent fronts.[164]

4.3 Mathematical description of variable diffusion coefficient

As mentioned in the previous section, the diffusion of *o*-xylene in NBPA-33 shows a sharp solvent front and can be modeled using variable diffusion coefficient. To model this process, I adopt the concentration-dependent diffusion coefficient approach.[148,160] Note that most of the work carried out in estimating the functional dependence of the diffusion coefficient on concentration has utilized microscopic and molecular dynamics treatments such as free volume theory,[165] jump model, etc.[166,167] To estimate the diffusion coefficient using these models a large number of parameters are required, which is an intricate and tedious task, especially for a previously uncharacterized polymer such as NBPA-33. Instead, I explore several macroscopic models available in the literature to relate the diffusion coefficient to the solvent concentration, which are more relevant to the development of a macroscopic predictive model of polymer swelling. The most commonly adopted model in these situations is known as the “Fujita” type model[168] which assumes exponential variation of diffusion coefficient. We adopt an analogous form as follows:

$$D(c) = D_0 \exp(A\ \phi_{solvent}) \tag{4.3}$$

Where, $D(0) = D_0$ and A is the proportionality constant. Note that we use solvent volume fraction, $\phi_{solvent}$, bounded between 0 and 1 instead of absolute concentration of the solvent for easier numerical treatment. The next model we consider assumes linear dependence of diffusion coefficient on the solvent and is known as the "Maxwell-Fricke" model. A simplified form of the equation is as given by:[169]

$$D(c) = \frac{D_s\,\varsigma}{\varsigma + 1 - \phi_{solvent}} \tag{4.4}$$

Where ς takes a value that depends on the approximate molecular shape (1.5 for rods and 2.0 for spheres). The third model we consider is the "Mackie-Meares" model, it assumes a quadratic functional form as follows:[169]

$$D(c) = D_s \frac{\phi_{solvent}^2}{(2 - \phi_{solvent})^2} \tag{4.5}$$

However, equation 4.5 shows that the mutual diffusion coefficient (when $\phi_{solvent} = 0$) is zero. This mathematical limitation is subverted in the numerical model which requires a non-zero concentration c_0 specified as the initial condition to avoid a singularity.[110] Further, the value of the mutual diffusion coefficient is highly sensitive to the initial concentration assumed. Instead, we define a similar functional form with quadratic variation as follows:

$$D(c) = D_0 + (D_s - D_0) * \phi_{solvent}^2 \tag{4.6}$$

From equations 4.3-4.6, note that the variable diffusion coefficient requires D_0 and/or D_s to be defined, depending on the function used. While D_s is the self-diffusion coefficient and is readily available in the literature, estimation of D_0 requires advanced imaging or spectroscopic methods. This can be a challenge, especially in polymers where the two diffusion coefficients can be several magnitudes apart unlike in elastomers. In the recent past, researchers have measured D_0 using advanced techniques like Raman Spectroscopy, pulse gradient spin echo (T1 relaxation) and spin-spin (T2 relaxation) Nuclear Magnetic Resonance (NMR) techniques, and Rutherford Backscattering, among others.[154] However, these techniques are more suitable for characterizing the case II behavior because of their large scan times (~10-30 min.). When diffusion is faster, these techniques either lose resolution or suffer from a low signal to noise ratio. These techniques also require significant sample preparation and analysis time. To avoid these limitations, I use an alternate simple approach to estimate the diffusion $D(c)$ using only D_s. I perform algebraic manipulations on equations 4.3 and 4.6 so that all four functional forms can be defined based on D_s. While doing so, I assume that the functional form is applicable for the entire range of the solvent volume fraction, (i.e. beyond equilibrium volume fraction) for mathematical convenience. This assumption may not be generally applicable to solvent-polymer systems, but as I show later, very well applies to NBPA-33 and *o*-xylene. Thus, appropriate care should be taken before applying such functional forms to model diffusion in polymer system.

By setting $\phi_{solvent} = 1$ when $D(c) = D_s$, equation 4.3 can be expressed in terms of D_s as follows:

$$D(c) = D_s \exp[-A(1 - \phi_{solvent})] \tag{4.7}$$

Now, to estimate the value of A, I use another boundary condition defined at equilibrium swelling. At this state, we can write $\phi_{solvent,eq} = 1 - \frac{1}{J_{eq}}$ and $D(c_{eq}) = D_{eq}$ to estimate A. By substituting this value back in equation 4.7 we can write the final form as follows:

$$D(c) = D_s\, exp\left[-J_{eq} \log\left(\frac{D_s}{D_{eq}}\right)(1 - \phi_{solvent})\right] \tag{4.8}$$

We perform similar algebraic transformations on the quadratic form defined in equation 4.6 to obtain the more convenient expression:

$$D(c) = \frac{D_{eq} - D_s\left(1 - \frac{1}{J_{eq}}\right)^2}{1 - \left(1 - \frac{1}{J_{eq}}\right)^2}(1 - \phi_{solvent}^2) + D_s \phi_{solvent}^2 \tag{4.9}$$

The advantage of this approach is in the fact that for most solvents the values of D_s are available in the literature and J_{eq} is available from gravimetry. Note that although D_0 was eliminated from these equations, the algebraic manipulation resulted in introduction of a new variable- D_{eq}. I define this coefficient as the equilibrium diffusion coefficient, i.e. the diffusion coefficient of solvent at swelling equilibrium. Crucially, estimating D_{eq} is a much easier experimental task that can be done using PRI, and, as I show in the text that follows, is sufficiently accurate to develop macro-models.

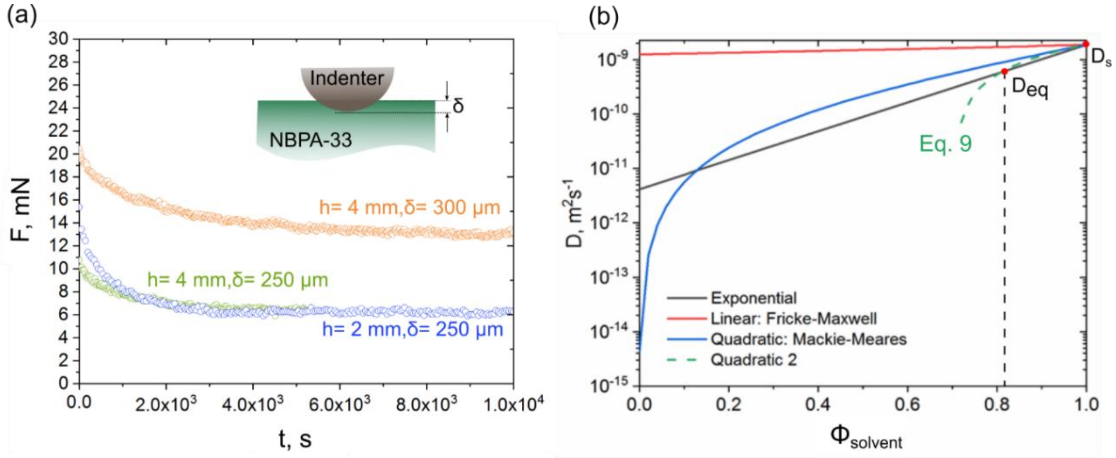

Figure 4.2 (a) Load response measured by the spherical indenter in PRI test. Three tests are shown which are used to fit equation 4.10, and (b) Plot of all the functional forms for diffusion coefficient under consideration. The quadratic form (dashed green line), defined by equation 4.9 results in negative values below $\phi_{solvent} = 0.7$.

4.4 Measurement of swelling parameters

4.4.1 Variable diffusion coefficient via $\mathrm{D_{eq}}$

PRI is a versatile and easy method to characterize a polymer gel in terms of its transport and mechanical properties.[170,171] In this method, a flat gel sample is subjected to a known, constant local compression using an indenter of desired geometry as shown in Figure 4.2a. The reactive load response, F, on the indenter is recorded with time. A polymer gel in the swollen state shows relaxation in the load due to the migration of solvent away from the indented region. Here, I use a spherical steel indenter of radius $R_{ind} = 4.8$ mm to indent the sample at different depths δ, and hold the indenter for 4 hours.

The plot in Figure 4.2a shows the change in reaction load, F against time for three representative samples. The load nearly instantaneously reaches a maximum value F_0 and then decays with time, eventually reaching a constant value of F_∞. Previous experimental-numerical studies on PRI suggest that the decay in the non-dimensional load takes up a mathematical form:[172]

$$\frac{F - F_\infty}{F_0 - F_\infty} = \exp\left[-\alpha \left(\frac{D_{eq} t}{R_{ind} \delta}\right)^{\beta}\right] \tag{4.10}$$

Where, F is the load at a given time, t, while α and β are geometrical functions of: R_{ind}, δ and sample thickness h.[172] I fit the experimental data obtained from five samples using equation 4.10 in JMP© Pro 14 and estimate the mean D_{eq} as $6.0 \pm 3 \times 10^{-10}$ m^{2}s^{-1}.

Having measured D_{eq}, I now substitute it into equations 4.8 and 4.9 and plot the variation of $D(c)$ with solvent volume fraction $\phi_{solvent}$, together with equations 4.4 and 4.5 in Figure 4.2b. The value of D_s is taken from the literature[173] to be $1.87 \pm 0.07 \times 10^{-9}$ m^{2}s^{-1}. It is evident from Figure 4.2b that the linear form overpredicts the diffusion coefficient and cannot be used to describe the solvent front motion. Also, the linear form is not constrained by the value of D_{eq} obtained from PRI tests. The Mackie-Meares quadratic form and the exponential form agree well for higher solvent volume fractions. For the lower values, however, Mackie-Meares form is prone to inconsistency and errors since it is heavily influenced by the initial volume fraction. This value is somewhat arbitrary from a computational point of view (and zero, experimentally), thus giving low values of $\sim 10^{-15}$ m^{2}s^{-1} as shown in Figure 4.2b. The second quadratic form (dashed line) gives negative diffusion coefficients below $\phi_{solvent} = 0.6$ and by extension, a linear form constrained by D_{eq} would do the same. This shows that the exponential form is qualitatively the best approximation for the diffusion coefficient when modeling non-ideal diffusion in glassy polymers during swelling. Now, we can estimate the values of D_0 from equation 4.8 by substituting $\phi_{solvent} = 0$. Using D_{eq} from PRI, D_s from literature, and J_{eq} from gravimetry, I estimate that $D_0 = 2.0 \times 10^{-11}$ m^{2}s^{-1}.

To validate the mathematical form of $D(c)$, I performed Raman spectroscopy imaging (RSI) to measure D_0. For this test, I made ~10 mm thick polymer sample in a quartz glass cuvette and analyzed the 1-D permeation of *o*-xylene along the length of the cuvette using a near Infrared light source (785 nm). I used two distinct peaks at ~1000 and ~700 wavenumber representing the polymer and the solvent respectively for detecting the solvent in the polymer matrix (see Appendix D). Using the time required for the solvent to propagate a known distance L in the sample I calculate the diffusion coefficient using following relation[164]-

$$D_0 = \frac{L^2}{6t} \tag{4.11}$$

Note that although this equation has been derived for the non-swelling polymer, the total experiment time is small enough (~ 25 min) for any considerable swelling to occur. This can also be verified by the gravimetry results which shows that $\frac{M}{M_\infty} < 0.1$ for first half hour for much smaller diffusion length scale (samples used in gravimetry were 3.8 mm in diameter), making equation 4.11 applicable to our RSI experiments. Using equation 4.11, I calculated $D_0 = 4.2 \pm 0.9\ \times 10^{-11}$ m^{2}s^{-1}. This value is very close to the D_0 estimated using equation 4.8. In other words, the assumption of extrapolating the exponential form given in equation 4.8 for the solvent volume fractions greater than the equilibrium state holds good for this pair of the polymer and the solvent. Thus, when we back-calculate D_s from D_0 measured in RSI and D_{eq} from indentation we get $D_s = 1.2 \times 10^{-9}$ m^{2}s^{-1} which is very close to the literature value.[173]

4.4.2 Shear modulus

Results from PRI can also be used to estimate the shear modulus of the swollen gel. The instantaneous load response of the gel when the indenter reaches the prescribed depth is used to estimate its mechanical properties, assuming it behaves like an ideal incompressible material over a short initial period. Based on previously reported semi-empirical/numerical formulations, the shear modulus, G_s, of a gel is calculated as follows:[172,174]

$$G_s = \frac{3F_0}{16\,\delta\,\sqrt{R_{ind}\,\delta}\,f_p(\sqrt{R_{ind}\delta}/h)} \tag{4.12}$$

Where f_p is a function of indentation radius, depth and gel film thickness and is given by-

$$f_p\left(\frac{\sqrt{R_{ind}\delta}}{h}\right) = \frac{2.36\left(\frac{\sqrt{R_{ind}\delta}}{h}\right)^2 + 0.82\left(\frac{\sqrt{R_{ind}\delta}}{h}\right) + 0.46}{\frac{\sqrt{R_{ind}\delta}}{h} + 0.46} \tag{4.13}$$

This approximation accounts for the deviation from the Hertzian load in thin films where the stiffness of the substrate affects the stress field at the indenter-film interfacial region. From the PRI experiments performed, I estimate $G_s = 14 \pm 6$ kPa using equation 4.12.

However, this modulus represents the modulus of the swollen gel. As the polymer swells, the modulus drops with solvent concentration and rubber deformation theory[175] uses shear modulus of the dry network to define the free energy. Thus, I next estimate the shear modulus of the dry NBPA-33, G_0 based on its modulus in the equilibrium swelling state, G_s. The change in modulus of the polymer with swelling depends on the type of polymer. Since I showed that the NBPA-33 shows dominatingly leathery characteristics, I assume that it follows the trend of modulus change observed in elastomers which given as[176]-

$$G_0 = G_s\, J_{eq}^{1/3} \tag{4.14}$$

Using this correlation, I estimate approximate values of $G_0 = 24 \pm 10$ kPa allowing for the variations in measurement of G_s. Note that, this assumption may not be completely accurate, but the lack of limiting viscoelastic relaxation and the absence of zero-order solvent uptake, makes it a reasonable assumption to develop a macroscopic deformation model. It is also to be noted that, the high variation in shear modulus is less significant in terms of numerical modeling since the combination of shear modulus and interaction parameter χ governs the swelling which is restricted to the equilibrium swelling ratio estimated in gravimetry. I describe this process in the following text.

4.4.3 Interaction parameter

Once the shear modulus is obtained, an important non-dimensional parameter known as Flory's interaction parameter χ can be estimated using equilibrium swelling data. A steady-state, equilibrium equation for swelling is given by[110]

$$RT\left[log\left(\frac{J_{eq}-1}{J_{eq}}\right)+\frac{1}{J_{eq}}+\frac{\chi}{J_{eq}^2}\right]+\frac{G_0\Omega}{\sqrt[3]{J_{eq}}}=0 \tag{4.15}$$

Where, R is universal gas constant, T is the temperature and Ω is solvent molar volume. I solve equation 4.15 iteratively to estimate χ so that for a known G_0, we get the given value of J_{eq}. Based on the nominal values of $G_0 = 24$ kPa and $J_{eq} = 5.4$, I estimate $\chi = 0.55$. Since the variation in J_{eq} is negligibly smaller compared to the measured variation in G_0, we can neglect this variation. Mathematically, for any given value of G_0 we can estimate a corresponding value of χ from equation 4.15 such that J_{eq} remains the same and we get pairs of G_0 and χ all resulting in the same J_{eq}. I verified for the three such pairs of $(G_0, \chi) = (24, 0.54), (34, 0.55), (14, 0.56)$ has only negligible effect on transient swelling predictions (see Appendix D).

4.5 Results and Discussion

4.5.1 Numerical modeling

Next, using the swelling parameters- $D(c), G_0, \chi$ estimated from the characterization tests, I develop a finite element model to numerically simulate the swelling experiments. The model is based on the theory of poroelasticity which requires solving force and mass balances with a volumetric constraint. The constitutive recipe is based on Flory-Rehner theory of rubber elasticity and energy of mixing. I cast the balance laws subjected to a volumetric constraint in the weak form and implement them in *weak form PDE* module in COMSOL multiphysics v5.3a. The details of the equations and the numerical procedure are provided in our previously published work.[140]

However, I note the key differentiation from our previously reported model in that, I use the *non-linear solid mechanics* module in COMSOL instead of casting a force balance law (equation 1 in Phadnis *et al.*[140]). This requires only the entropic part of the free energy function W_{el} to be defined in COMSOL's custom *hyperelastic material* module and I define it as:

$$W_{el} = \frac{G_0}{2}\left[I_1(\boldsymbol{C_{el}}) - 3 - 2\log(I_3(\boldsymbol{C_{el}}))\right] \tag{4.16}$$

Where, $I_1(\boldsymbol{C_{el}})$ and $I_3(\boldsymbol{C_{el}})$ are 1st and 3rd invariants of elastic right Cauchy-Green tensor $\boldsymbol{C_{el}}$, respectively. I first verify this modeling by comparing the numerical results with previously published work[177] (see Appendix D) and then use the experimental data from characterization tests to validate the model.

4.5.2 Model Validation

Next, I validate the numerical model using a set of optical and gravimetry experiments discussed in the previous sections. First, I include the diffusion coefficient, the shear modulus and the Flory's parameter obtained from the indentation tests and gravimetry in the model. Then with substitution of these parameters, I simulate our optical and gravimetry experiments in COMSOL. The solvent flux is approximated with a variable diffusion coefficient defined based on equation 4.6. Using this numerical model, I then estimate the change in outer radius and solvent front propagation in the cylinder *i.e.* $d_0/2$ and $d_i/2$, respectively as well as solvent uptake by the sample with time.

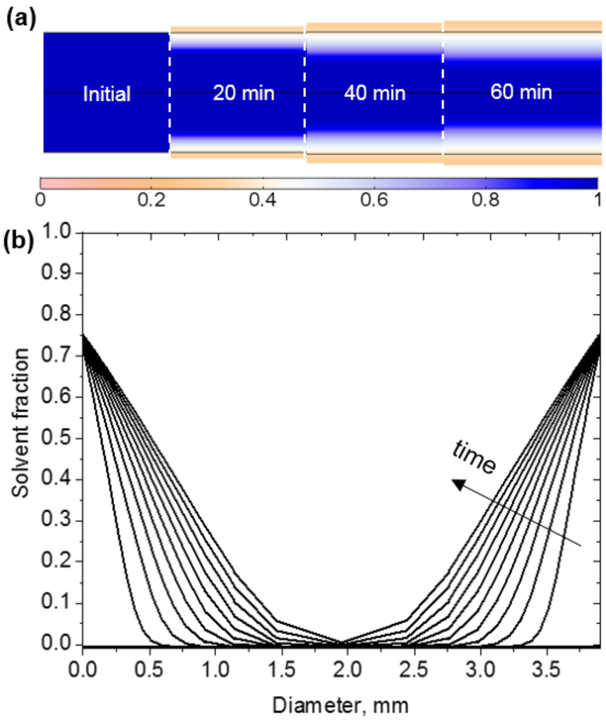

Figure 4.3 (a) 2D contour plot of the polymer volume fraction of NBPA-33 in cylindrical samples at different times from COMSOL simulation (legend: polymer volume fraction), (b) Solvent volume fraction profile along the NBPA-33 cylinder diameter at different times till the solvent front disappears.

The plots in Figure 4.3a and b show the solvent volume fractions at different times of the numerical experiment. The simulated and experimental (Figure 4.1b) results show qualitatively similar inward propagation of the solvent front. The corresponding values of solvent volume fraction along the cylinder diameter at different times are plotted in Figure 4.3b. This profile is a direct consequence of the diffusion coefficient defined based on equation 4.6. From our gravimetry results we assumed the viscoelastic relaxation timescale to be smaller than the diffusion timescale. Thus, the resulting profile in Figure 4.3b shows the presence of the solvent front but does not show saturation of the polymer behind it, unlike the mechanism in case II (evident from the drooping solvent volume fraction profile). This fact can also be realized by the values of the mutual diffusion coefficient D_0 and self-diffusion coefficient of the solvent at saturation D_{eq}. Previous experimental and numerical studies, on other polymer systems, report the two diffusion coefficients are at least 4-5 orders of magnitude apart owing to the slow viscoelastic relaxation process.[139,178,179]

Finally, I quantitatively validate the model by comparing the experimental data with numerical results. In these simulations I use average values of mutual diffusion coefficient of $D_0 = 2 \times 10^{-11}$ m^2s^{-1}, shear modulus of $G_0 = 24$ kPa, and interaction parameter $\chi = 0.55$. I do, however, account for the experimental variations in the sample dimensions by simulating the range of $d = 3.9 \pm 0.1$ mm and $L = 28 \pm 1$ mm. As shown in Figure 4.4, the model predictions agree well with the experimental results considering the possible uncertainties in the experiments. Specifically, the plot in Figure 4.4a shows the variation in NBPA-33 cylinder outer diameter and the location of the solvent front with time (in terms of the radius of dry core polymer $d_i/2$). The increase in the outer radius follows a power-law-like trend similar to the solvent uptake in Figure 4.1a. In fact, the increase in diameter with time can be expressed in terms of power exponent n. It can easily be shown that the cylindrical samples maintain the aspect ratio when swollen. I use this characteristic to derive the expression for cylinder diameter as follows:

$$R = R_d\left[1+\frac{(J_{eq}-1)}{\zeta}kt^n\right]^{1/3} \tag{4.17}$$

Where, R_d is the radius of the dry polymer sample and ζ is the density ratio of solvent and the dry polymer. The increase in radius predicted by equation 4.17 is also plotted in Figure 4.4b. Thus, by performing gravimetry experiments, one can find the swelling stretch along the radial and axial directions.

For the solvent front propagation as well, we can see a similar trend. As noted earlier, the solvent front does not propagate at constant velocity, but it slows down as it moves towards the center of the cylinder. This happens because the diffusion in the swollen part of the polymers eventually becomes slower than the diffusion in the dry polymer due to the reduced chemical potential gradient in the swollen matrix.

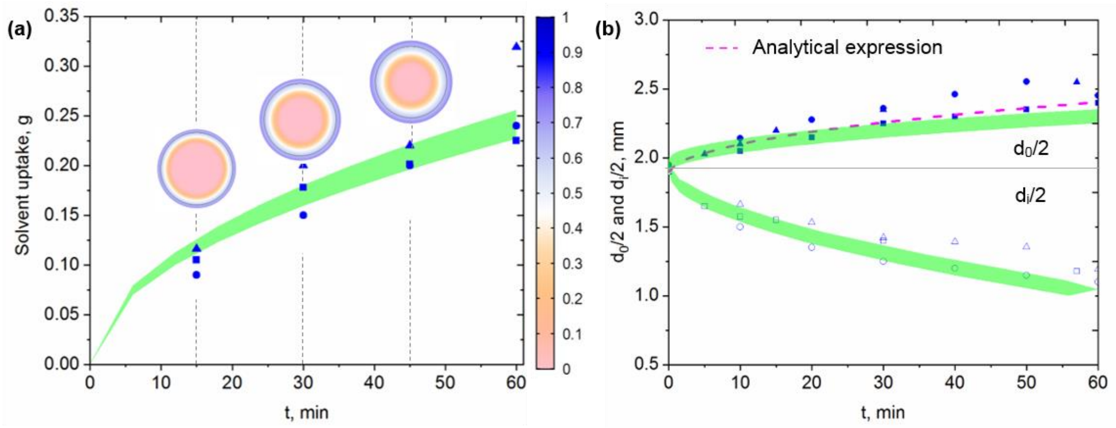

Figure 4.4 (a) Comparison between solvent uptake by polymer as measured from three experiments (in blue markers) and numerical predictions (green band) accounting for variation in diameter and length of the samples (legend: solvent volume fraction), (b) Comparison between radial deformation of the sample from optical imaging experiments and predictions from the numerical model.

Lastly, note that we compared numerical and experimental results over the span of 1 hour due to experimental limitations. Specifically, I observed that past 1 hour, as the dry polymer core becomes small, it cracks and ruptures resulting in local variations in solvent flux. Thomas and Windle[180] attributed this type of fracture to the compressive forces exerted by the swollen polymer surrounding the relatively thin dry polymer. In addition, the polymer samples we synthesized contained a small fraction of an uncrosslinked polymer which eventually dissolves in the solvent. I measured this amount by weighing the mass before and after swelling and found it to be about 10% thus suggesting lower molecular weight of the polymer. Capturing these two effects in the numerical model is beyond the scope of the current work and thus, we restrict the validation effort to the first hour of the transient behavior. Moreover, for most applications of SAPs, such as chemical containment, soft robotics, drug delivery, etc., the sample size we considered (~ 10^0 mm) is towards the higher end. For smaller sample sizes the swelling time scale will be much shorter and the amount of uncrosslinked polymer and swelling compressive stress will reduced, proportionately, making the model more appropriate in such scenarios.

4.6 Materials and Methods

4.6.1 Synthesis of NBPA-33

The super absorbent polymer developed for this work is obtained by polymerizing N-butyl-N-Phenyl Acrylamide incorporating Poly(ethylene glycol) 200 dimethacrylate (PEGDMA 200, Polysciences) as a crosslinker. Details of the synthesis of NBPA-33 are provided in our previous work.[147] Briefly, the polymerization procedure is as follows. I mix N-butyl-N-Phenyl Acrylamide with Azobisisobutyronitrile (Millipore Sigma, 0.8 mol% based on monomer) and add PEGDMA 200 (0.5 mol% based on monomer). I then seal the mixture in a glass bottle and perform a freeze-pump-thaw cycling 3-4 times in nitrogen environment to remove dissolved oxygen. Finally, I cast the polymer solution in the required shape using a suitable mold and cure it at 50 °C for 20-24 hours in nitrogen purged environment.

4.7 Conclusions

In this work, I characterize recently developed low molecular weight NBPA-33, a superabsorbent polymer tuned to selectively absorb target solvents, and develop a predictive numerical model of its swelling dynamics in o-xylene. I identify the pseudo-Fickian diffusion of *o*-xylene in this polymer via solvent uptake and optical imaging experiments. To define the variable macroscopic diffusion coefficient for diffusion in NBPA-33, I suggest a new methodology based on a combination of Poroelastic Relaxation Indentation and gravimetry. Using this simple method, I show that the diffusion in NBPA-33 can be reasonably well characterized. Using parameters measured using this method, I develop a finite element-based model of the NBPA-33 swelling behavior. The solvent absorption and swelling deformation predicted by the model agrees well with the experimental data. In a two-fold future work, the polymer synthesis process can be further streamlined to have higher molecular weight NBPA and the non-fickian part of the solvent flux may be incorporated in the model via stress-diffusion coupling for more accuracy. In fact, through the PRI test, the viscoelastic parameters of the polymer can also be measured and incorporated into the model. This overall simplifying computational framework can provide important insights in designing complex applications based on NBPA-33 such as bio-mimicking semi-permeable barriers, chemical containment fabrics and membranes.

5 BREATHABLE, SELF-SEALING MEMBRANE FOR HAZMAT SUIT APPLICATIONS

In this chapter, I present the design, development and characterization of a composite breathable fabric that self-seals upon exposure with CWA simulant aerosol. The chapter is broadly divided into two sections- the preceding text concerns with design parameters of the fabric where I describe how the previous work on polymer synthesis, characterization and the numerical model discussed in chapters 3 and 4 culminates into determining these parameters. The subsequent text describes the development of the polymer and fabric design.

5.1 Composite fabric design considerations

So far, in chapters 3 and 4 we investigated the swelling response of the polymer and the effect of its geometrical and chemo-mechanical properties with a given penetrant. Using multiphysics finite element modeling, we gained insights into underlying mechanisms that correlate these parameters with the swelling behavior. However, to design the fabric, we need to consider the external parameters as well that are critical to its functioning. So, in the first section of this chapter, I combine the understanding of effect of the geometric and transport properties on swelling with the previously unexplored factors such as CWA droplet aerosol size distribution, droplet ‘encounter’ frequency, base fabric mesh size etc. In the following text, I explore the parametric space for these factors and discuss how these design considerations can be utilized to optimize the design.

5.1.1 CWA aerosol droplet size distribution

Most target CWAs that are of concern in this work are low vapor pressure liquids. The aerosol spray of these chemicals can linger in the air for prolonged durations and gets transported via wind and atmospheric diffusion. Characterizing CWA aerosol is extremely difficult and can only be done in specialized laboratories. Not surprisingly, there have been only a few reports about the CWA aerosol droplet size distribution (ADSD), related to the development of reliable methodologies for CWA detection. The most relevant study to our interest was done where using a combination of FTIR and flow-through photoacoustic methods, Gurton *et al.*[181] characterized the aerosol of four CWA simulants- DMMP and DEMP (both simulants of sarin), DIMP (simulant of Soman) and DEP (simulant for VX). The authors measured the droplets produced by the compressed air-based nebulizer with median diameter between 1-2 µm and used it to test a proposed optical characterization methodology. In other reports, techniques like ion mobility mass spectrometry,[182] single-particle aerosol mass spectrometry,[183] were demonstrated for the detection of CWA simulant aerosol with droplet size between 1-5 µm. Basing the further analysis on these reports, I consider the target aerosol with droplet size distribution between 1-5 µm.

5.1.2 SAP form and synthesis

The composite fabric has been proposed to use standard military clothing materials such as cotton or nylon as the base fabric. Thus, I consider cylindrical and spherical geometries for the SAP since they are easy to integrate with fibers of these materials. The cylindrical geometry can be achieved by dip-coating the base material fiber so that it conforms to the typical fabric structure. However, a continuous matrix of the polymer would provide additional material for solvent diffusion resulting in spreading of the chemical.

To test this hypothesis, I conducted a preliminary ‘proof-of-concept’ experiment. I coated the nylon fishing line (2 mm diameter) with Sylgard 184 (Dow Corning) using a custom-build die-cast setup. A few drops of hexane were placed in the gap between two such PDMS coated fibers placed 0.4 mm from each other and I recorded the gap using an optical camera. The PDMS coating swells by rapidly absorbing the hexane and the gap between the fibers is closed as a result.

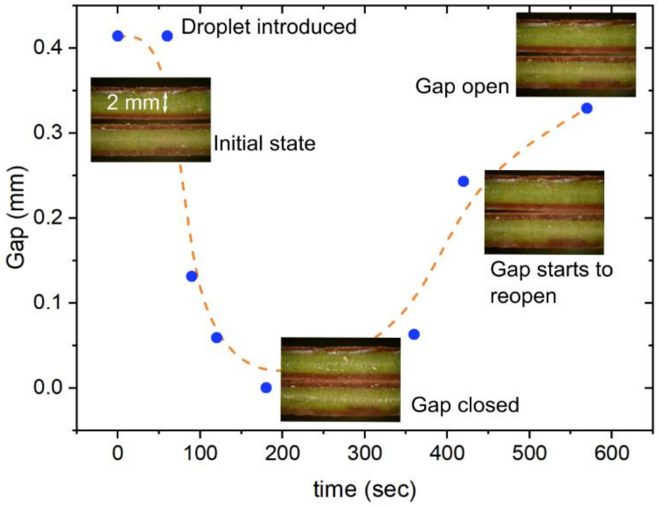

Figure 5.1 Time response of the gap between two parallel PDMS coated fibers after introducing hexane droplet(s) in the gap.

However, due to the continuous matrix of polymer available for diffusion, the absorbed hexane spreads throughout the coating and redistributing and reducing the local concentration. As hexane diffuses, the polymer coating responds by ‘de-swelling’ and the gap opens again. This is evident from Figure 5.1 where I plot the gap between the fibers with time of experiment. After the droplet is placed, the gap closes rapidly to 10% in 100 seconds however, as the hexane redistributes, the local swelling reduces, and the gap opens again in 400 seconds to 90% of its nominal value. Note that the hexane distribution occurs primarily along the circumferential direction and then along the length of the fiber due to diffusion timescale associated with these dimensions.

This observation has important implications on the geometrical considerations of the polymer. Although the conformal coating lets the solvent distribute itself, it could very well be effective over prolonged exposure periods with continuous droplet encounter. However, for intermittent exposures, this design will render ineffective since it may remain open for significant periods. Since hazmat suits are not recommended for prolonged use in presence of high concentration areas, effective protection against low encounter rate is more desirable here. Additionally, to conformally coat the fibers, large amounts of SAP is required which can make the system costly and increase its weight.

This situation can be avoided by designing a discontinuous matrix of the SAP localized to the fabric pores. The most convenient geometry is spherical, which is easier to make as compared to the conformal coating and is also easy to integrate with the base fabric. Ideally, spherical beads of NBPA can be attached to the base fabric on corners of the pore such that the when the CWA droplet comes in contact, it has higher probability of getting trapped. Next, I discuss the rationale behind determining the size of the NBPA beads. In chapter 3, I showed that the extent of polymer swelling is maximized when the polymer and droplet dimensions are comparable using a spatiotemporal scaling analysis (case iii in Figure 3.3). This result is used as a principal guideline to determine the dimensions of the NBPA in the fabric. In the previous section, I reported the literature values for CWA ADSD which I reproduced using a custom-built ultrasonic nebulizer setup. Evidently, the SAP geometry needs to have the size comparable to these droplets. Thus, the target geometrical size of the polymer is fixed at ~10^0 µm. Please note that this constraint is applicable only to the relevant dimension, *i.e.* the dimension responsible for closing of the pores during swelling.

These beads can be synthesized are synthesized using emulsion polymerization method in which the monomer N-butyl-N-phenylacrylamide is crosslinked using 1,10-decanedioldimethacrylate. This crosslinker has been chosen due to its hydrophobicity which makes it easier to form an oil in water type of emulsion for the polymer solution. Next, Sodium decyl sulphonate (SDS) is added as a surfactant which helps in controlling the size of the beads. The crosslinking reaction is photo-initiated through Irgacure I2959 which is dissolved in the water. This allows crosslinking to begin at the surface of the bead uniformly, penetrating inwards. The solution is finally cured under a UV light source (365 nm, 20 mW/cm^2) while kept on a vortex mixer to maintain high shear rate in the suspension for 10 min. The solution was then allowed to separate and excess water was removed which also removes dissolved SDS. Then, small amount of IPA was added to remove any uncrosslinked polymer. This procedure was repeated a couple of times and solution was allowed to dry at the room temperature to get the dry polymer powder (It is to be noted that this procedure has been developed by a co-contributor solely and is reproduced here with a permission).

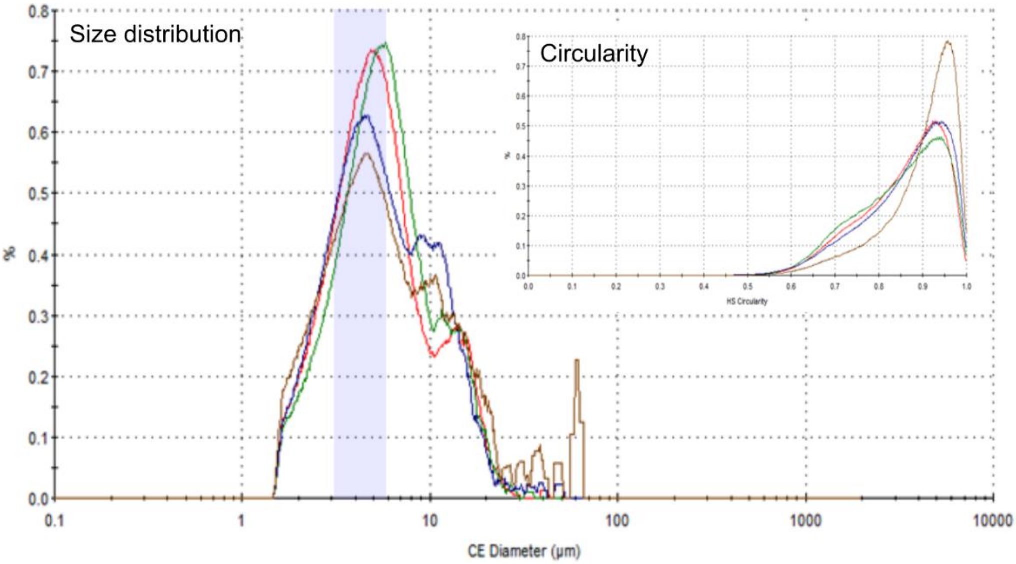

Figure 5.2 The size distribution of NBPA beads obtained through emulsion polymerization. Insert: Circularity of the particles. Both size distribution and circularity are measured using Malvern morphologi particle analyzer.

Finally, to check the results of the emulsion polymerization, I characterized the NBPA powder using a particle analyzer (Malvern Morphologi). The results are shown in Figure 5.2 which shows number averaged bead diameter ~ 2.8 µm and circularity between 0.9-1.0. The NBPA bead size obtained using given amounts of materials is adequate to our design as I discuss later. However, any changes in the size can be obtained by changing the amount of SDS in the allowable range (typically up to ~10^1 µm).

5.2 Composite fabric design

Once the size of polymer beads was roughly decided, I used COMSOL model simulations to determine the design guidelines for the base fabric. From the gravimetry experiments, the equilibrium swelling ratio of the SAP was measured to be between 5-6. That means the equilibrium stretching ratio experienced by the SAP beads is approximately $\sqrt[3]{5.5} \cong 1.8$. Thus, based on SAP bead size we can roughly estimate a maximum dimension of the fabric pore that can be closed by SAP swelling. However, realistically, multiple SAP beads can be 'triggered' when CWA droplet is encountered and close the pore as they swell. In this process, the beads will likely come in contact with each other. This contact dynamics thus can have an effect on how the pore is closed. I developed a COMSOL model to simulate this process. This model incorporates the effect of SAP beads touching each other using inbuilt COMSOL functionality to define contact pairs for deforming geometries.

I simulate the 2-D model to estimate: 1. size of the pore that can be closed upon swelling of beads of a given size, 2. time required by the beads to swell and close the area. Note that I refer to the closing of pore when at least 95% of the initial pore area is closed. This estimate is reasonable since the CWA droplet size distribution indicates that no droplet will pass through the 5% of the pore area. Also, closing of the area is asymptotic with time after 95% area is closed as neighboring beads experience 'locking' effect, rendering any further attempts to close the pore, inefficient.

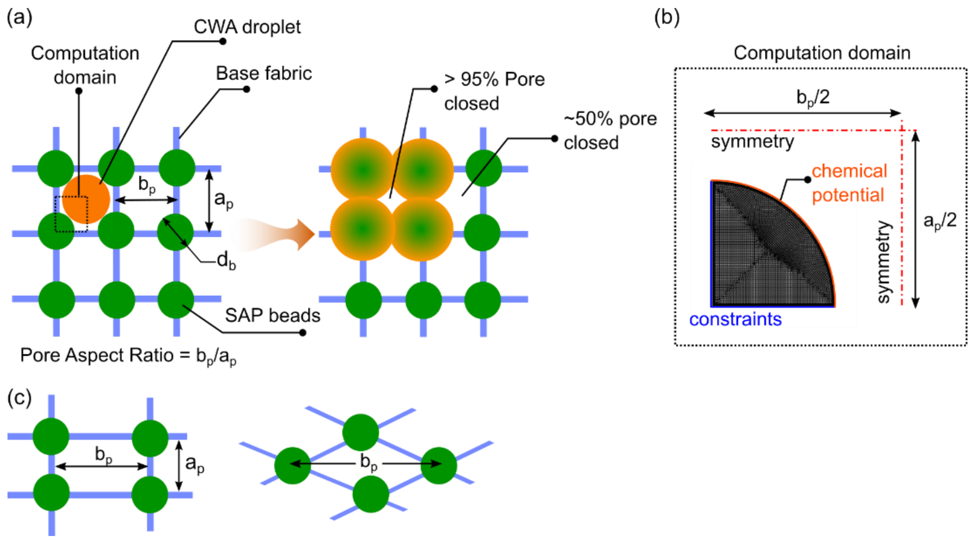

Figure 5.3 (a) 2-D schematic of composite fabric with discontinuous SAP matrix beads attached to the porous mesh. After CWA contact, the beads swell and close the pore. (b) Computation domain in COMSOL used to simulate the closing of pores in base mesh and study the effect of variation in parameters $a_p/2$ and $b_p/2$.

First, I consider a highly ordered mesh with square pores of size $a_p(= b_p)$. Assuming ideal design, I consider four SAP beads of diameter d_b attached around the square, one at each corner such that $a_p{\sim}d_b$. To simplify the simulation, I consider only one pore with four beads on the four corners as shown in Figure 5.3 and simulate only a quarter of the domain as shown to reduce the computation time. For a given size of SAP bead (d_b), I considered different values of a_p and b_p. The results from these numerical tests are summarized in Figure 5.4 Results from the 2-D model showing pore closing dynamics for a square arrangement. Inset: Effect of pore aspect ratio on the relationship between pore size and SAP bead size for effective protection. Please note that the 2-D representation of the sphere extends to cylindrical geometries in 3-D space. However, this assumption does not affect my results regarding swelling along the radial direction. I observed that, in agreement with my initial estimate, to close the pore at least 95% of its initial size, the size of the square pore cannot be more than $1.8d_b$ and ideally it should be $1.75d_b$. As it can be seen from the plot in Figure 5.4 with the increase in gap beyond $2d_b$, the pore remains at least 20% open which is an undesirable scenario. Thus, from the COMSOL model we use this relationship between pore size and SAP bead as the design guideline in selecting the base fabric. Also note that the pore size can be smaller than $1.75d_b$ but the design would be not as effective since the swellability of SAP beads will not be fully utilized in such designs. It is important to note the time required for the closing of the pore as well.

To close the pore by 95% of its initial area, it takes approximately 0.2-0.5 s. Comparing this with the diffusion time scale I get, $\tau_d \sim \frac{D_b^2}{D_0} \sim 1\ s$ (for $D_b = 2\ \mu m$) which is comparable to my simulation results, where $D_0 = 2 \times 10^{-11}$ m^2s^{-1} is the mutual diffusion coefficient measured in chapter 4. This means that this design can provide protection against CWA droplet ‘encounter frequency’ as high as 2-5 s^{-1} with no limit on the lower bound of the frequency.

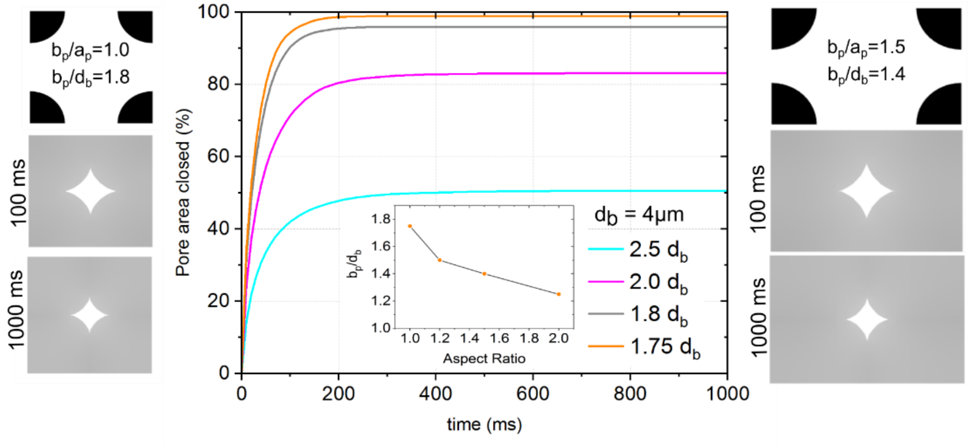

Figure 5.4 Results from the 2-D model showing pore closing dynamics for a square arrangement. Inset: Effect of pore aspect ratio on the relationship between pore size and SAP bead size for effective protection.

In other words, this design is applicable in both high and low CWA concentration regions. However, due to discontinuity, the beads are likely to saturate at much faster rate than conformal configuration. To examine the saturation condition, I calculate the number of droplets the SAP bead can absorb before it saturates as $n_{sat} = (J_{eq} - 1)\left(\frac{d_b}{d_{cwa}}\right)^3$, where d_{cwa} is diameter of the CWA droplet. Thus, based on the nominal values of $d_b = 2\ \mu m, d_{cwa} = 1\ \mu m$ and $J_{eq} = 5.5$, we can estimate that each bead can absorb approximately 40 droplets. This gives us the total time of ~10-20 s at maximum allowable droplet encounter frequency. However, as noted earlier, these hazmat suits are not recommended in ‘high-concentration’ areas, thus we expect the fabric to self-sealing for much longer durations in medium-low impact areas. It should be noted that estimating the realistic droplet encounter rates is an extremely difficult task and is not available to the best of the author's knowledge. Thus, investigating the effectiveness of the composite fabric in these scenarios is beyond the scope of this work.

Once the ideal square pore is simulated, I consider rectangular and diamond-shaped pores as well since they are encountered frequently in fabric meshes. It can be seen from Figure 5.4 that we can still define these shapes in terms of the variables b_p and a_p where b_p always denotes the larger dimension irrespective of the geometry. It can be shown that the dimensional requirements for a diamond-shaped pore can be deduced from square or rectangular pores.

6 CONCLUSIONS AND FUTURE WORK

Interactions between functional polymers and droplets show interesting multiphysics behavior. These interactions are studied in detail in the context of dropwise condensation and swelling-based breathable protective fabric. During dropwise condensation, small droplets deform the soft substrate through elastocapillary interactions. I show that these deformations alter the heat transfer and thus, can have profound effects in optimizing the mechanical properties of the substrate. In swelling-based breathable protective fabric, I studied the swelling in specialized polymer caused by droplets of chemical weapon agent simulants. Through combined experimental and numerical approach, I showed that this interaction can be exploited in developing an adaptive fabric that responds to these simulants and becomes nonpermeable locally in both time and space.

With advent of research in soft, conductive composite polymer, desired thermal properties can be achieved for various thermal management applications. However, in case of phase change applications, mechanical properties play an important role and thus these materials need to be carefully examined. Through my analytical-experimental analysis, I showed that softer substrates lower the condensation heat transfer on account of ramifications of their mechanical properties. However, in this analysis, I used the droplet size distribution developed for the metal surfaces. I see some opportunity to further extend my analysis by using more appropriate droplet size distribution on soft elastomeric materials. However, I expect this to marginally change my results only quantitively while the qualitative conclusion will still hold good.

In addition, I showed that softer surface increases the resistance to droplet shedding in which droplets slide off a vertical surface under gravity. This detrimental effect can be avoided if a surface can be thought of as a metamaterial capable of changing its elastic modulus throughout the course of the droplet ‘life-cycle’. With that, droplet nucleation and shedding being a cyclic phenomenon, the frequency of mechanical tuning of the surface can be ‘synced’ with it to have soft surface during nucleation while becoming harder as the droplet grows. Numerical simulation of these interactions could be fairly evolved but can be implemented to see the effects on the overall heat transfer. However, given the fact that the deformation of the surface due to small droplets has maximum effect on the heat transfer, I expect the frequency-based modulation of the mechanical properties to only compensate for it and not improve it further with respect to the baseline.

Chemically induced swelling of polymers has long been studied and used in numerous applications. When controlled locally, swelling can be used to induce interesting modulations in topology. Through finite element modeling of this multiphysics behavior, I explored these modulations of elastomeric material geometries caused by chemical droplets. Through geometric and temporal scaling laws, I showed that there exists a relation between droplet size and polymer size which results into different topologies for different relationships. I validated this hypothesis by testing two such geometrical relationships qualitatively and used the quantitative measurement to validate the numerical model.

In chapter 4, I extended this modeling to superabsorbent polymer which swells in much larger proportions as compared to the elastomers. I characterized this customized polymer to measure its mechanical and chemical properties while suggesting a simpler method based on Poroelastic relaxation indentation. This allowed me to extract all relevant properties required for predictive modeling from two simple tests. Subsequently, I showed that the swelling nature on account of its spatial deformations, can be used to actively control the dimensionalities of the system in stimulus environments. This allowed me to explore the droplet induced swelling of superabsorbent polymers for designing a breathable protective fabric in which beads of polymer close the open pores in the fabric when contaminated by harmful chemical agents. This toggle action of closing of pore is local to the area of contamination thus keeping the fabric breathable which can solve the thermoregulation problem in current systems.

Using insights from my finite element modeling about absorption, diffusion, and deformation processes, I developed design guidelines for developing such fabric. In developing these guidelines, I used both, geometric relationships between droplets and elastomers and predictive modeling of superabsorbent polymer; and extended to incorporate the external factors such as CWA droplet size distribution, base fabric etc. In continuation of this work, I suggest exploring the decontamination mechanisms through which absorbed chemicals can be cleaned-of off the polymer the matrix ‘refreshing’ the polymer for cyclic operations. Primary suggestion includes using an adsorbing material with high surface to volume ration situated inside the polymer matrix. This will allow the chemical to move away from the polymer matrix while ‘drying’ it which makes it available to swell again and block the CWA droplets when required. This recommendation increases the overall life span of the hazmat suite till the adsorption mechanism is completely saturated.

REFERENCES

1 P. Kotagama, A. Phadnis, K. C. Manning and K. Rykaczewski, *Adv. Mater. Technol.*, 2019, 1800690, 1–12.

2 S. A. Nunneley, *Space Life Sci.*, 1970, **2**, 335–360.

3 M. D. Bartlett, N. Kazem, M. J. Powell-Palm, X. Huang, W. Sun, J. A. Malen and C. Majidi, *Proc. Natl. Acad. Sci.*, 2017, 201616377.

4 M. I. Ralphs, N. Kemme, P. B. Vartak, E. Joseph, S. Tipnis, S. Turnage, K. N. Solanki, R. Y. Wang and K. Rykaczewski, *ACS Appl. Mater. Interfaces*, 2017.

6 S. H. Jeong, S. Chen, J. Huo, E. K. Gamstedt, J. Liu, S.-L. Zhang, Z.-B. Zhang, K. Hjort and Z. Wu, *Sci. Rep.*, 2015, **5**, 18257.

7 V. G. Damle, X. Sun and K. Rykaczewski, *Adv. Mater. Interfaces*, 2015, **2**, 1400479.

8 M. Sokuler, G. K. Auernhammer, M. Roth, C. Liu, E. Bonacurrso and H. J. Butt, *Langmuir*, 2010, **26**, 1544–1547.

9 S. Anand, A. T. Paxson, R. Dhiman, J. D. Smith and K. K. Varanasi, *ACS Nano*, 2012, **6**, 10122–10129.

10 A. M. Cazabat, *Contemp. Phys.*, 1987, **28**, 347–364.

11 V. M. Starov, S. R. Kostvintsev, V. D. Sobolev, M. G. Velarde, S. A. Zhdanov and M. G. Velarde, *Langmuir*, 2002, **18**, 9744–9750.

12 M. J. de Ruijter, J. de Coninck and G. Oshanin, *Langmuir*, 1999, **15**, 2209–2216.

13 T. C. Hung, *Energy*, 1997, **22**, 7, 661-667.

14 W. F. Castle, *Int. J. Refrig.*, 2002, **25**, 158–172.

15 A. T. Paxson, J. L. Yagüe, K. K. Gleason and K. K. Varanasi, *Adv. Mater.*, 2014, **26**, 418–423.

16 V. P. Carey, *Liquid–vapor phase-change phenomena: An introduction to the thermophysics of vaporization and condensation process in heat transfer equipment*, Bristol, 2nd edn., 2007.

17 R. L. Webb and N.-H. Kim, *Taylor Fr. New York, NY, USA*, 2007.

18 J. W. Rose, *Proc. Inst. Mech. Eng. Part A J. Power Energy*, 2005, **216**, 115–128.

19 M. H. Rausch, A. P. Fröba and A. Leipertz*, Int. J. Heat Mass Transf.*, 2008, **51**, 1061–1070.

20 G. Azimi, R. Dhiman, H.-M. Kwon, A. T. Paxson and K. K. Varanasi, *Nat. Mater.*, 2013, **12**, 315–320.

21 D. J. Preston, D. L. Mafra, N. Miljkovic, J. Kong and E. N. Wang, *Nano Lett.*, 2015, **15**, 2902–2909.

22 R. Xiao, N. Miljkovic, R. Enright and E. N. Wang, *Sci. Rep.*, 2013, **3**, 1988.

23 S. Anand, K. Rykaczewski, S. B. Subramanyam, D. Beysens and K. K. Varanasi, *Soft Matter*, 2014, **11**, 69–80.

24 C. Lixin and Y. Jiehui, *J. Enhanc. Heat Transf.*, 1998, **5**, 1–8.

25 S. Vemuri, K. J. Kim, B. D. Wood, S. Govindaraju and T. W. Bell, *Appl. Therm. Eng.*, 2006, **26**, 421–429.

26 K. K. Varanasi, M. Hsu, N. Bhate, W. Yang and T. Deng, *Appl. Phys. Lett.*, 2009, **95**, 094101.

27 P. S. Mahapatra, A. Ghosh, R. Ganguly and C. M. Megaridis, *Int. J. Heat Mass Transf.*, 2016, **92**, 877–883.

28 L. Mishchenko, M. Khan, J. Aizenberg and B. D. Hatton, *Adv. Funct. Mater.*, 2013, **23**, 4577–4584.

29 B. Mondal, M. Mac Giolla Eain, Q. Xu, V. M. Egan, J. Punch and A. M. Lyons, *ACS Appl. Mater. Interfaces*, 2015, **7**, 23575–23588.

30 C. W. Yao, T. P. Garvin, J. L. Alvarado, A. M. Jacobi, B. G. Jones and C. P. Marsh, *Appl. Phys. Lett.*, 2012, **101**, 111605.

31 D. M. Anderson, M. K. Gupta, A. A. Voevodin, C. N. Hunter, S. A. Putnam, V. V Tsukruk and A. G. Fedorov, *ACS Nano*, 2012, **6**, 3262–3268.

32 X. Chen, R. Ma, H. Zhou, X. Zhou, L. Che, S. Yao and Z. Wang, *Sci. Rep.*

33 A. Ghosh, S. Beaini, B. J. Zhang, R. Ganguly and C. M. Megaridis, *Langmuir*, 2014, **30**, 13103–13115.

34 V. G. Damle and K. Rykaczewski, *Appl. Phys. Lett.*, 2017, **110**, 171603.

35 J. B. Boreyko and C.-H. Chen, *Phys. Rev. Lett.*, 2009, **103**, 184501.

36 C. Dietz, K. Rykaczewski, A. G. Fedorov and Y. Joshi, *Appl. Phys. Lett.*, 2010, **97**, 33103–33104.

37 N. Miljkovic, R. Enright and E. N. Wang, *Am. Chem. Soc.*, 2012, **6**, 1776–1785.

38 N. Miljkovic and E. N. Wang, *MRS Bull.*, 2013, **38**, 397–406.

39 N. Miljkovic, R. Enright, Y. Nam, K. Lopez, N. Dou, J. Sack and E. N. Wang, *Nano Lett.*, 2013, **13**, 179–187.

40 K. Rykaczewski, A. T. Paxson, S. Anand, X. Chen, Z. Wang and K. K. Varanasi, *Langmuir*, 2013, **29**, 881–891.

41 P. B. Weisensee, Y. Wang, Q. Hongliang, D. Schultz, W. P. King and N. Miljkovic, *Int. J. Heat Mass Transf.*, 2017, **109**, 187–199.

42 M. Coux, C. Clanet and D. Quéré, *Cit. Appl. Phys. Lett*, 2017, **110**, 251605.

43 T. Vasileiou, T. M. Schutzius and D. Poulikakos, *Langmuir*, 2017, **33**, 6708–6718.

44 P. B. Weisensee, J. Tian, N. Miljkovic and W. P. King, *J. Heat Transfer*, 2017, **139**, 20902.

45 S. Gart, J. E. Mates, C. M. Megaridis and S. Jung, *Phys. Rev. Appl.*, 2015, **3**, 44019.

46 R. E. Pepper, L. Courbin and H. A. Stone, *Phys. Fluids*, 2008, **20**, 82103.

47 S. Mangili, C. Antonini, M. Marengo and A. Amirfazli, *Soft Matter*, 2012, **8**, 10045–10054.

48 R. Rioboo, M. Voué, H. Adão, J. Conti, A. Vaillant, D. Seveno and J. De Coninck, *Langmuir*, 2009, **26**, 4873–4879.

49 P. B. Weisensee, J. Tian, N. Miljkovic and W. P. King, *Sci. Rep.*, 2016, **6**, 30328.

50 R. W. Style, C. Hyland, R. Boltyanskiy, J. S. Wettlaufer and E. R. Dufresne, *Nat. Com*, 2013, 2728.

51 B. Andreotti, O. Bäumchen, F. Boulogne, K. E. Daniels, E. R. Dufresne, H. Perrin, T. Salez, J. H. Snoeijer and R. W. Style, *Soft Matter*, 2016, **12**, 2993–2996.

52 X. Yao, Y. Hu, A. Grinthal, T.-S. Wong, L. Mahadevan and J. Aizenberg, *Nat. Mater.*, 2013, **12**, 529–534.

53 W.-K. Lee, W.-B. Jung, S. R. Nagel and T. W. Odom, *Nano Lett.*, 2016, **16**, 3774–3779.

54 A. Carré and M. E. R. Shanahan, *Langmuir*, 2001, **17**, 2982–2985.

55 A. Carré and M. E. R. Shanahan, *Am. Chem. Soc. Polym. Prepr. Div. Polym. Chem.*, 1996, **37**, 72–73.

56 Y. Wang, B. Qian, C. Lai, X. Wang, K. Ma, Y. Guo, X. Zhu, B. Fei and J. H. Xin, , *ACS Appl. Mater. Interfaces*, 2017, 9,29, 24428-24432.

57 S. Karpitschka, S. Das, M. Van Gorcum, H. Perrin, B. Andreotti and J. H. Snoeijer, *Nat. Commun.*, 2014, **6**, 1–7.

58 S. J. Park, B. M. Weon, J. S. Lee, J. Lee, J. Kim and J. H. Je, *Nat. Commun.*, 2014, **5**, 1–7.

59 L. Chen, G. K. Auernhammer and E. Bonaccurso, *Soft Matter*, 2011, **7**, 9084.

60 R. W. Style, A. Jagota, C.-Y. Hui and E. R. Dufresne, *Annu. Rev. Condens. Matter Phys.*, 2017, **8**, 99–118.

61 R. W. Style and E. R. Dufresne, *Soft Matter*, 2012, **8**, 7177–7184.

62 M. Abu-Orabi, *Int. J. Heat Mass Transf.*, 1998, **41**, 81–87.

63 S. Chavan, H. Cha, D. Orejon, K. Nawaz, N. Singla, Y. F. Yeung, D. Park, D. H. Kang, Y. Chang, Y. Takata and N. Miljkovic, *Langmuir*, 2016, **32**, 7774–7787.

64 A. I. Rusanov, *J. Colloid Interface Sci.*, 1978, **63**, 330–345.

65 Y.-S. S. Yu and Y.-P. P. Zhao, *J. Colloid Interface Sci.*, 2009, **339**, 489–494.

66 R. Pericet-Cámara, A. Best, H. J. Butt and E. Bonaccurso, *Langmuir*, 2008, **24**, 10565–10568.

67 R. Pericet-Camara, G. K. Auernhammer, K. Koynov, S. Lorenzoni, R. Raiteri and E. Bonaccurso, *Soft Matter*, 2009, **5**, 3611.

68 X. Sun and K. Rykaczewski, *ACS Nano*, 2016, **11**, 906–917.

69 J. Chen and S. J. Bull, *Vacuum*, 2009, **83**, 911–920.

70 A. S. Alaboodi and Z. Hussain, *J. King Saud Univ. - Eng. Sci.*, 2019, 31, 1, 61-69.

71 R. W. Style, C. Hyland, R. Boltyanskiy, J. S. Wettlaufer and E. R. Dufresne, *Nat. Commun.*, 2013, **4**, 2728.

72 F. Eslami and J. A. W. Elliott, *J. Phys. Chem. B*, 2011, **115**, 10646–10653.

73 A. Phadnis and K. Rykaczewski, *Int. J. Heat Mass Transf.*, 2017, **115**, 148–158.

74 S. Karpitschka, A. Pandey, L. A. Lubbers, J. H. Weijs, L. Botto, S. Das, B. Andreotti and J. H. Snoeijer, *Proc. Natl. Acad. Sci.*, 2016, **113**, 7403–7407.

75 A. Pandey, S. Karpitschka, L. A. Lubbers, J. H. Weijs, L. Botto, S. Das, B. Andreotti and J. H. Snoeijer, *Soft Matter*, 2017, **13**, 6000–6010.

76 A. Phadnis and K. Rykaczewski, *Langmuir*, 2017, **33**, 12095–12101.

77 T. L. Bergman, A. S. Lavine, F. P. Incropera and D. P. Dewitt, 2007, *Fundamentals of heat and mass transfer*, Wiley.

78 J. Guadarrama-Cetina, R. D. Narhe, D. A. Beysens and W. González-Viñas, *Phys. Rev. E - Stat. Nonlinear, Soft Matter Phys.*, 2014, **89**, 1–10.

79 J. W. Rose, *Chem. Eng. Res. Des.*, 2004, **82**, 419–429.

80 Y. Utaka and S. Wang, *Int. J. Heat Mass Transf.*, 2004, **47**, 4507–4516.

81 T. Murase, H. S. Wang and J. W. Rose, *Int. J. Heat Mass Transf.*, 2007, **50**, 3774–3779.

82 Y. Yamada, T. Ikuta, T. Nishiyama, K. Takahashi and Y. Takata, *Langmuir*, 2014, **30**, 14532–14537.

83 A. Phadnis and K. Rykaczewski, *Int. J. Heat Mass Transf.*, 2017, **115**, 148–158.

84 K. Rykaczewski, A. T. Paxson, M. Staymates, M. L. Walker, X. Sun, S. Anand, S. Srinivasan, G. H. Mckinley, J. Chinn, J. H. J. Scott and K. K. Varanasi, *Sci. Rep.*, 2014, **4**, 4158.

85 M. E. Cabrera, G. M. Saidel, S. C. Kalhan, A. J. Physiol and H. Circ, *Society*, 2008, **82**, 1522–1536.

86 W. Hong, X. Zhao, J. Zhou and Z. Suo, *J. Mech. Phys. Solids*, 2008, **56**, 1779–1793.

87 D. J. Buckley, M. Berger and D. Poller, *J. Polym. Sci.*, 1962, **56**, 163–174.

88 M. Doi, *J. Phys. Soc. Japan*, 2009, **78**, 052001.

89 D. J. Tanaka, T. & Fillmore, *J.Chem. Phys.*, 1979, **70**, 1214.

90 M. Daoud, E. Bouchaud and G. Jannink, *Macromolecules*, 1986, **19**, 1955–1960.

91 E. Reyssat and L. Mahadevan, *J. R. Soc. Interface*, 2009, **6**, 951-957.

92 B. P. N. Singh and S. P. Kulshrestha, *J. Food Sci.*, 1987, **52**, 1538–1541.

93 M. J. Harrington, K. Razghandi, F. Ditsch, L. Guiducci, M. Rueggeberg, J. W. C. Dunlop, P. Fratzl, C. Neinhuis and I. Burgert, *Nat. Commun.*, 2011, **2**, 337.

94 P. Fratzl and F. G. Barth, *Nature*, 2009, **462**, 442–448.

95 Y. Qiu and K. Park, *Adv. Drug Deliv. Rev.*, 2001, **53**, 321–39.

96 D. T. Eddington and D. J. Beebe, *Adv. Drug Deliv. Rev.*, 2004, **56**, 199–210.

97 S. Ahn, R. M. Kasi, S.-C. Kim, N. Sharma and Y. Zhou, *Soft Matter*, 2008, **4**, 1151.

98 Z. Liu and P. Calvert, *Adv. Mater.*, 2000, **12**, 288–291.

99 T. Ono, T. Sugimoto, S. Shinkai and K. Sada, *Nat. Mater.*, 2007, **6**, 429–433.

100 J.-B. Fan, Y. Song, S. Wang, J. Meng, G. Yang, X. Guo, L. Feng and L. Jiang, *Adv. Funct. Mater.*, 2015, **25**, 5368–5375.

101 W. A. Akber Hassan and X. Jiang, *Greenh. Gases Sci. Technol.*, 2012, **2**, 408–418.

102 M. S. Mittenthal, B. S. Flowers, J. E. Bara, J. W. Whitley, S. K. Spear, J. D. Roveda, D. A. Wallace, M. S. Shannon, R. Holler, R. Martens and D. T. Daly, *Ind. Eng. Chem. Res.*, 2017, **56**, 5055–5069.

103 E. C. Achilleos, R. K. Prud'homme, I. G. Kevrekidis, K. N. Christodoulou and K. R. Gee, *Aiche J.*, 2000, **46**, 2128–2139.

104 S. Sotoudeh, G. Pourfallah, A. Barati, R. Davarnejad, M. A. Farahani and A. Memar, *Ind. Eng. Chem. Res.*, 2010, **49**, 10111–10115.

105 O. Uz Okay and S. B. Sariisik, *Eur. Polym. J.*, 2000, **36**, 393–399.

106 F. A. Escobedo and J. J. De Pablo, *Phys. Rep.*, 1999, **318**, 85–112.

107 S. A. Chester, C. V. Di Leo and L. Anand, *Int. J. Solids Struct.*, 2015, **52**, 1–18.

108 W. Hong, Z. Liu and Z. Suo, *Int. J. Solids Struct.*, 2009, **46**, 3282–3289.

109 Z. Duan, J. Zhang, Y. An and H. Jiang, 2013, *J. Appl. Mech.*, **80**, 041017.

110 A. Lucantonio, P. Nardinocchi and L. Teresi, *J. Mech. Phys. Solids*, 2013, **61**, 205–218.

111 D. P. Holmes, M. Roché, T. Sinha and H. A. Stone, *Soft Matter*, 2011, **7**, 5188.

112 M. Pezzulla, G. P. Smith, P. Nardinocchi and D. P. Holmes, *Soft Matter*, 2015, **12**, 4435–4442.

113 A. Lucantonio, P. Nardinocchi and M. Pezzulla, *Proc. R. Soc. A Math. Phys. Eng. Sci.*, 2014, **470**, 20140467.

114 L. Ionov, *Adv. Funct. Mater.*, 2013, **23**, 4555–4570.

115 D. P. Holmes, P.-T. Brun, A. Pandey and S. Protière, *Soft Matter*, 2016, **12**, 4886–4890.

116 H. S. Kim and A. J. Crosby, *Adv. Mater.*, 2011, **23**, 4188–4192.

117 D. P. Holmes, M. Ursiny and A. J. Crosby, *Soft Matter*, 2008, **4**, 82–85.

118 H. Lee, J. Zhang, H. Jiang and N. X. Fang, *Phys. Rev. Lett.*, 2012, **108**, 1–5.

119 M. Guvendiren, S. Yang and J. A. Burdick, *Adv. Funct. Mater.*, 2009, **19**, 3038–3045.

120 M. Guvendiren, J. A. Burdick and S. Yang, *Soft Matter*, 2010, **6**, 5795.

121 D. P. Holmes and A. J. Crosby, *Phys. Rev. Lett.*, 2010, **105**, 1–4.

122 D. P. Holmes and A. J. Crosby, *Adv. Mater.*, 2007, **19**, 3589–3593.

123 H. Lee, C. Xia and N. X. Fang, *Soft Matter*, 2010, **6**, 4342.

124 J.-L. Liu and X.-Q. Feng, *Acta Mech. Sin.*, 2012, **28**, 928–940.

125 L. Chen, E. Bonaccurso, T. Gambaryan-Roisman, V. Starov, N. Koursari and Y. Zhao, *Curr. Opin. Colloid Interface Sci*, 2018, **36**, 46-57.

126 J. Liu, J. Sun and Y. Mei, *J. Appl. Phys.*, 2013, **114**, 044901.

127 K. Rykaczewski and T. Burgin, *US Pat*, US20170321373A1, 2017.

128 C. J. Durning and K. N. Morman, *J. Chem. Phys.*, 1993, **98**, 4275–4293.

129 N. R. Kenkare, C. K. Hall and S. A. Khan, *J. Chem. Phys.*, 2000, **113**, 404–418.

130 X. Wang and W. Hong, *Proc. R. Soc. A Math. Phys. Eng. Sci.*, 2012, **468**, 3824–3841.

131 S. a Chester and L. Anand, *J. Mech. Phys. Solids*, 2010, **58**, 1879–1906.

132 J. Zhang, X. Zhao, Z. Suo and H. Jiang, *J. Appl. Phys.*, 2009, **105**, 093522.

133 D. Caccavo and G. Lamberti, *Mater. Sci. Eng. C*, 2017, **76**, 102–113.

134 N. Bouklas, C. M. Landis and R. Huang, *J. Mech. Phys. Solids*, 2015, **79**, 21–43.

135 J. N. Lee, C. Park and G. M. Whitesides, *Anal. Chem.*, 2003, **75**, 6544–6554.

136 X. Sun, S. Turnage, E. B. Iezzi, Y. Yang, B. Chang, N. C. Muthegowda, S. K. Balijepalli, N. Dhuyvetter, L. P. Wang, K. N. Solanki and K. Rykaczewski, *J. Coat. Technol. Res.*, 2017, **14**, 1247–1258.

137 T. Nguyen, D. Bentz and E. Byrd, *J. Coatings Technol.*, 1995, **67**, 37–46.

138 I. Linossier, F. Gaillard, M. Romand and J. F. Feller, *J. Appl. Polym. Sci.*, 1997, **66**, 2465–2473.

139 M. A. Awan and J. H. Dymond, *Int. J. Thermophys.*, 2001, **22**, 679–700.

140 A. Phadnis, K. C. Manning, I. Sanders, T. P. Burgin and K. Rykaczewski, *Soft Matter*, 2018, **14**, 5869–5877.

141 R. A. Orwoll and P. A. Arnold, *Phys. Prop. Polym. Handb.*, 2007, **50**, 451.

142 N. Otsu, *IEEE Trans. Syst. Man. Cybern.*, 1979, **20**, 62–66.

143 M. A. C. Stuart, W. T. S. Huck, J. Genzer, M. Müller, C. Ober, M. Stamm, G. B. Sukhorukov, I. Szleifer, V. V. Tsukruk, M. Urban, F. Winnik, S. Zauscher, I. Luzinov and S. Minko, *Nat. Mater.*, 2010, **9**, 101–113.

144 L. Hines, K. Petersen, G. Z. Lum and M. Sitti, *Adv. Mater.*, 2017, **29**, 1603483.

145 L. Ionov, *Mater. Today*, 2014, **17**, 494–503.

146 L. Dong, A. K. Agarwal, D. J. Beebe and H. Jiang, *Nature*, 2006, **442**, 551–554.

147 K. C. Manning, A. Phadnis, D. Simonet, T. P. Burgin and K. Rykaczewski, *Ind. Eng. Chem. Res.*, 2018, **57**, 13269–13274.

148 J. C. Wu and N. A. Peppas, *J. Polym. Sci. Part B Polym. Phys.*, 1993, **31**, 1503–1518.

149 A. Peterlin, *J. Polym. Sci. Polym. Phys. Ed.*, 1979, **17**, 1741–1756.

150 L. A. Weisenberger and J. L. Koenig, *Macromolecules*, 1990, **23**, 2445–2453.

151 V. Badilita, R. C. Meier, N. Spengler, U. Wallrabe, M. Utz and J. G. Korvink, *Soft Matter*, 2012, **8**, 10583–10597.

152 L. G. Raguin, E. P. Office and S. Prakash, *MRS Online Proc. Libr. Arch.*, 2006, **930**.

153 C. Sammon, J. Yarwood and N. Everall, *Polymer (Guildf).*, 2000, **41**, 2521–2534.

154 D. Vesely, *Int. Mater. Rev.*, 2008, **53**, 299–315.

155 Y. Hu, X. Zhao, J. J. Vlassak and Z. Suo, *Appl. Phys. Lett.*, 2010, **96**, 121904.

156 H. L. Frisch, *Polym. Eng. Sci.*, 1980, **20**, 2–13.

157 T. T. Wang, T. K. Kwei and H. L. Frisch, *J. Polym. Sci. Part A-2 Polym. Phys.*, 1969, **7**, 2019–2028.

158 N. A. Peppas, *Pharm. Acta Helv.*, 1985, **60**, 110–111.

159 P. L. Ritger and N. A. Peppas, *J. Control. Release*, 1987, **5**, 23–36.

160 R. W. Korsmeyer, S. R. Lustig and N. A. Peppas, *J. Control. Release*, 1988, **7**, 61–68.

161 N. A. Peppas and J. J. Sahlin, *Int. J. Pharm.*, 1989, **57**, 169–172.

162 C. Y. Hui, K. C. Wu, R. C. Lasky and E. J. Kramer, *J. Appl. Phys.*, 1987, **61**, 5129–5136.

163 C. Y. Hui, K. C. Wu, R. C. Lasky and E. J. Kramer, *J. Appl. Phys.*, 1987, **61**, 5137–5149.

164 J. Crank, *The Mathematics of Diffusion*, Oxford University Press, 1975.

165 J. S. Vrentas and C. M. Vrentas, *Macromolecules*, 1994, **27**, 5570–5576.

166 M. P. Tonge and R. G. Gilbert, *Polymer (Guildf).*, 2001, **42**, 501–513.

167 L. Masaro and X. X. Zhu, *Prog. Polym. Sci.*, 1999, **24**, 731–775.

168 H. Fujita, in *Fortschritte Der Hochpolymeren-Forschung*, Springer Berlin Heidelberg, Berlin, Heidelberg, 1961, 1–47.

169 R. A. Waggoner, F. D. Blum and J. M. D. MacElroy, *Macromolecules*, 1993, **26**, 6841–6848.

170 M. L. Oyen, *Int. Mater. Rev.*, 2014, **59**, 44–59.

171 C. C. White, M. R. Vanlandingham, P. L. Drzal, N. K. Chang and S. H. Chang, *J. Polym. Sci. Part B Polym. Phys.*, 2005, **43**, 1812–1824.

172 E. P. Chan, Y. Hu, P. M. Johnson, Z. Suo and C. M. Stafford, *Soft Matter*, 2012, **8**, 1492–1498.

173 B. Rousseau and J. Petravic, *J. Phys. Chem. B*, 2002, **106**, 13010–13017.

174 Y. Hu, E. P. Chan, J. J. Vlassak and Z. Suo, *J. Appl. Phys.*, 2011, **110**, 086103.

175 P. J. Flory and J. Rehner, *J. Chem. Phys.*, 1943, **11**, 512–520.

176 R. Young and P. Lovell, *Introduction to Polymers*, CRC Press, 2011.

177 S. A. Chester and L. Anand, *J. Mech. Phys. Solids*, 2010, **58**, 1879–1906.

178 M. Karimi, A. A. Tashvigh, F. Asadi and F. Z. Ashtiani, 2016, **6**, 9013–9022.

179 H. Ertl and F. A. L. Dullien, *AIChE J.*, 1973, **19**, 1215–1223.

180 N. L. L. Thomas and A. H. H. Windle, *Polymer (Guildf).*, 1980, **21**, 613–619.

181 K. P. Gurton, M. Felton, R. Dahmani and D. Ligon, *Appl. Opt.*, 2007, **46**, 6323–9.

182 W. E. Steiner, S. J. Klopsch, W. A. English, B. H. Glowers and H. H. Hill, *Anal. Chem.*, 2005, **77**, 4792–4799.

183 A. N. Martin, G. R. Farquar, M. Frank, E. E. Gard and D. P. Fergenson, *Anal. Chem.*, 2007, **79**, 6368–6375.

184 S. Kim and K. J. Kim, *J. Heat Transfer*, 2011, **133**, 081502.

185 G. Lu, Y. Y. Duan, X. D. Wang and D. J. Lee, *Int. J. Heat Mass Transf.*, 2011, **54**, 4437–4447.

186 A. Chandramohan, S. Dash, J. A. Weibel, X. Chen and S. V. Garimella, *Langmuir*, 2016, **32**, 4729–4735.

APPENDIX A

SUPPORTING INFORMATION FOR CHAPTER 2

A1. Experimental setup

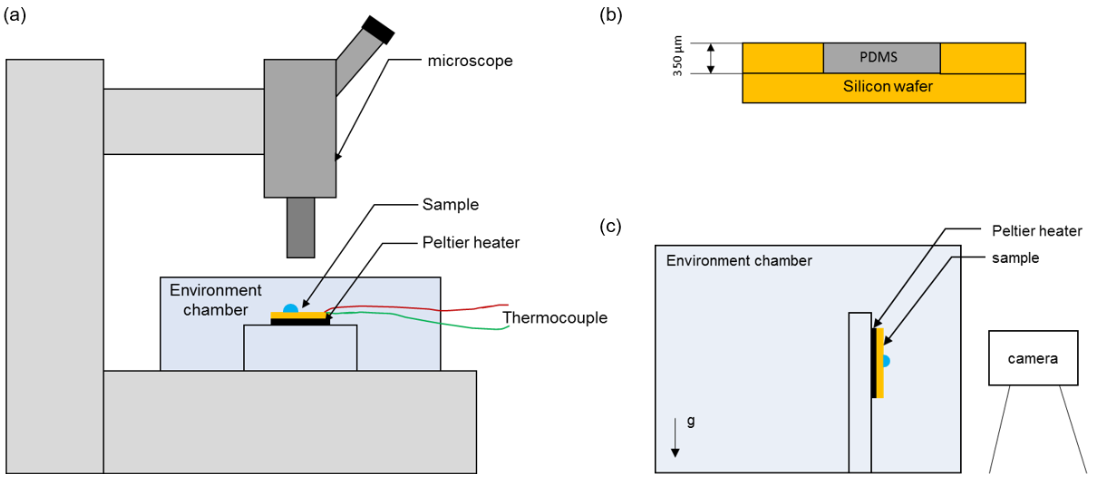

Figure A1. Schematic views of the experimental setup used to determine (a) droplet nucleation density and (c) shedding diameter. The schematic in (b) shows setup of a PDMS sample.

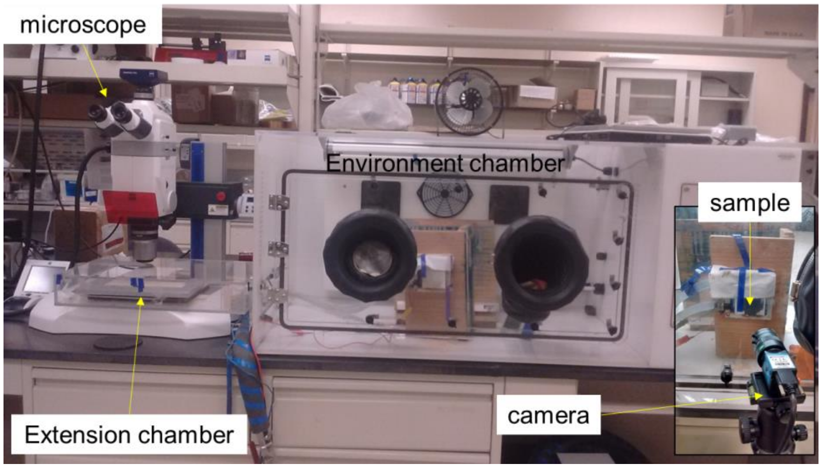

Figure A2. Image of the experimental setup used for conducting the condensation experiments.

A2. Deformation due to droplets smaller than elastocapillary length

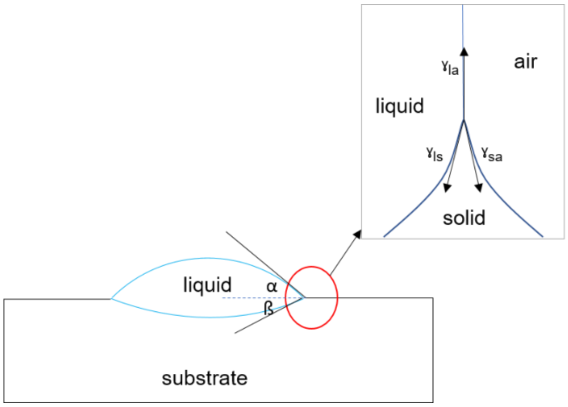

Figure A3. Schematic showing deformation of a liquid substrate by a water droplet

Force balance at the triple phase contact line gives-

$$\gamma_{la} cos\beta + \gamma_{ls} cos\alpha = \gamma_{sa}$$

$$\gamma_{la} sin\beta = \gamma_{ls} sin\alpha$$

Solving for α, β we get-

$$cos\alpha = \frac{\gamma_{la}^2 + \gamma_{ls}^2 - \gamma_{sa}^2}{2\gamma_{ls}\gamma_{sa}}$$

$$cos\beta = \frac{\gamma_{sa}^2 + \gamma_{la}^2 - \gamma_{ls}^2}{2\gamma_{sa}\gamma_{la}}$$

Also, from geometry,

$$R_u sin\beta = R_L sin\alpha$$

Where R_u is radius of curvature of liquid-vapor interface and R_L is radius of curvature of liquid-solid interface. Another equation used to solve for two variables system is the volume equation. We consider a known radius droplet to calculate the volume. The solution of these system of equations gives a complete formulation to build a geometry for a droplet of a size smaller than the elastocapillary radius. The values used for γ_{la}, γ_{ls} and γ_{sa} are 72 mN/m, 41 nN/m and 39 mN/m, respectively. The corresponding values of α and β are 51° and 26.5°consituting radius of curvature $R_u = 938$ nm and $R_L = 534$ nm, respectively.

A3. DWC heat transfer with varied droplet distribution scenarios

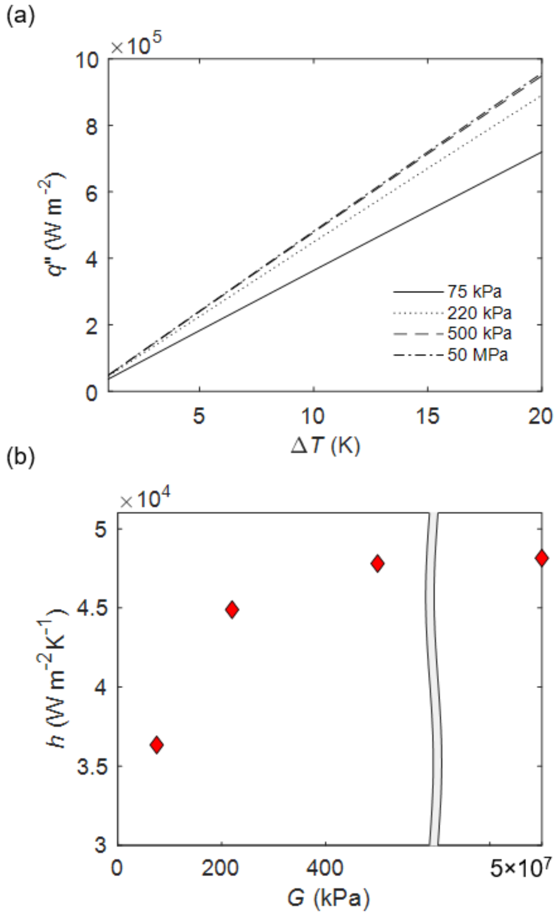

Figure A4. (a) Comparison of heat transfer rate per unit condenser area for different substrates and subcooling levels; the inset shows heat transfer rate per unit condenser area at subcooling of 5 K plotted against increasing substrate moduli from 75 kPa to 50 GPa, and (b) comparison of DWC condensation heat transfer coefficient, h, plotted against the substrate elastic modulus, *G*. In this case the cutoff size between the droplets defined by Yu *et al.*[65] model and the liquid-on-liquid shape from $r < r_{el}$ to $r < 2\, r_{el}$.

A4. Sample properties

As explained in the text, three PDMS samples were prepared along with a silicon wafer coated with monolayer of flurosilane. Following table summarizes the relevant properties:

Table A1. Properties of the samples

	PDMS 10:1	PDMS 20:1	PDMS 33:1	Silicon
Shear modulus, kPa	500	220	75	50000
Contact angle, °	104.5	118	124	110.6
CAH, °	16.2	11	5.4	16.4

A5. COMSOL model benchmarking and verification

To verify the modeling assumptions and methodology, the model is first benchmarked against the results published in the literature. As mentioned earlier, heat transfer through condensate droplet occurs through conduction and Marangoni convection. In the following section, the model is benchmarked separately with conduction model followed by benchmarking of combined flow (conduction + Marangoni) model.

Conduction only model

The conduction only model results have been compared with the model proposed Kim and Kim [184]. The conduction heat transfer rate through a droplet on a hydrophobic surface has been estimated using equation 1. The COMSOL model is simulated for the conditions mentioned in the paper and the results have been compared in Figure A5.

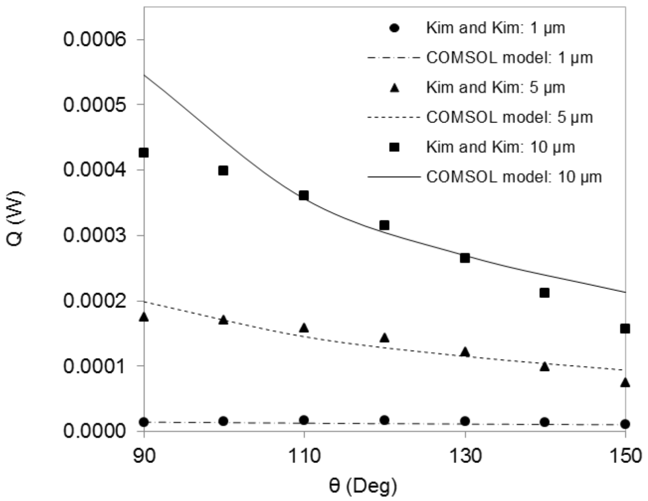

Figure A5. Comparison of total heat transfer rates through condensate water droplet between COMSOL conduction model and the analytical model by Kim and Kim [184].

Three different sizes of droplets have been considered- 1 µm, 5 µm, and 10 µm. Heat transfer rate is estimated for each droplet size for equilibrium contact angles ranging from 90º to 150º. Interfacial heat transfer coefficient is taken to be 0.32 MW/m^{2}K. Preset model compared well for 1 µm and 5 µm, with maximum difference of 3.5 % in the 10 µm droplet. Its worth noting that Chavan et al.[63] showed that Kim and Kim model under predicts the heat transfer due to inappropriate boundary conditions.

Conjugate heat transfer model

Once the conduction model has been verified, Marangoni flow is simulated in the same manner. Before we use this model to estimate the heat transfer rates, the Marangoni flow field predicted by the model needs to be verified. The flow field inside the droplet predicted by the numerical model is thus benchmarked against the results provided by Lu *et al* [185]. In this study, authors studied the flow field inside the evaporating droplet on a hydrophilic surface. Since, the substrate is hotter than the droplet, bouncy driven flow is also present along with the Marangoni flow. Following three cases are considered- only buoyancy driven flow is present, only Marangoni flow is present, and both flows are present in the droplet. The comparison for all the three cases has been provided in the Figure A6.

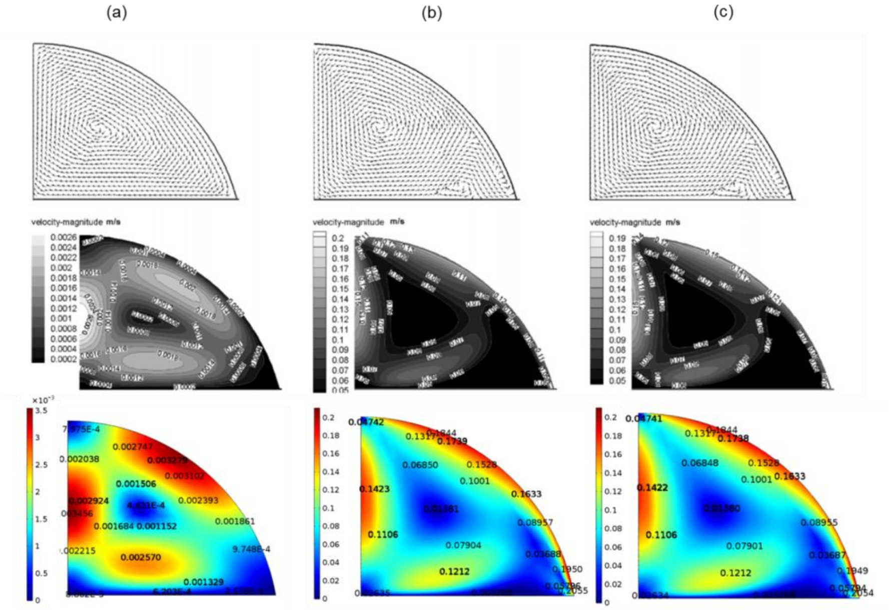

Figure A6. Comparison of flow field from the numerical model with Lu *et al.*[185] for following cases: (a) buoyant flow only, (b) Marangoni flow only and (c) buoyancy + Marangoni flow.

Validation

Apart from comparison with analytical and numerical studies, present model is also validated against the experimental results presented by Chandramohan *et al.*[186]. The authors conducted an experiment on a methanol droplet on a hydrophobic surface with the substrate temperature lower than the droplet. A laser assisted PIV technique has been used to visualize the flow field inside the droplet. The COMSOL is model is simulated for the experimental conditions and the results have been compared as shown in Figure A7.

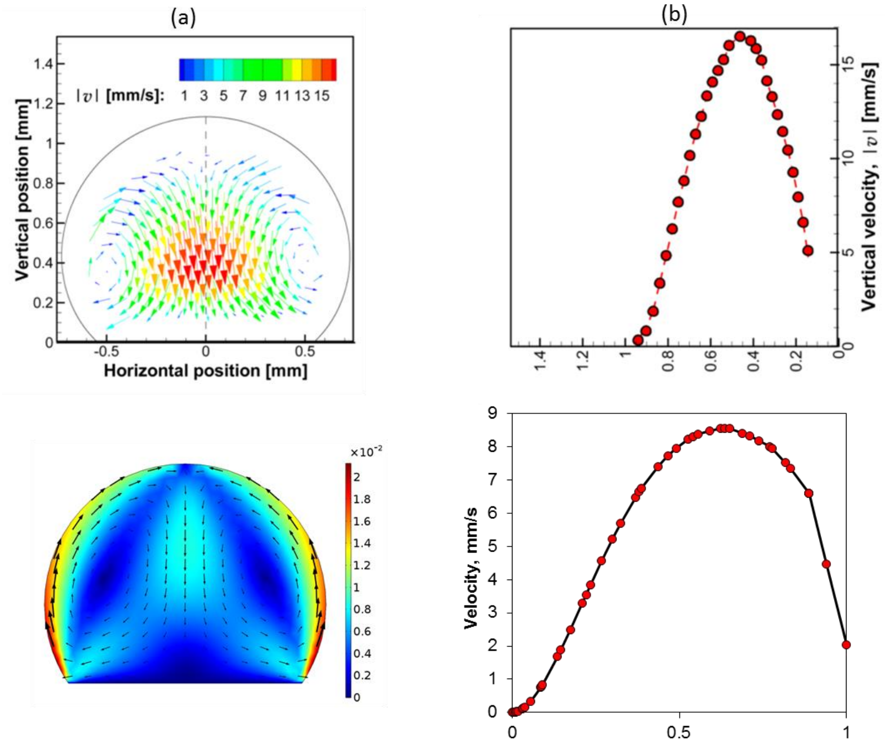

Figure A7. Comparison of results with Chandramohan *et al*[186]: (a) Marangoni flow field inside methanol droplet on a super hydrophobic surface, (b) Vertical velocity at the centerline of the droplet (at 0 mm)

A6. Impact of interfacial heat transfer coefficient

As given by equation 8, the interfacial heat transfer coefficient takes into account the presence of non-condensable gases in the steam (or vapor of organic liquid) through accommodation coefficient, γ. The results presented in the main text correspond to the accommodation coefficient of 0.04. Here we show results corresponding to the values of different accommodation coefficients. Table S1 summarizes heat transfer coefficients for water at saturation temperature of 373 K.

Table A2. Interfacial heat transfer coefficient variation with accommodation coefficient

γ	0.1	0.5	0.75	1.0
h_{i}, $Wm^{-2}K^{-1}$	815552.5	5165166.0	9297298.8	15495498.0

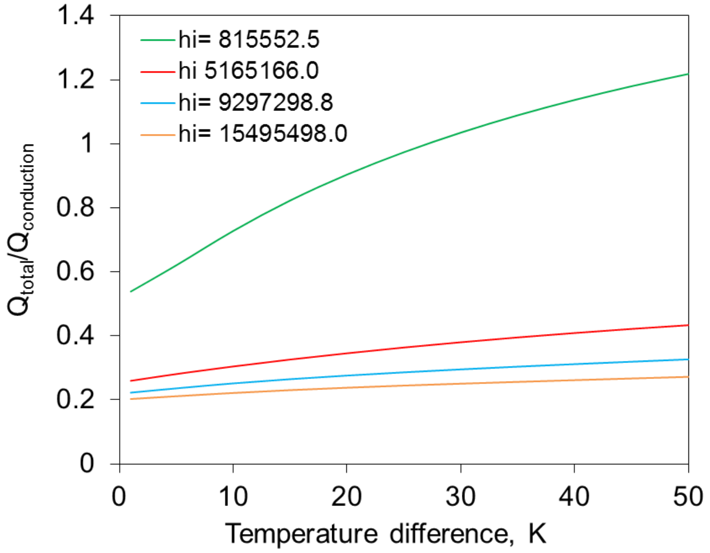

Figure A8. Variation of heat transfer ratio with degree of subcooling for different values of interfacial heat transfer coefficient (in W/m^2K).

A7. Model results- conduction

The results discussed in the main article are concerned with the case where Marangoni flow and conduction are both simulated. Here, we summarize the temperature results for conduction only case compared with temperatures for Marangoni flow simulated case.

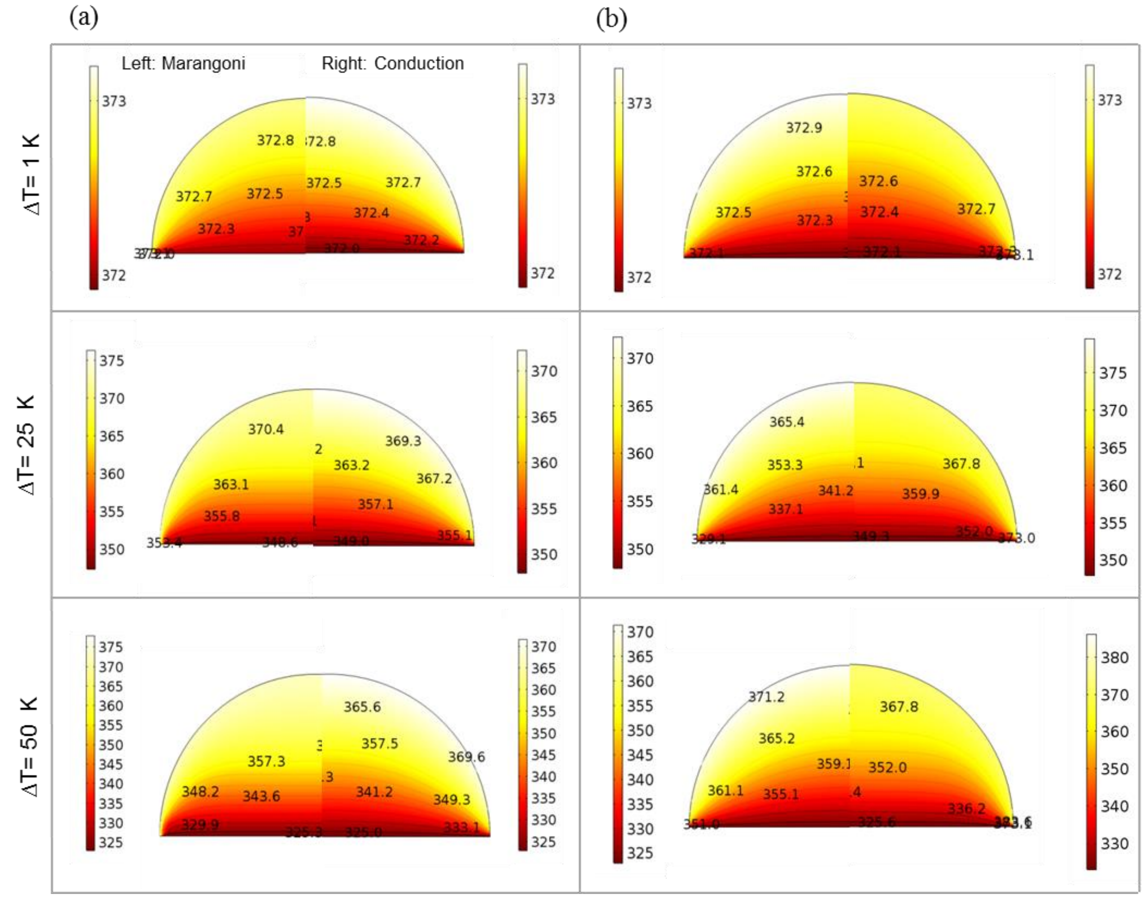

Figure A9. Temperature field results inside condensate water droplet of size (a) 1 μm and (b) 1 mm radius for three values of temperature difference- 1 K, 25 K and 50 K at saturation temperature of 373 K.

A8. Heat transfer ratio for *T*$_{sat}$ = 313 K

The heat transfer ratio is plotted against the degree of sub-cooling for droplet radius ranging from 100 nm to 1 mm in Figure A10. The trends agree with those shown in Figure 2.6 in the main text. At the same time, the values of heat transfer ratios lie between the values for T_{sat} = 297 K and 373 K. A linear increase in surface tension gradient with respect to the temperature results in increased heat transfer with the temperature.

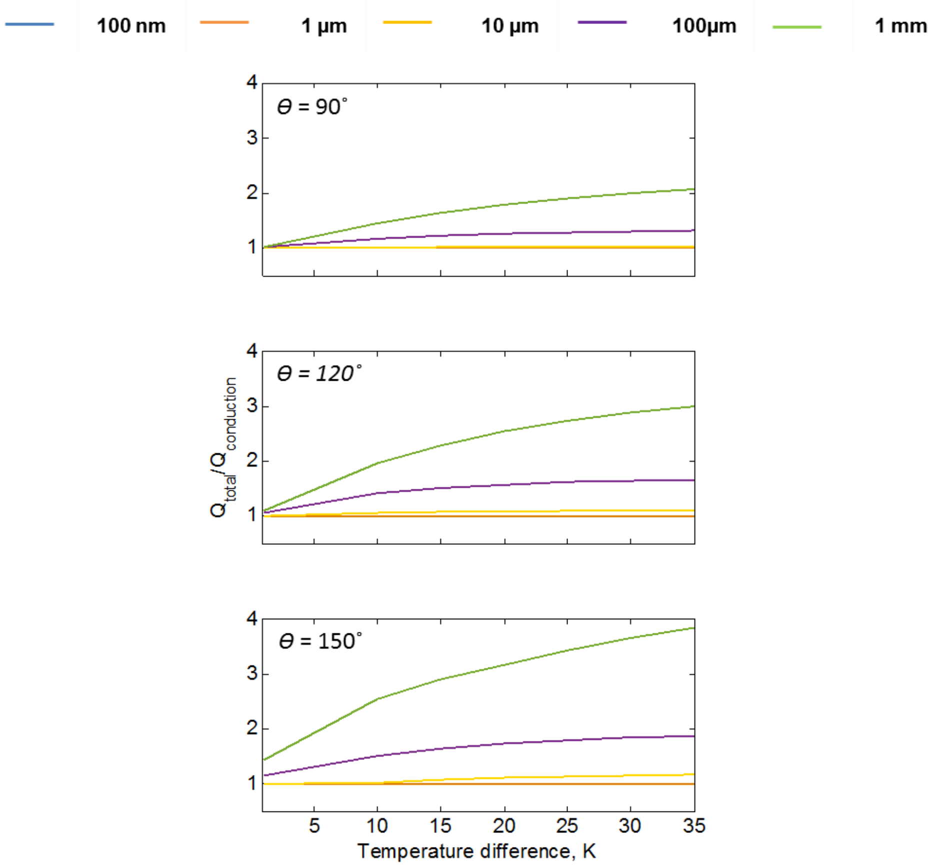

Figure A10. Heat transfer ratio (plotted on y-scale) across water droplet for saturation temperature of 313 K with contact angles, θ, of 90º, 120º and 150º.

A9. Heat flux ratio across solid-liquid interface for θ = 150°

Figure A11 shows comparison of heat flux ratios between three different degrees of subcooling for a dropelt with contact angle of 150° and radius 1 µm (Figure A11a) and 1 mm (Figure A11b). The maximum heat transfer ratio of 6 is obtained for 1 mm droplet.

The reason for this increase is well established from 14 fold increrase in the TPL heat flux as shown in Figure A11b.

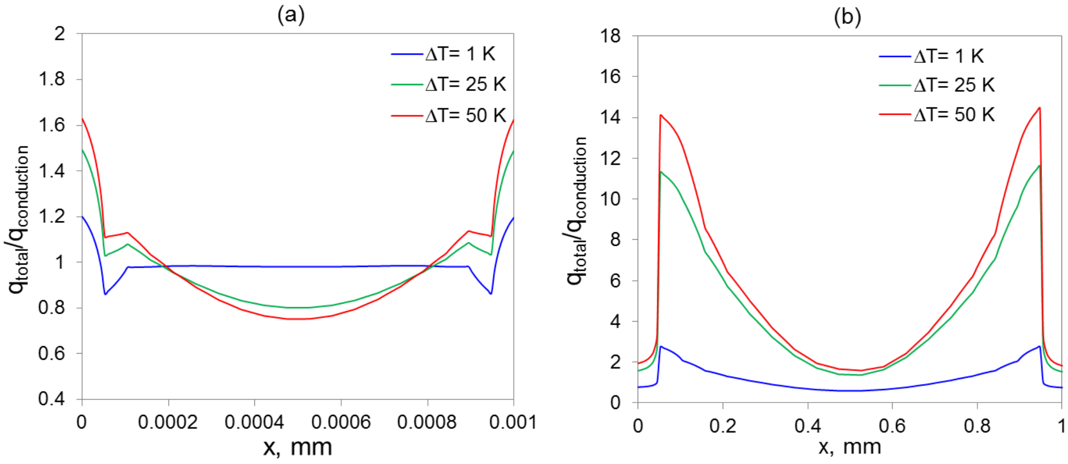

Figure A11. Heat flux ratio plotted across solid-liquid interface of (a) 1 µm and (b) 1 mm droplet size for three values of sub-cooling**.**

A10. Shear stress at the solid-liquid interface

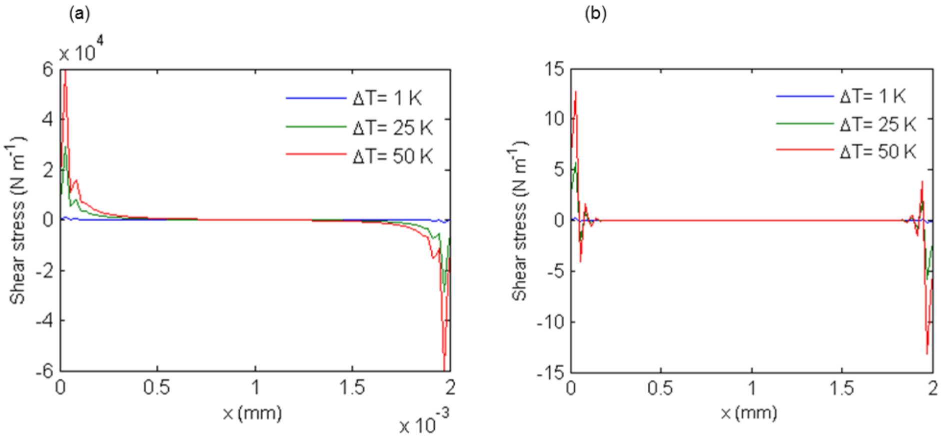

Figure A12. Shear stress at the solid-liquid interface of (a) 1 µm and (b) 1 mm water droplet size for three values of sub-cooling**.**

APPENDIX B

THE EFFECT OF MARANGONI CONVECTION ON HEAT TRANSFER DURING DROPWISE CONDENSATION ON HYDROPHOBIC AND OMNIPHOBIC SURFACES

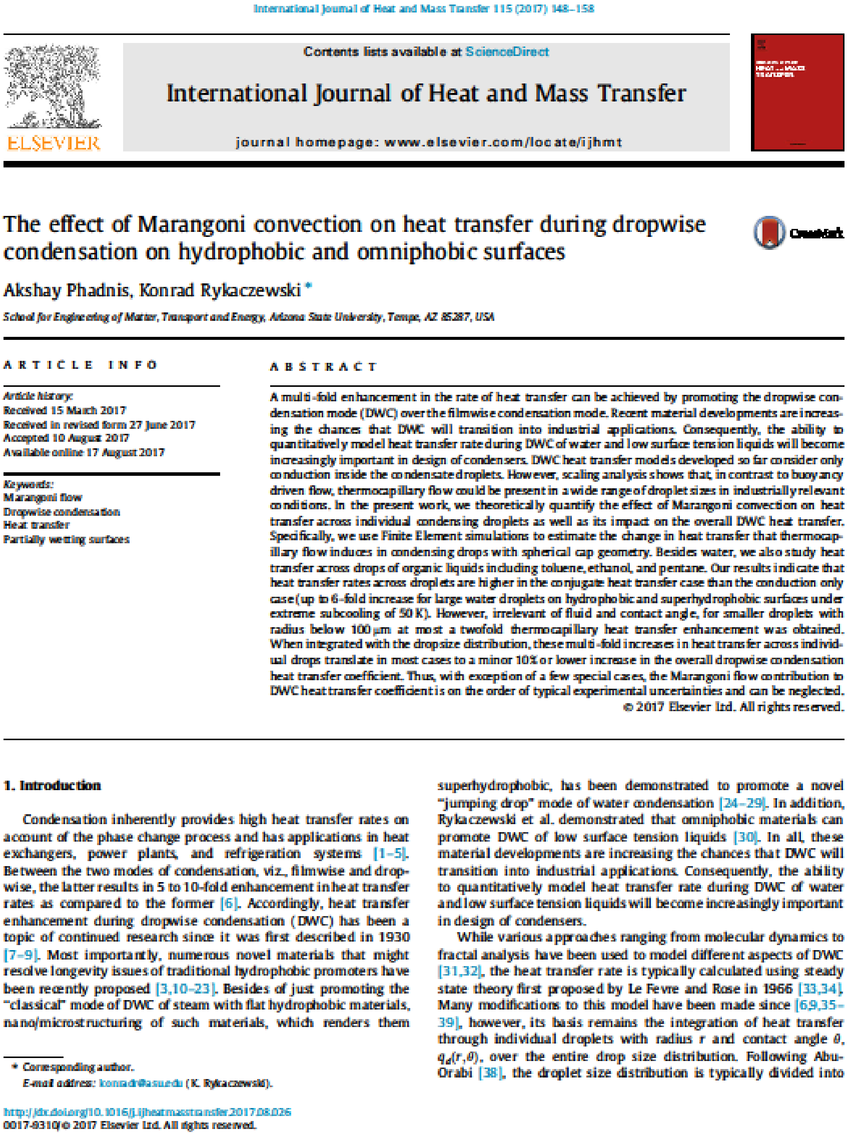

International Journal of Heat and Mass Transfer 115 (2017) 148–158

Contents lists available at ScienceDirect

International Journal of Heat and Mass Transfer

journal homepage: www.elsevier.com/locate/ijhmt

The effect of Marangoni convection on heat transfer during dropwise condensation on hydrophobic and omniphobic surfaces

Akshay Phadnis, Konrad Rykaczewski *

School for Engineering of Matter, Transport and Energy, Arizona State University, Tempe, AZ 85287, USA

ARTICLE INFO

Article history:
Received 15 March 2017
Received in revised form 27 June 2017
Accepted 10 August 2017
Available online 17 August 2017

Keywords:
Marangoni flow
Dropwise condensation
Heat transfer
Partially wetting surfaces

ABSTRACT

A multi-fold enhancement in the rate of heat transfer can be achieved by promoting the dropwise condensation mode (DWC) over the filmwise condensation mode. Recent material developments are increasing the chances that DWC will transition into industrial applications. Consequently, the ability to quantitatively model heat transfer rate during DWC of water and low surface tension liquids will become increasingly important in design of condensers. DWC heat transfer models developed so far consider only conduction inside the condensate droplets. However, scaling analysis shows that, in contrast to buoyancy driven flow, thermocapillary flow could be present in a wide range of droplet sizes in industrially relevant conditions. In the present work, we theoretically quantify the effect of Marangoni convection on heat transfer across individual condensing droplets as well as its impact on the overall DWC heat transfer. Specifically, we use Finite Element simulations to estimate the change in heat transfer that thermocapillary flow induces in condensing drops with spherical cap geometry. Besides water, we also study heat transfer across drops of organic liquids including toluene, ethanol, and pentane. Our results indicate that heat transfer rates across droplets are higher in the conjugate heat transfer case than the conduction only case (up to 6-fold increase for large water droplets on hydrophobic and superhydrophobic surfaces under extreme subcooling of 50 K). However, irrelevant of fluid and contact angle, for smaller droplets with radius below 100 μm at most a twofold thermocapillary heat transfer enhancement was obtained. When integrated with the dropsize distribution, these multi-fold increases in heat transfer across individual drops translate in most cases to a minor 10% or lower increase in the overall dropwise condensation heat transfer coefficient. Thus, with exception of a few special cases, the Marangoni flow contribution to DWC heat transfer coefficient is on the order of typical experimental uncertainties and can be neglected.

© 2017 Elsevier Ltd. All rights reserved.

1. Introduction

Condensation inherently provides high heat transfer rates on account of the phase change process and has applications in heat exchangers, power plants, and refrigeration systems [1–5]. Between the two modes of condensation, viz., filmwise and dropwise, the latter results in 5 to 10-fold enhancement in heat transfer rates as compared to the former [6]. Accordingly, heat transfer enhancement during dropwise condensation (DWC) has been a topic of continued research since it was first described in 1930 [7–9]. Most importantly, numerous novel materials that might resolve longevity issues of traditional hydrophobic promoters have been recently proposed [3,10–23]. Besides of just promoting the "classical" mode of DWC of steam with flat hydrophobic materials, nano/microstructuring of such materials, which renders them superhydrophobic, has been demonstrated to promote a novel "jumping drop" mode of water condensation [24–29]. In addition, Rykaczewski et al. demonstrated that omniphobic materials can promote DWC of low surface tension liquids [30]. In all, these material developments are increasing the chances that DWC will transition into industrial applications. Consequently, the ability to quantitatively model heat transfer rate during DWC of water and low surface tension liquids will become increasingly important in design of condensers.

While various approaches ranging from molecular dynamics to fractal analysis have been used to model different aspects of DWC [31,32], the heat transfer rate is typically calculated using steady state theory first proposed by Le Fevre and Rose in 1966 [33,34]. Many modifications to this model have been made since [6,9,35–39], however, its basis remains the integration of heat transfer through individual droplets with radius r and contact angle θ, $q_d(r,\theta)$, over the entire drop size distribution. Following Abu-Orabi [38], the droplet size distribution is typically divided into

---

* Corresponding author.
E-mail address: konradr@asu.edu (K. Rykaczewski).

http://dx.doi.org/10.1016/j.ijheatmasstransfer.2017.08.026
0017-9310/© 2017 Elsevier Ltd. All rights reserved.

APPENDIX C

SUPPORTING INFORMATION FOR CHAPTER 3

C1. Solvent uptake comparison and validation

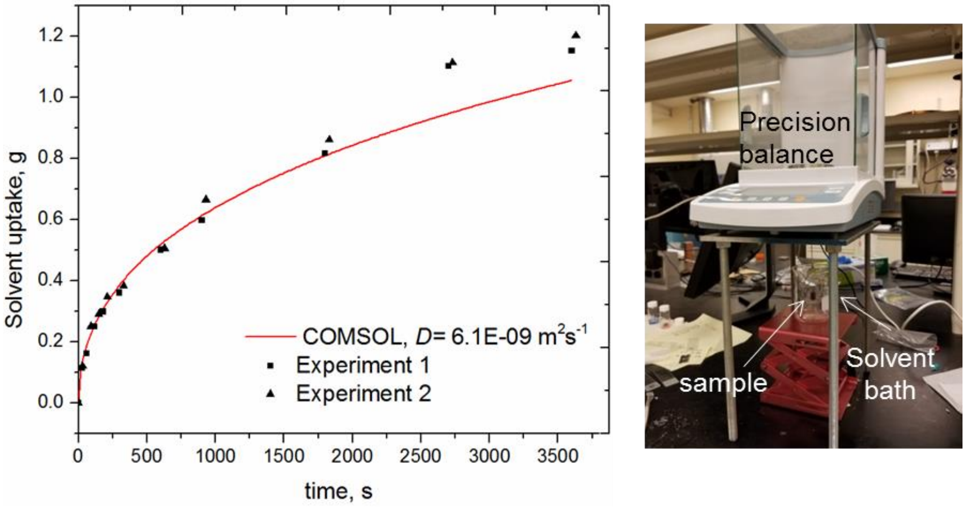

Figure C1. Comparison of solvent uptake with time between FE model predictions and the two experiments conducted on the cylindrical samples. On the right is the experimental setup used to measure the solvent uptake of PDMS.

The model predicted solvent uptake is compared with the experimentally measured values. The experiments were conducted on two different samples. The red line corresponds to the numerical values predicted by the COMSOL model. This is not done by fitting the experimental data but by using diffusion coefficient of 6.1×10^{-9} m^2s^{-1} and the appropriate boundary conditions. A slight deviation at higher time points is due to an additional solvent held in the convex shaped top surface resulting in higher values.

C2. Equilibrium swelling ratio

The equilibrium swelling ratio defined as the ratio of swollen volume to the dry volume can be calculated from above results as follows:

Volume of the dry polymer = 1.055 cm^3

Volume of the solvent absorbed = 1.8 cm^3

S_{eq} = (1.8+1.055)/ 1.055 = 2.71

At the same time, volumetric or bulk strain can be estimated as –

$\epsilon_{bulk} = 1.8/1.055{=}1.706$

C3. Assumptions in the numerical model

It should be noted that the chemical potential in Equation 5b represents the chemical potential of solvent inside gel relative to that of the pure solvent. Thus, on the boundary, where the chemical potential of gel equilibrates with the outside solvent, we use $\mu = \mu_0 = 0$. However, assumption of a perfect equilibrium poses a challenge in terms of concentration of the solvent at the boundary. Consider free swelling of a cubical polymer sample when completely immersed in the solvent bath. At equilibrium, the stresses inside the gel vanish because of absence of any constraint and from Equations 5a and 5b we can write-

$$\mu_0 = RT\left(\log\left(\frac{\Omega J_0 c_{eq}}{1+\Omega J_0 c_{eq}}\right) + \frac{1}{1+\Omega J_0 c_{eq}} + \frac{\chi}{\left(1+\Omega J_0 c_{eq}\right)^2}\right) + \frac{G\Omega}{\lambda_{eq}} \qquad \text{(C-1)}$$

Where, c_{eq} is equilibrium concentration and λ_{eq} is the equilibrium stretching ratio such that equilibrium swelling ratio $J_{eq} = \lambda_{eq}^3$. For given values of $T = 298$ K and $\chi = 0.39$, $G = 75$ kPa and $\Omega = 3\times10^{-4}$ $\text{m}^3\,\text{mol}^{-1}$, the equilibrium concentration for hexane is $c_{eq} = 22000$ mol m^{-3}. This value is significantly higher than the expected concentration of 7650 mol m^{-3}. This discontinuity is believed to be resulting due to assumptions associated with

Flory-Rehner free energy calculation. This formulation neglects free energy of mixing underestimating the free energy resulting in higher concentration. We estimated that, $\mu_0 =$ -236 J mol^{-1} when $c_{eq} =$ 7650 mol m^{-3} which is not considerably different from the ideal equilibrium. However, to be consistent with the literature we use $\mu_0 = 0$. Also, the effect of using $\mu_0 =$ -236 J mol^{-1} instead of ideal equilibrium value on displacement is within $\pm$ 0.15 mm.

C4. FTIR-ATR experiments and results

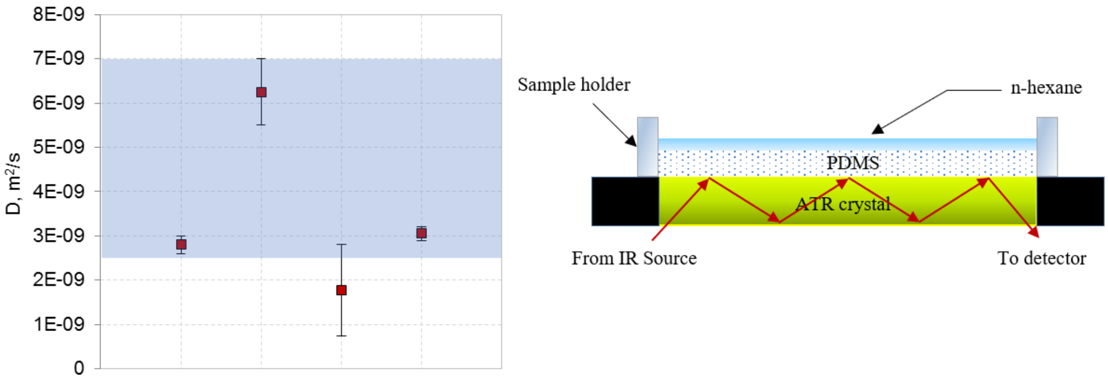

Figure C2. Measurement of the diffusion coefficient of n-hexane in PDMS using FTIR-ATR technique.

C5. Hexane droplet spreading and absorption

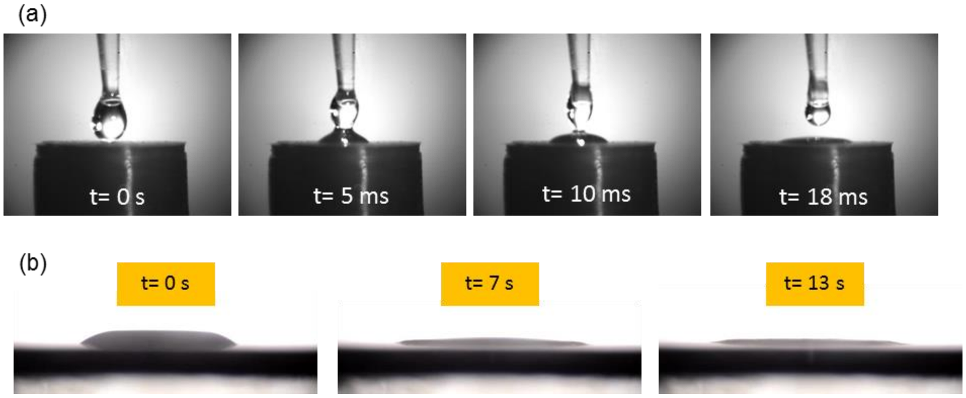

Figure C3. (a) High speed imaging of hexane droplet spreading on PDMS sample and (b) Images of absorption of hexane droplet in PDMS sample with time.

C6. Wrinkle formation and crumpling of thin films (case (iv))

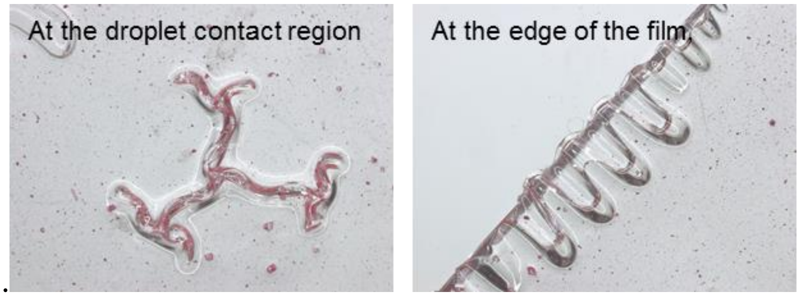

Figure C4. Crumpling due to swelling instabilities in thin PDMS samples after injecting 3−5 drops of hexane (~30−50 μL). Thickness of the film is 110 μm.

The films are obtained by spin coating PDMS on glass slides of size 25.4×25.4 mm. We expect this to happen because for a thin film of thickness ≪ droplet size, the solvent diffuses rapidly and fills the gap between PDMS and glass slide and results into inelastic crumpling instabilities.

C7. Experimental setup

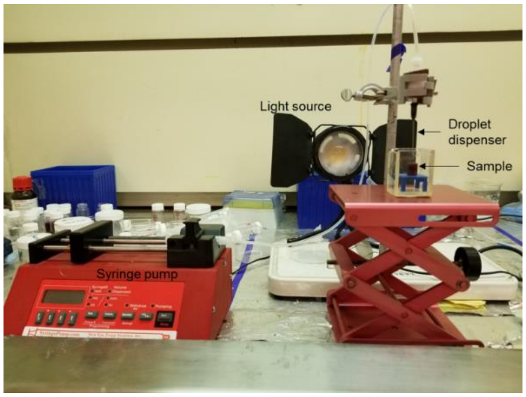

Figure C5. Experimental setup used to measure the swelling of polymer samples.

APPENNDIX D

SUPPORTING INFORMATION FOR CHAPTER 4

D1. 1-D assumption in a long thin cylinder

Chemical species transport equation in axisymmetric cylindrical coordinates is given by-

$$\bar{J} = -M(c)\left[\frac{1}{r}\frac{\partial}{\partial r}(r\mu) + \frac{\partial \mu}{\partial z}\right]$$

Now for a cylinder of initial radius R_0 and length L_0, we define two non-dimensional variables as $r^* = \frac{r}{R_0} \sim 1$ and $z^* = \frac{z}{L_0} \sim 1$. Since the order of magnitude of these non-dimensional numbers is unity, we re-write the transport equation as follows-

$$\bar{J} = -M(c)\left[\frac{1}{R_0 r^*}\frac{\partial}{\partial r^*}(r^*\mu) + \frac{1}{L_0}\frac{\partial \mu}{\partial z^*}\right] = -\frac{M(c)}{R_0}\left[\frac{1}{r^*}\frac{\partial}{\partial r^*}(r^*\mu) + \frac{R_0}{L_0}\frac{\partial \mu}{\partial z^*}\right]$$

First term in the bracket scales as $\frac{1}{r^*}\frac{\partial}{\partial r^*}(r^*\mu) \sim \mu$ while the second term scales as $\frac{R_0}{L_0}\frac{\partial \mu}{\partial z^*} \sim \frac{R_0}{L_0}\mu$

In this case, we have a long thin cylinder where $L_0 \gg R_0$ thus the second term in the bracket becomes negligible with respect to the first term and thus can be ignored without loss of accuracy. Henceforth, all the analysis pertains to this simplified 1-D assumption.

D2. Differential Scanning Calorimetry of NBPA-33

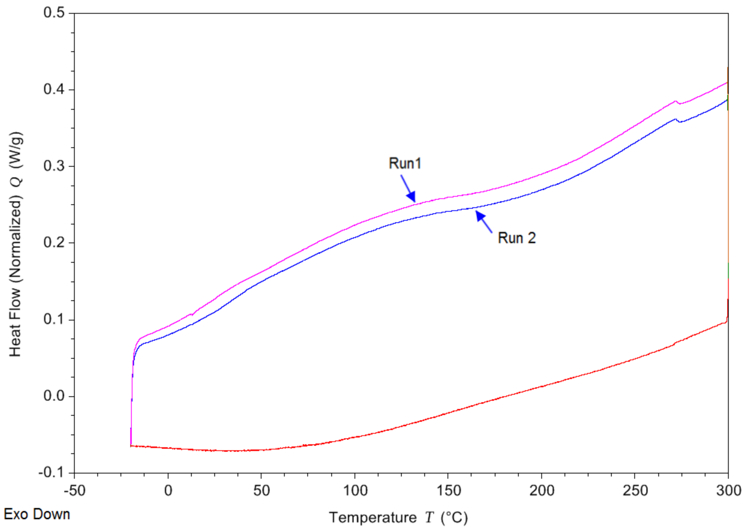

Figure D1. Results from Differential Scanning Calorimetry done on NBPA-33. The two lines correspond with two consecutive runs. No sharp peak observed during heating cycle.

Before we characterize the diffusion of *o*-xylene in NBPA-33, we determine the polymer crystal structure. Crystal structure forms a good basis for understanding the diffusion mode in the polymer. For example, most crystalline and semi-crystalline polymers exhibit case II behavior. To find out the crystal structure of NBPA-33, we performed Differential Scanning Calorimetry (DSC2500, TA instruments). We performed temperature sweep from –20 °C to 300 °C and repeated the cycle three times. The results showed an absence of any crystallinity in NBPA-33, making it’s a glassy amorphous polymer (see DSC results in Appendix D). This result is important because, with an amorphous structure, the mobility tensor can be assumed to be isotropic. Using this result, we discuss the characterization of NBPA-33 using gravimetric analysis and indentation to estimate swelling ratio, diffusion coefficient(s) and mechanical modulus required to implement the theory of poroelasticity.

D3. Contribution of fickian vs relaxation components of the diffusion

To quantitively measure the contribution of two diffusion modes in the polymer, we use a mixed treatment suggested by Peppas and Sahlin[161]-

$$\frac{M}{M_\infty} = k_1 t^{0.45} + k_2 t^{0.9}$$

For the cylindrical geometry. Using JMP, we fit the gravimetry data and estimated $k_1 = 0.026$ and $k_2 = 0.0014$. Thus, the coefficient of fickian transport is approximately an order of magnitude higher than that of relaxation transport.

D4. Raman Spectroscopy Imaging (RSI)

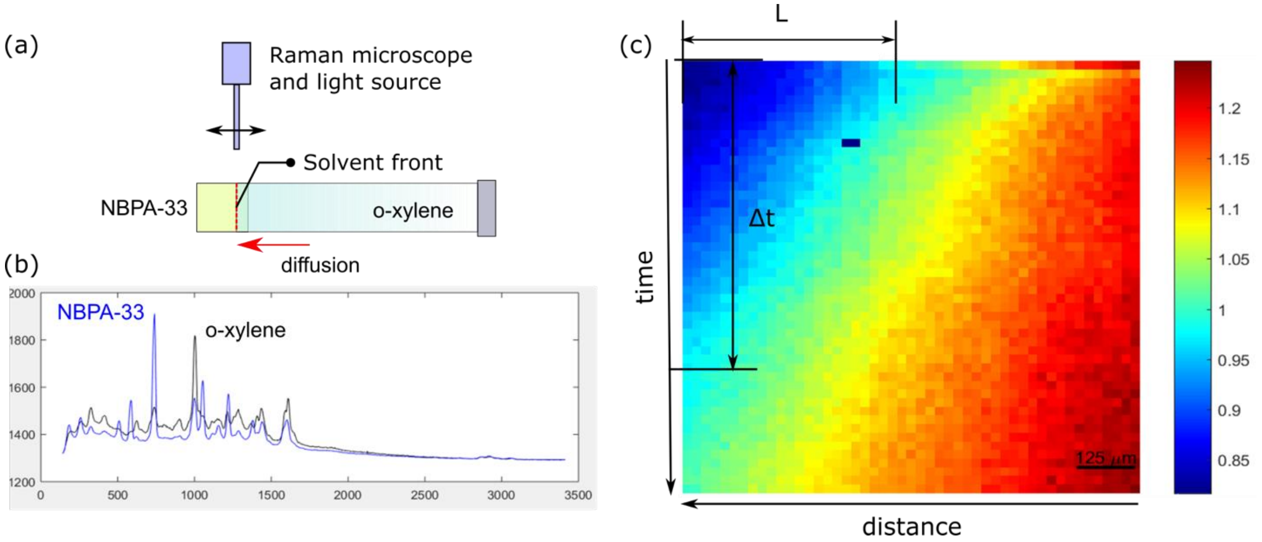

Figure D2. (a) Schematic of experiment configuration used for RSI, (b) Spectrum graphs of Raman shift recorded for pure polymer and solvent and (c) Raman shift response intensity ratio plotted along the length of ±0.5 mm from initial polymer front (total 1 mm) at different time points. Propagation of the solvent front can be seen with the diminishing blue color corresponding to the dry polymer.

D5. Estimation of D_0 using analytical expression

We calculate D_0 from the analytical solution developed by Crank[164] approximating 1-D diffusion along the radial direction in a long cylinder. Crank developed the following expression, based on solvent uptake of a cylindrical sample, to calculate the limiting diffusion coefficient, in this case, D_0:

$$\frac{M(t)}{M_\infty} = 1 - \sum_{n=1}^{\infty} \frac{4}{a^2 \alpha_n^2} exp[-D_0 \alpha_n^2 t]$$

Where a is the cylinder radius and α_n is the nth root of a Bessel function of the 1st kind, of order zero, such that it satisfies $J_0(a\alpha_n) = 0$. We use our gravimetry data and fit equation above to estimate $D_0 = 5 \times 10^{-11}$ m^{2}s^{-1} which agrees reasonably well with the experimentally estimated nominal value of 2.0×10^{-11} m^{2}s^{-1} given that it assumes only radial diffusion in a cylinder.

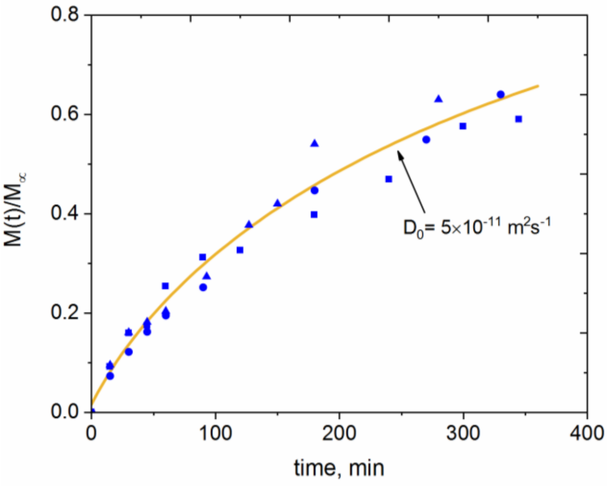

Figure D3. Equation 11 is fitted with $D_0 = 5 \times 10^{-11} m^2 s^{-1}$ (brown line) using data from three gravimetry experiments (blue markers).

D7. Effect of variation in shear modulus

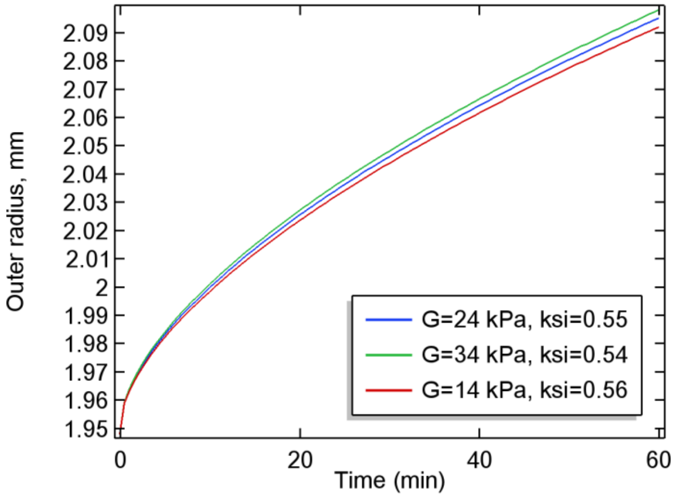

Figure D4. Variation in outer radius with shear modulus. The values of Flory's parameter are obtained by iteratively solving the equilibrium swelling equation.

D8. Swelling induced cracking of dry polymer core

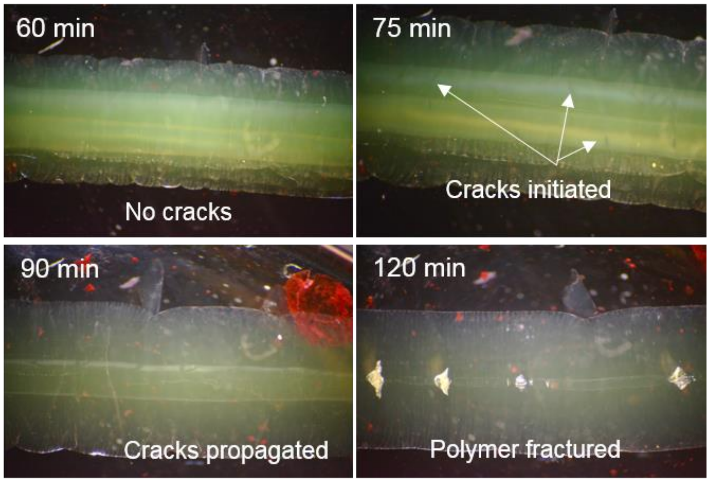

Figure D5. Images of NBPA-33 cylinder swelling in *o*-Xylene at different times showing swelling induced cracking and fracture of non-swollen dry polymer core.